UNIVERSITÉ DU LUXEMBOURG

TECHNISCHE UNIVERSITÄT DRESDEN

PhD-FSTC-2017-17

Faculty of Sciences, Technology and Communication

Fakultät Mathematik und Naturwissenschaften

Spin texture of two-dimensional topological insulators

Binational Dissertation

to obtain the degree of

Docteur de l'université du Luxembourg

en physique

and

Doctor rerum naturalium (Dr. rer. nat.)

by

Alexia Rod

Born on 2nd of August 1989 in Geneva (Switzerland)

Submitted on 08.02.2017 in Luxembourg and on 10.01.2017 in Dresden

Presented on 24.03.2017 in Dresden

This dissertation was produced from September 2013 to August 2015 at the Institute for Theoretical Physics, Technische Universität Dresden and from September 2015 to December 2016 at the Physics and Materials Science Research Unit, University of Luxembourg.

Dissertation defense committee – Doctorate Commission:

Prof. Dr. Thomas Schmidt, Dissertation supervisor, assessor
Associate professor, Université du Luxembourg

Prof. Dr. Matthias Vojta, Dissertation supervisor, assessor
Professor, Technische Universität Dresden

Prof. Dr. Hans-Henning Klauß, Chairman
Professor, Technische Universität Dresden

Prof. Dr. Thierry Giamarchi
Professor, Université de Genève

Prof. Dr. Patrik Recher
Professor, Technische Universität Braunschweig

Prof. Dr. Ludger Wirtz
Professor, Université du Luxembourg

"Beyond the edge of the world there's a space where emptiness and substance neatly overlap, where past and future form a continuous, endless loop. And, hovering about, there are signs no one has ever read, chords no one has ever heard."

Haruki Murakami

Abstract

Since the discovery of two-dimensional topological insulators a decade ago, their one-dimensional edge states have attracted significant attention due to their unique properties. For example due to time-reversal symmetry, they are protected against elastic backscattering and they propagate such that electrons with opposite spins move in opposite directions. In fact, the only necessary symmetry to sustain the edge states is time-reversal symmetry. Moreover in experimental setups, the axial spin symmetry seems to be absent. This absence allows new processes to appear such as inelastic backscattering. However, these consequences were neglected in most theoretical works where the spins are considered to be polarized in the z direction.

The aim of this thesis is to provide a more realistic model taking into account a broken axial spin symmetry. In this scheme, we show that a rotation of the spin quantization axis as a function of momentum always appears. This observation leads us to develop a deeper understanding of the size of the rotation related to the material parameters and material models, using also realistic values. It also leads us to understand the implications in real space in cases where translation invariance is lost and how to quantify the rotation in such systems.

The new processes which arise when the axial spin symmetry is broken have important consequences for transport in real materials. To see this, we consider a Hall bar with a hole in its middle, i.e. an antidot. This enables us to create two tunneling regions in order to probe the effect of this generic model. We also consider the effect of Coulomb interactions around the hole, as they can be important in such geometry. We discover that it is possible to probe directly the absence of axial spin symmetry. As experimental evidence is important to investigate our theoretical findings, we propose spectroscopic means to probe the spin texture.

Finally, we also consider one of the experimentally-known candidate materials, namely InAS/GaSb heterostructures. From the $k \cdot p$ Hamiltonian, it is possible to show that their bandstructure shows some anisotropies. The latter is also reflected in the spin texture of their edge states.

Contents

1 Introduction: Topological insulators

Low dimensional systems (i.e. systems in one or two dimensions) have attracted a lot of attention and research throughout the second half of the 20^{th} century. They continue to be an active and fascinating field of research. New processes occur in these systems where their quantum nature becomes more apparent, and exotic states and phases can emerge. One famous example is spin-charge separation in a one-dimensional system [1]: the electrons can form particular quasiparticles whose quantum numbers cannot be traced back to the original electrons and holes. One of the quasiparticles named the spinon has a spin-1/2, but no charge, whereas another of these quasiparticles is called the holon. It has no spin, but the charge of an electron. These two quasiparticles propagate at different velocities and behave independently from the other. They were experimentally measured in $SrCuO_2$ crystals [2, 3] and in quantum wires made by electron-beam lithography on the upper layer of a GaAs-AlGaAs double quantum well [4].

With the fast pace of new materials discoveries and new technical opportunities, we must be able to explore this area of condensed matter physics theoretically and experimentally. Examples of such low dimensional systems include nanowires, the ballistic edge states of a quantum Hall bar or Bose-Einstein condensates using cold atoms in one-dimensional optical lattice in one dimension. In two dimensions, we have the two dimensional electron gas, graphene or high-temperature cuprate superconductors. Theoretically, the progresses in the ab initio methods and the explosion of computing power enable us to probe numerically the stability and the physical properties of new compounds before they can be synthesized. On the experimental side, the development of nanotechnologies and more recently cold atoms created a new playground for condensed matter physicists to explore these previously unusual systems.

The discovery of graphene [5], a free standing two-dimensional material, opened new opportunities and brought new hopes for these exotic systems. Graphene hosts peculiar properties: its bandstructure has a gapless linear dispersion relation. In the absence of impurities, graphene is a semimetal, i.e. the overlap between the valence and the

conduction bands is pointlike. Moreover, the linearity of the dispersion means that the electrons can be described by spinless fermions with no mass term. They satisfy Dirac equation and they are therefore called Dirac fermions. In addition, graphene can be produced by exfoliation [5]. Graphene also features unique optical, thermal, electrical and mechanical properties. Early in its discovery, about a decade ago, graphene also inspired Kane and Mele to theoretically propose a new class of materials, which is called two-dimensional topological insulators [6–8]. The generalization to a three-dimensional version was made the year after [9–11].

Two-dimensional topological insulators differ from normal or also called "trivial insulators" as they are predicted to be bulk insulators with gapless states located at their edges. These edge channels are related to the topological nature of the band structure, and should always exist at the interface with a trivial insulator. A few years later, topological insulators made of HgTe [12] and InAs/GaSb heterostructures [13] revealed their unique properties in different experimental laboratories using transport setups. These discoveries created a new vivid field of research as topological insulators may be useful in other fields such as spintronics or quantum computing. This thesis hopes to contribute to the understanding of these peculiar materials.

One focus point of the field is the study of the edge channels. They are characterized by their helical nature [14]. This means that they always come in a counterpropagating pair with opposite spin orientation. This property comes from the protection afforded to the edge states by time-reversal symmetry, which is preserved in such system, as long as there is not any magnetic field or magnetic impurities. In most theoretical works, the spin orientation of the edge states is considered to be polarized in the z direction. However, the axial spin symmetry is not essential for the existence of this topological phase. Only time-reversal symmetry is crucial. Moreover in experimental devices, effects may arise such as Rashba spin-orbit coupling or bulk inversion asymmetry [7, 15, 16] which do not break time-reversal symmetry, but break the axial spin symmetry. The source of the spin quantization axis symmetry-breaking can originate directly from the bulk material as bulk inversion asymmetry, or in the case of Rasbha spin-orbit coupling, it can be induced by an electric field or the substrate on top of which the topological insulator is grown.

In the absence of spin axis symmetry, the edge states remain helical, i.e. the states counterpropagate. However, they do not now have a well-defined spin as they form a combination of spin-up and spin-down. In momentum space, it was realized that close to the Dirac point, i.e. the point where the edge states are crossing, the spin axis of the edge states is rotating [17]. The aim of this thesis is to better understand the consequences and the applications of a broken spin quantization axis. We will first try to quantify this rotation as a function of the materials' parameters and see how it is possible to enhance

this effect. We will also extend the understanding of this rotation in real space and how it could appear in experimental setups. Another aim of this thesis is to explain how to detect the breaking of the spin axis symmetry through physical measurements and quantities. It was pointed out that the broken spin axis symmetry should give some correction to the conductance at finite temperature [17], but we will use transport and spectroscopic setups to propose other means to detect it.

In this introductory chapter, we will start with the trending topic of topology in condensed matter physics, a subject which resulted in the 2016 Nobel Prize in physics being given to Thouless, Haldane and Kosterlitz. We will then focus our discussion on the particular topic of two-dimensional insulators. We will then investigate the mechanisms triggering such a phase as well as the subsequent models and possible materials. We will conclude this chapter in introducing the concept of generic helical edge states, a central notion to understanding the spin texture in two-dimensional topological insulators. It can be noted that several reviews [18–23] and books [24–26] on this introductory theme and beyond have already been written.

1.1 Topology in condensed matter physics

The study of phases of matter and the properties that characterize them are an important topic in condensed matter physics. Usually, the classification is done through Landau theory [27], involving the symmetries that are spontaneously broken in each phase. These symmetries can be either discrete or continuous. One typical example is liquid water becoming ice. From one phase to the other, the translational and rotational symmetries become spontaneously broken, as the ice forms a crystalline order. Nonetheless, this description of phases of matter does not give a complete classification.

One of the first hints appeared in 1980 when von Klitzing et al. performed the first measurement of the Integer Quantum Hall Effect (IQHE) in a two-dimensional electron gas (2DEG) at low temperature and high magnetic field [28]. It was discovered that the current is carried by the edge whereas the bulk remains insulating, resulting in a longitudinal resistance of 0. The edge current leads to a quantized Hall conductance at some particular values

$$\sigma_H = n\frac{e^2}{h}, \tag{1.1}$$

where n is an integer, e the elementary charge and h the Planck constant. The first experimental evidence of IQHE is shown in Fig. 1.1 [28]. We indeed observe drops in the longitudinal voltage each time the Hall voltage reaches a plateau value. The measured Hall voltages at the plateaus are determined by the value of the applied current multiplied by the values of the Hall resistance. The latter is precisely quantized independently of the

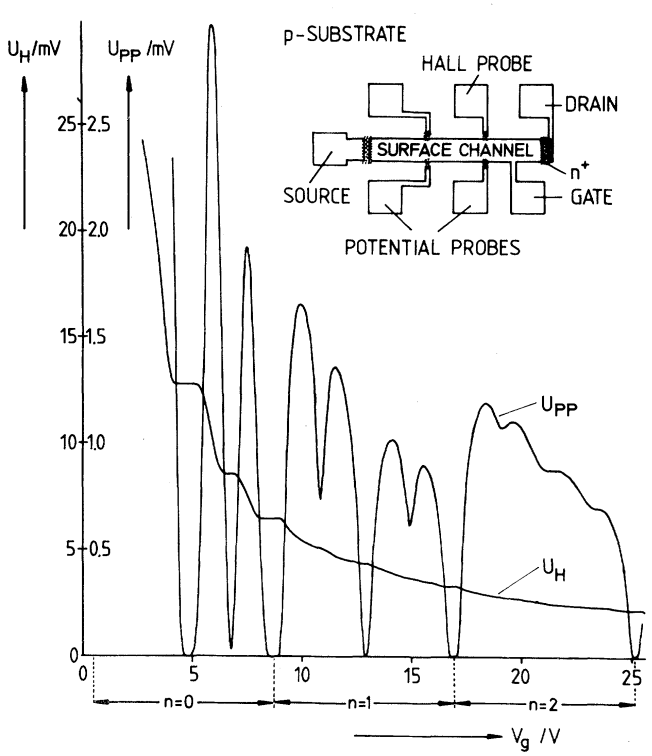

Figure 1.1: Hall voltage U_H and longitudinal voltage U_{PP} measured as a function of the gate voltage V_g at a temperature of 1.5K and a magnetic field of 18T, figure taken from Ref. [28].

geometric details of the measured sample or of the disorder on the mesa. This originates from the topological nature of the conductance. In a semiclassical interpretation [29], the electrons are localized on cyclotron orbits due to the high magnetic field. These orbits are quantized, forming Landau levels. On the edge, the electrons cannot complete the full orbit, but instead move along the edge in a skipping motion. The topological origin of the Hall conductance quantization cannot be understood through the conventional Landau theory in terms of an order parameter, but rather through a topological invariant, the first Chern number, which can only be an integer independently of the details of the setup [30, 31]. The system exists in a different phase at each different value of n, without breaking any symmetry. Therefore, the system should go through a quantum phase transition, each time the value of n is changed by an integer number.

Before continuing further in the direction of IQHE, we can focus on the consequences of the appearance of this topological invariant. First, we should define what topology in the context of condensed matter physics means. In mathematics, topology can be introduced to classify a space by the properties that are preserved under a "smooth transformation". Smooth in this context that the transformation can be carried out continuously. Therefore, the global properties of a space are those of interest, not the particular geometric details.

As an example of the use of topology in mathematics, we can roughly say that we can classify a space by the number of "holes" it has – the genus. A torus has a different genus compared to a sphere. In a physical context, the meaning of topology is related by analogy to this "smooth transformation". We consider only Hamiltonians with a bulk gap. Two Hamiltonians are considered as topologically equivalent, if we can change smoothly one Hamiltonian into the other without closing this bulk band gap. A phase transition between two distinct topological phases is only possible when the gap closes.

To characterize the different physical phases, we need a topological invariant, the Chern invariant. Berry introduced in Ref. [32] the concept of a geometrical phase which appears during the time-evolution of the wave function during adiabatic transport in slowly varying fields. This "Berry" phase is distinct from the usual dynamical phase e^{iEt}. On a closed loop, the Berry phase cannot be removed unless it happens to take an integer value multiplied by 2π. On a closed loop in the Brillouin zone, the Berry phase appears as the k momentum is adiabatically varied [33]. Simon [34] pointed out the equivalence between the invariant proposed by Thouless et al. in Ref. [31], namely the Chern number and the Berry phase divided by 2π, when the surface bounded by the closed loop corresponds to the full Brillouin zone. The link with the mathematics of fiber bundles was also clearly stated [35, 36].

At the interface between two systems in different topological phases, the gap has to close in order to move from one topological phase to the other. This change of phase is also characterized by a change in the topological invariant. Moreover, the gap closing is mediated by gapless chiral edge modes. Here the meaning of chiral is that they propagate only in one direction. They are bound to the edge of the two systems, where the gap closes. In fact, these edge modes are a manifestation of the bulk topological invariant. The first link between topology and edge modes was proposed in 1976 in Ref. [37] and is called the bulk-boundary correspondence [18, 26].

Finally, if we return to the IQHE, we can present a model, which was introduced by Haldane in Ref. [38]. This model inspired the theoretical discovery of topological insulators, as we will see later. Haldane realized that the key ingredient in the observation of the IQHE is not the external magnetic field but the breaking of time-reversal (TR) symmetry. We will come back to the importance of this symmetry in the next section. The Haldane model consists of spinless fermions on a honeycomb lattice. It is composed of a hexagonal lattice, where the unit cells contain two sites and hence the lattice is formed of two sublattices. The magnetic field is chosen such that in one hexagonal plaquette, the total magnetic flux cancels. The tight-binding Hamiltonian can be written as [24]

$$H = t_1 \sum_{\langle ij \rangle} c_i^\dagger c_j + t_2 \sum_{\langle\langle ij \rangle\rangle} e^{-i\nu_{ij}\phi} c_i^\dagger c_j + M \sum_i \varepsilon_i c_i^\dagger c_i, \tag{1.2}$$

where t_1 is the nearest-neighbor hopping. The second term describes the next-nearest-neighbor hopping t_2 which acquires an additional phase $e^{-i\nu_{ij}\phi}$. This phase originates from the flux acquired during the hopping and $\nu_{ij} = \pm 1$ will change depending on the hopping rotation direction. We will discuss about this phase in more detail in Sec. 1.4.1. Finally, the last term is the inversion-breaking mass term [39], where $\varepsilon_i = \pm 1$ if the particle is on the sublattice A or on the sublattice B. The interplay between the inversion breaking mass term and the broken TR-symmetry due to the flux enables us to compute a nonzero Hall conductance.

1.2 Topological insulators

Haldane described a nontrivial topological state where TR-symmetry is absent. The key idea was to have an internal magnetic field which resulted in a vanishing total magnetic flux. Although it remained relatively forgotten for more than 15 years, it paved the way to the discovery of topological insulators (TIs) [6], where TR-symmetry is this time preserved. To preserve TR-symmetry, the idea is to have a magnetic field which points in opposite directions for each spin orientation. This can be achieved in the presence of spin-orbit coupling (SOC) which acts as an effective magnetic field and depending on the spin orientation, but at the same time preserves TR-symmetry. We will come back to SOC and its origin in the next section. Finally, note the deep link of TI with IQHE: they are both members of the Hall effect family; indeed two-dimensional TIs are also called Quantum Spin Hall Effect (QSHE). Moreover, QSHE can be seen as copies of IQHE states, one for each spin direction, which feel opposite effective magnetic fields. We will only discuss two-dimensional TIs throughout this thesis.

The presence of TR-symmetry has a crucial impact and important consequences on fermionic particles, i.e. in particular on electrons. The effect of TR is to reverse the arrow of time, namely $t \to -t$. Its operator Θ acts on space and momentum operators as $\Theta x \Theta^{-1} = x$ and $\Theta p \Theta^{-1} = -p$ respectively. This means that Θ can be generally written as the combination of a unitary operator U and complex conjugation K: $\Theta = UK$. It leads to the fact that $\Theta^2 = \pm\mathbb{1}$. For spin operators, TR-symmetry acts as $\Theta \vec{S} \Theta^{-1} = -\vec{S}$. By historical convention, the TR-operator rotates the spin by π around the y axis, leading to the following expression

$$\Theta = e^{i\pi S_y} K, \tag{1.3}$$

such that $\Theta^2 = \pm\mathbb{1}$ for bosonic and fermionic particles respectively. Furthermore, Kramers theorem [40] states that fermionic particles are at least doubly degenerate under TR-symmetry. For example if we take one eigenfunction $|\psi\rangle$ of $\mathcal{H}$ and $[\mathcal{H}, \Theta] = 0$, then $\Theta|\psi\rangle$ is also an eigenfunction of $\mathcal{H}$. Moreover, it has the same eigenenergy and it is orthogonal

to $|\psi\rangle$. One important consequence of Kramers theorem is that in a translation symmetric space (e.g. in a crystal) it implies that the eigenstates of the Hamiltonian with momenta $\mathbf{k}$ and $-\mathbf{k}$ have the same energy. Only at some special points of the Brillouin zone, named Time-Reveral Invariant Momenta (TRIM), we have a pair of degenerate states. As an example, in a two-dimensional Brillouin zone for a square lattice, the TRIM are located at $(0,0)$, $(0,\pm\pi/a)$, $(\pm\pi/a,0)$ and $(\pm\pi/a,\pm\pi/a)$, where a is the lattice constant.

That the TI preserves TR-symmetry leads to a Chern number of $n=0$. Nonetheless, it is still in another topological class to the trivial insulator, a class which is characterized by a $\mathbb{Z}_2$ invariant, i.e. either $\nu=0$ or $\nu=1$ [6]. We can understand this result using bulk-boundary correspondence. Note that now, due to Kramers theorem, the edge states necessarily come in pairs, as they are Kramers partners. Moreover, these pairs are defined as helical [14], as they must propagate in opposite directions with opposite spin axis. If we have an odd number of pairs of edge states in the gap, it is not possible to eliminate all of the edge states by gapping them out without violating TR-symmetry. However, if we have an even number of pairs of edge states, we can eliminate them completely without violating TR-symmetry, by gapping them out. We can then relate the difference between two values of the $\mathbb{Z}_2$ invariant to the number of edge states appearing at the interface through the following equation

$$\Delta\nu = N_K \mod 2, \tag{1.4}$$

where N_K is the number of Kramers pairs [18, 26]. As the Hamiltonian has to remain TR-invariant, some terms such as elastic backscattering or magnetic impurities are forbidden. This then leads to a protection of the edge states against such mechanisms, making them robust against small perturbations.

1.3 Spin-orbit coupling

We saw that SOC plays an important role in the physics of TIs. It enables us to have an effective momentum-dependent magnetic field, which does not break TR-symmetry. Nonetheless, the presence of SOC in a material does not necessarily lead to a TI phase and in most cases, no such phase will occur. SOC arises from the relativistic effects. We can first distinguish two origins: one originating directly from the atoms and their intrinsic structure and the other from the crystal structure. If we start with the atomic part of SOC, we can consider the relativistic hydrogen-like model. Even though this model is quite simplified, it gives already the first insights for the atomic origin of SOC.

The nonrelativistic hydrogen model [41–43] has Hamiltonian

$$H = \frac{p^2}{2m_e} - \frac{Ze^2}{r}, \tag{1.5}$$

where the first term is the nonrelativistic kinetic energy of the electron and the second term is the Coulomb potential of the atomic nucleus felt by the electron. Z is the atomic number. As the electron moves in the nuclear electric field, the electron experiences an effective magnetic field. A coupling between the electron spin $\mathbf{S}$ and the orbital momentum $\mathbf{L} = \mathbf{r} \times \mathbf{p}$ appears [41–43], such that there is an additional term

$$H_{\mathrm{SO}} = \frac{1}{2m_e^2c^2}\frac{1}{r}\frac{\mathrm{d}V}{\mathrm{d}r}\mathbf{L}\cdot\mathbf{S} = \frac{1}{2m_e^2c^2}\frac{Ze^2}{r^3}\mathbf{L}\cdot\mathbf{S}. \tag{1.6}$$

There is then a coupling between the orbital angular momentum and the spin orientation of the electron. We observe that the atomic number Z enters in the evaluation of the SOC energy contribution. If we compute the energy difference induced by SOC, we get a Z^4/n^3 dependence, where n is the principal quantum number, indicating the electron's shell. Therefore, heavier atoms will present stronger SOC effects. In atoms, one consequence of SOC is the appearance of the fine structure.

A very important consequence of atomic SOC for TIs appears in the inversion of the bandstructure. The order of the valence and the conduction bands can get inverted leading to a negative mass gap. To adiabatically connect a Hamiltonian with an inverted mass gap to a normal insulator which has a positive mass gap, it is necessary to close the gap. Therefore in case of a strong SOC which enables a band inversion, a TI phase can emerge [8, 44].

If we consider crystalline structures, additional SOC arises if there is a lack of inversion symmetry [43, 45]. This lack of inversion symmetry appears

- at the interface of the crystal, or
- if the crystal lattice does not have a center of inversion, or
- if there is locally a lack of inversion symmetry.

In the two first cases, the additional SOC is not responsible for creating a TI phase, but are important sources for breaking the axial spin symmetry. The lack of inversion symmetry at the interface is called Structural Inversion Asymmetry (SIA), which can in some systems lead to (Bychkov-)Rashba SOC [46, 47]. If the crystal is grown in the z-direction, there is an effective electric field $\mathbf{E}$ pointing in the z-direction at the interface such that $\mathbf{E} = E_z\mathbf{z}$. The electron moving at the surface will "feel" an effective magnetic

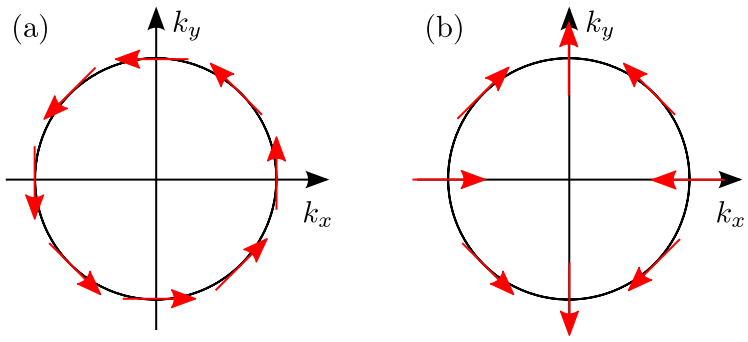

Figure 1.2: Sketch of the Fermi surface and of the spin orientation in case of the absence of inversion symmetry. Panel (a) shows the spin orientation in the presence of Rashba SOC and panel (b) shows the spin orientation in the presence of linear Dresselhaus SOC.

field due to this electric field. The Rashba SOC term can then be expressed as

$$H_{\mathrm{R}} = \alpha_R(\mathbf{z} \times \mathbf{p}) \cdot \boldsymbol{\sigma}, \tag{1.7}$$

where α_R is the Rashba SOC constant. This constant is material dependent. Rashba SOC locks the electron's spin to lie in the plane perpendicular to z and it imposes that the spin axis is also perpendicular to the momentum. This is called spin-momentum locking and its effect at the Fermi surface is shown in Fig. 1.2(a).

The lack of a center of inversion, typically in III-V semiconductors like GaAs or InSb, is called Bulk Inversion Asymmetry (BIA), which can lead to Dresselhaus SOC [48]. It was first noticed by Dresselhaus that close to the Γ point, SOC can be expressed as

$$H_{\mathrm{D}}^{\mathrm{3D}} = \gamma_D \left[(p_y^2 - p_z^2)p_x\sigma_x + (p_z^2 - p_x^2)p_y\sigma_y + (p_x^2 - p_y^2)p_z\sigma_z\right], \tag{1.8}$$

where γ_D is the Dresselhaus SOC constant. For a crystal grown in the z-direction, which exhibit a 2DEG, it is possible to simplify the expression above [49]. We can estimate the expectation values $\langle k_z \rangle = 0$ and $\beta_D = \gamma_D \langle k_z^2 \rangle$. Moreover, we can only keep the linear term in k_x and k_y. The Hamiltionian now becomes

$$H_{\mathrm{D}} = \beta_D \left[p_y\sigma_y - p_x\sigma_x\right]. \tag{1.9}$$

The linear term also locks the spin in the surface plane perpendicular to z. However this time, it imposes that the spin axis is parallel to the momentum. Its effect at the Fermi surface is shown in Fig. 1.2(b). Note that at the interface of semiconductors without a center of inversion, we will see the appearance of both SIA and BIA, and both effects will combine resulting in a particular spin orientation at the Fermi surface. Moreover, they will break the spin quantization axis symmetry. This will have important consequence for

the appearance of a nontrivial spin texture.

Finally, we can also consider when inversion symmetry is locally absent in the crystal. In this case, SOC can also arise and we will define it as "intrinsic SOC". This type of SOC is very important in relation to TI phases, as it can open a nontrivial gap at the Fermi energy [7]. This gap will differ from the inversion-breaking mass term defined for example in Haldane Hamiltonian in Eq. (1.2) or in Ref. [39], as the system becomes gapless at some point to smoothly connect the states in these two types of gaps [7]. We will see an example in Sec. 1.4.1.

1.4 Proposed models and materials

In the previous section, we introduced the concept of topology in condensed matter physics, which led to the discovery of TIs. We pointed out the main features of TIs and we stressed the importance of SOC in such systems. We have now enough knowledge to move on to a more practical and realistic examination, where we explore the different proposed models as well as the material candidates.

1.4.1 Kane-Mele model for graphene

Chronologically, the first model for TIs was designed for graphene. Kane and Mele [6, 7] generalized the model developed by Haldane [38], where the phase-dependent hopping now originates from an intrinsic SOC. It leads to an opening of the gap at the K and K' points which, is of opposite sign at these two points. As noted in the previous section, this gap cannot be adiabatically traced to a simple inversion-breaking mass [7]. The phase-dependent hopping comes from the fact that the electron hopping to the next-nearest neighbor site feels the electric field emitted from the intermediate site. The electric field induces an effective magnetic field on the moving electron. This effective magnetic field generates a phase for the electron, which depends on the spin of the electron and on the position of the intermediate site, as shown in Fig. 1.3. The Hamiltonian is fully TR invariant. Moreover, if there is a perpendicular electric field or a substrate, Rashba SOC appears due to the breaking of inversion symmetry. As explained before, this term does not break TR symmetry either, but it does break spin axis symmetry. Nevertheless, the $\mathbb{Z}_2$ invariant is stable as long as the Rashba term is not sufficiently large to close the gap [7, 50]. The Kane-Mele (KM) model can be written in a tight-binding form as

$$H_{\mathrm{KM}} = -t \sum_{\langle ij \rangle} c_i^\dagger c_j + i\lambda_{\mathrm{SO}} \sum_{\langle\langle ij \rangle\rangle} \nu_{ij} c_i^\dagger s^z c_j + i\lambda_{\mathrm{R},1} \sum_{\langle ij \rangle} c_i^\dagger (\mathbf{s} \times \hat{\mathbf{d}}_{ij})_z c_j, \tag{1.10}$$

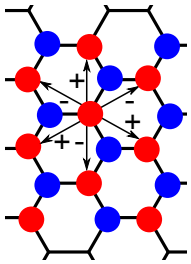

Figure 1.3: Sign of the phases resulting from the intrinsic SOC.

where $c_j = (c_{j\uparrow}, c_{j\downarrow})^T$ is a spinor. t is the nearest-neighbor hopping, λ_{SO} is the intrinsic SOC and $\lambda_{\mathrm{R},1}$ is the Rashba SOC. $\nu_{ij} = \pm 1$ is the phase described above, resulting from the induced effective magnetic field when the electron hops to its next-nearest-neighbor. This is the same phase presented in the Haldane model in Eq. (1.2). It will take the value ± 1 if the electron makes a "left turn" (resp. "right turn"), as indicated in Fig. 1.3. $\mathbf{s}$ is the physical spin and $\hat{\mathbf{d}}_{ij}$ is the unit vector between the site j and the site i. We define the translation vectors between neighboring sites as

$$\boldsymbol{\delta}_1 = \frac{a}{\sqrt{3}} \begin{pmatrix} -1 \\ 0 \end{pmatrix}, \quad \boldsymbol{\delta}_2 = \frac{a}{2\sqrt{3}} \begin{pmatrix} 1 \\ \sqrt{3} \end{pmatrix}, \quad \boldsymbol{\delta}_3 = \frac{a}{2\sqrt{3}} \begin{pmatrix} 1 \\ -\sqrt{3} \end{pmatrix}, \tag{1.11}$$

where a is the lattice constant. The unit cell is formed by two equivalent atoms (a & b) represented in red and in blue respectively in Fig 1.3. We can describe the spinor c_j in terms of elements of the sublattice a_j and b_j. We must consistently take into account the hopping to the nearest and to the next-nearest neighbors. The lattice unit vectors are $\mathbf{a}_1 = \delta_2 - \delta_1$ and $\mathbf{a}_2 = \delta_3 - \delta_1$.

We Fourier transform the Hamiltonian into momentum space, such that the operators become

$$c^\dagger_{\mathbf{k}} = \sum_j e^{i\mathbf{k}aj} c^\dagger_j, \qquad c_{\mathbf{k}} = \sum_j e^{-i\mathbf{k}aj} c_j. \tag{1.12}$$

The Hamiltonian can be rewritten as

$$H_{\mathrm{KM}} = \sum_{\mathbf{k}} \Psi^\dagger(\mathbf{k}) \mathcal{H}_{\mathrm{KM}}(\mathbf{k}) \Psi(\mathbf{k}), \tag{1.13}$$

where $\Psi(\mathbf{k}) = (a_\uparrow(\mathbf{k}), b_\uparrow(\mathbf{k}), a_\downarrow(\mathbf{k}), b_\downarrow(\mathbf{k}))^T$. The Hamiltonian is now expressed in terms of the Bloch matrix

$$\mathcal{H}_{\mathrm{KM}}(\mathbf{k}) = \begin{pmatrix} \varepsilon(\mathbf{k}) & -\tau(\mathbf{k}) & 0 & \rho_1(\mathbf{k}) \\ -\tau^*(\mathbf{k}) & -\varepsilon(\mathbf{k}) & \rho_2(\mathbf{k}) & 0 \\ 0 & \rho_2^*(\mathbf{k}) & -\varepsilon(\mathbf{k}) & -\tau(\mathbf{k}) \\ \rho_1^*(\mathbf{k}) & 0 & -\tau^*(\mathbf{k}) & \varepsilon(\mathbf{k}) \end{pmatrix}, \tag{1.14}$$

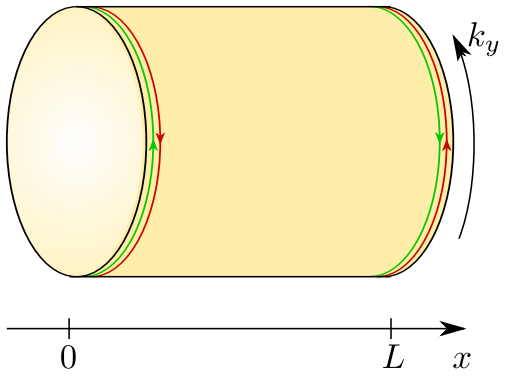

Figure 1.4: Sketch of a TI nanorribon of length L. The inside is hollow. At each end, there are two edge states propagating in opposite directions and are characterized by their momenta.

where the different terms appearing in the Hamiltonian are **k**-dependent

$$\tau(\mathbf{k}) = t\left[1 + e^{\sqrt{3}iak_x/2}e^{iak_y/2} + e^{iak_y}\right], \tag{1.15}$$

$$\varepsilon(\mathbf{k}) = 2\lambda_{\mathrm{SO}}\left[\sin(ak_y) - 2\sin(ak_y/2)\cos(\sqrt{3}ak_x/2)\right], \tag{1.16}$$

$$\rho_1(\mathbf{k}) = \frac{i\lambda_{\mathrm{R},1}}{2}\left[(-\sqrt{3}-i) + e^{iak_y}(\sqrt{3}-i) + 2ie^{\sqrt{3}iak_x/2}e^{iak_y/2}\right], \tag{1.17}$$

$$\rho_2(\mathbf{k}) = \frac{i\lambda_{\mathrm{R},1}}{2}\left[(\sqrt{3}+i) + e^{-iak_y}(-\sqrt{3}+i) - 2ie^{-\sqrt{3}iak_x/2}e^{-iak_y/2}\right]. \tag{1.18}$$

We would like to model a TI nanoribbon, i.e. a hollow cylinder. As the nanoribbon is surrounded by vacuum, edge states will appear localized at both ends of the nanoribbon, as shown in Fig. 1.4. We can understand this using bulk-boundary correspondence in Eq. (1.4), as vacuum is a trivial insulator. We partially Fourier transform Eq. (1.10) in the y-direction using

$$c^\dagger_{l,k_y} = \sum_j e^{ik_yaj}c^\dagger_{l,j}\,, \qquad c_{l,k_y} = \sum_j e^{-ik_yaj}c_{l,j}. \tag{1.19}$$

It is possible to plot the band energy spectrum as a function of momentum, because there is still one periodic direction. Note that the there are two pairs of edge states due to the finite length of the ribbon, i.e. there are two states at $x = 0$ and two states at $x = L$. An example of such nanoribbon using KM model is shown on Fig. 1.5. We set $a = 1$, $t = 1$, $\lambda_{\mathrm{SO}} = 0.2$ and $\lambda_{\mathrm{R},1} = 0.05$. The gap Δ is determined by the strength of the intrinsic SOC, $\Delta/2 = 3\sqrt{3}\lambda_{\mathrm{SO}}$. Note that the edge states start at the K and K' points where the Dirac cones open and cross at the TRIM $k_y = \pi$. Rashba SOC breaks particle-hole symmetry ($E(k) \to -E(k)$).

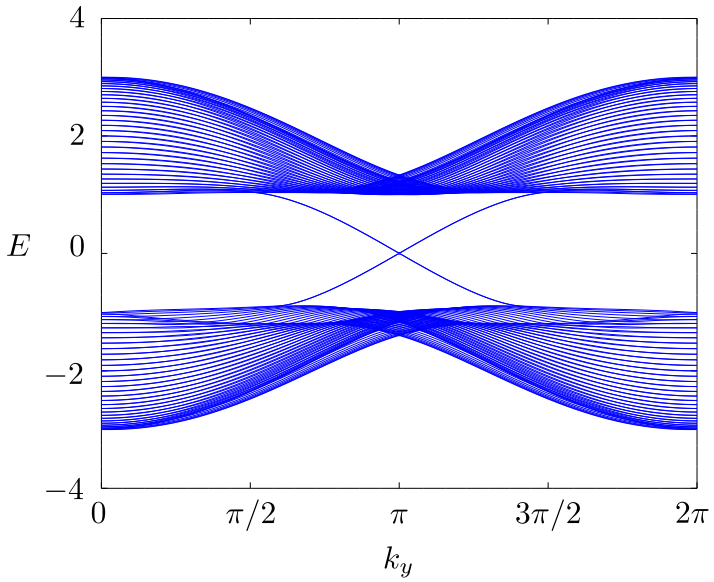

Figure 1.5: The energy spectrum of the KM Hamiltonian for a nanoribbon of L=32 unit cells. We set $a = 1$, $t = 1$, $\lambda_{\mathrm{SO}} = 0.2$ and $\lambda_{\mathrm{R},1} = 0.05$.

1.4.1.1 Silicene, Germanene & Stanene

It was soon noted that SOC in graphene is too small to generate a measurable gap [51, 52]. In order to increase SOC, we can use heavier elements than carbon as we saw in Sec. 1.3. We replace the carbon atoms by silicon, germanium or tin atoms to form silicene, germanene or stanene respectively. From first principles calculations [53, 54], the gap is large enough to hope for room-temperature experiments due to the enhanced SOC. Due to buckling of the structure, an additional intrinsic Rashba SOC term appears in these non-graphene systems [54]. It is expressed as

$$H_{\mathrm{R},2} = -i\frac{2}{3}\lambda_{\mathrm{R},2}\sum_{\langle\langle ij\rangle\rangle}\mu_{ij}\, c_i^{\dagger}(\mathbf{s}\times\hat{\mathbf{d}}_{ij})_z\, c_j, \tag{1.20}$$

where $\mu_{ij} = \pm 1$ is a phase for the sublattice a and b respectively and $\hat{\mathbf{d}}_{ij}$ is the unit vector between the site i and the site j. It is still possible to apply an electric field or use the substrate to induce a tunable Rashba interaction like in Eq. (1.10) [55]. We can also Fourier transform this Hamiltonian, to have the Bloch matrix

$$\mathcal{H}_{\mathrm{R},2}(\mathbf{k}) = \begin{pmatrix} 0 & 0 & -\rho_3(\mathbf{k}) & 0 \\ 0 & 0 & 0 & \rho_3(\mathbf{k}) \\ -\rho_3^*(\mathbf{k}) & 0 & 0 & 0 \\ 0 & \rho_3^*(\mathbf{k}) & 0 & 0 \end{pmatrix}, \tag{1.21}$$

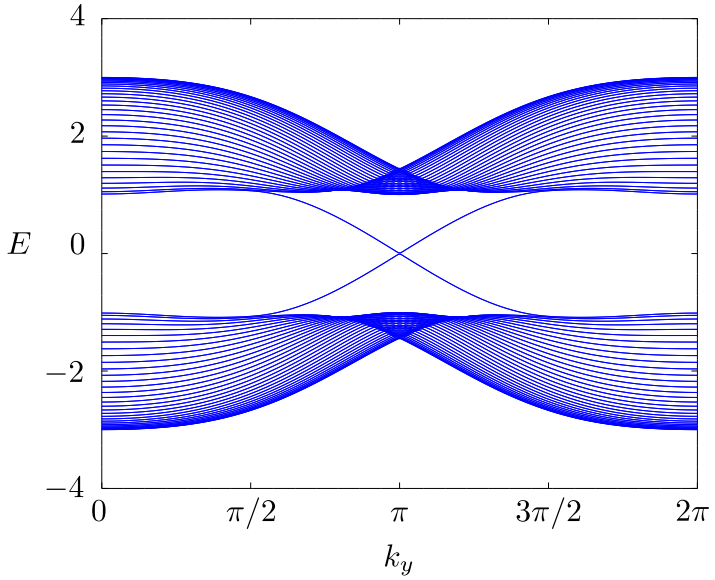

Figure 1.6: The energy spectrum of silicene described by the KM Hamiltonian and $\lambda_{\mathrm{R},2}$-term, for a nanoribbon of L=32 unit cells. We set $a = 1$, $t = 1$, $\lambda_{\mathrm{SO}} = 0.2$, $\lambda_{\mathrm{R},1} = 0$ and $\lambda_{\mathrm{R},2} = 0.5$.

where $\rho_3(\mathbf{k})$ is given by

$$\rho_3(\mathbf{k}) = \frac{4}{3}\lambda_{\mathrm{R},2}\Big[\sin(ak_y) + \cos(\sqrt{3}ak_x/2)\sin(ak_y/2) + \sqrt{3}i\sin(\sqrt{3}ak_x/2)\cos(ak_y/2)\Big]. \tag{1.22}$$

As for the KM model, we can partially Fourier transform the Hamiltonian and produce a plot for the energy spectrum of a nanoribbon as shown in Fig. 1.6. We set $a = 1$ and $t = 1$ such that $\lambda_{\mathrm{SO}} = 0.2$, $\lambda_{\mathrm{R},1} = 0$ and $\lambda_{\mathrm{R},2} = 0.5$. There are a few differences compared to the case of extrinsic Rashba SOC: the intrinsic Rashba SOC preserves the particle-hole symmetry but its effect is weaker (between Fig. 1.5 and Fig 1.6, there is a factor 10 between the two Rashba SOC strengths).

1.4.2 Bernevig-Hughes-Zhang model for HgTe heterostructures

Soon after KM, Bernevig, Hughes & Zhang [8] (BHZ) developed another model for two-dimensional TI. They used the zinc blende structure of a heterostructure formed by a layer of HgTe sandwiched between two layers of CdTe. Zinc blende lattices are two interpenetrating face-centered cubic lattices, and they are a common crystal structure for binary compound semiconductors. Due to the strong SOC, the s-band and the p-bands get inverted near the Γ-point in the HgTe layer. This is not the case for the CdTe layer, as the SOC effect is weaker. We see the band structure of the two layers near the Γ-point

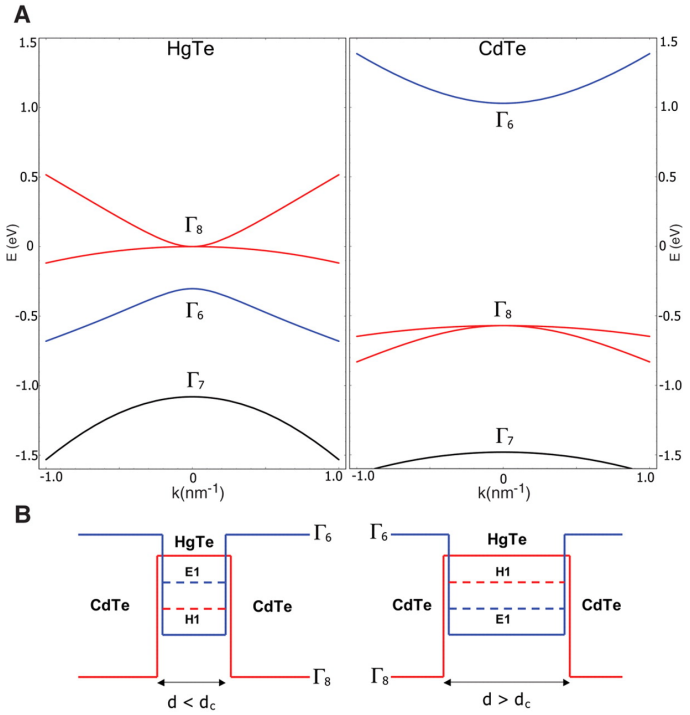

Figure 1.7: In panel (A), the bandstructure is plotted in each layer near the Γ-point. On the left, we have the bandstructure for HgTe, which has an inversion of the Γ_6 and Γ_8 bands. On the right, we have the bandstructure for CdTe. Panel (B) shows the band inversion in the effective model. If the length is shorter the critical value (left), the insulator remains trivial. Otherwise (right), it becomes a TI. Taken from Ref. [8].

in panel A of Fig. 1.7 [8], where Γ_7 and Γ_8 are p-bands and Γ_6 is an s-band.

It is possible to describe this system as an effective 2D system from $k \cdot p$ theory [49, 56] with only two spin-degenerate bands: one electron band $\{|E_1,+\rangle, |E_1,-\rangle\}$ and one hole band $\{|H_1,+\rangle, |H_1,-\rangle\}$. The states are confined to the HgTe layer. The inversion of these two effective bands, and thus also the topological phase transition occurs at a critical length $d_c = 6.3$nm. Below that critical value, the system is a trivial insulator and above it, it becomes a TI as shown in panel B of Fig. 1.7 [8]. More about zinc blende heterostructures and $k \cdot p$ theory will be presented in Chap. 4.

The effective two-dimensional Hamiltonian is expressed in the following manner

$$H_{\mathrm{BHZ}} = \sum_{\mathbf{k}} \Phi^{\dagger}(\mathbf{k}) \mathcal{H}_{\mathrm{BHZ}}(\mathbf{k}) \Phi(\mathbf{k}) = \sum_{\mathbf{k}} \Phi^{\dagger}(\mathbf{k}) \begin{pmatrix} h(\mathbf{k}) & 0 \\ 0 & h^{*}(-\mathbf{k}) \end{pmatrix} \Phi(\mathbf{k}), \tag{1.23}$$

where $\Phi(\mathbf{k}) = (E_+(\mathbf{k}), H_+(\mathbf{k}), E_-(\mathbf{k}), H_-(\mathbf{k}))^T$. $h(\mathbf{k})$ is a massive Dirac Hamiltonian

$$h(\mathbf{k}) = \varepsilon(\mathbf{k}) + \mathbf{d}(\mathbf{k}) \cdot \sigma, \tag{1.24}$$

where $\varepsilon(\mathbf{k}) = C - D(k_x^2 + k_y^2)$, $\mathbf{d}(\mathbf{k}) = (Ak_x, -Ak_y, M - B(k_x^2 + k_y^2))^T$ and $\sigma = (\sigma^x, \sigma^y, \sigma^z)^T$

are the Pauli matrices acting on the pseudospin of the subbands. A, B, C, and D are parameters that depend on the original layers. M is the band gap at the Γ-point, so that when M is negative there is a band inversion. The system is in a TI regime if $0 < M/(2B) < 2$. With this notation we can rewrite the Bloch matrices as

$$\mathcal{H}_{\mathrm{BHZ}}(\mathbf{k}) = \varepsilon(\mathbf{k})\mathbb{1}_{4x4} + d_1(\mathbf{k}) \cdot \sigma_x \otimes s_z + d_2(\mathbf{k}) \cdot \sigma_y \otimes \mathbb{1}_{2x2} + d_3(\mathbf{k}) \cdot \sigma_z \otimes \mathbb{1}_{2x2}, \tag{1.25}$$

where $\mathbf{s}$ is the physical spin. This continuous model can be regularized on a square lattice, such that $k_i \approx \sin(k_i)$ and $k_i^2 \approx 2-2\cos(k_i)$. It is interesting to note that the Hamiltonian is still block diagonal. Nonetheless, as the lattice is now formed of two types of atoms, inversion symmetry in the bulk is not preserved [57]. This leads to an additional term

$$\mathcal{H}_{\mathrm{BIA}}(\mathbf{k}) = \begin{pmatrix} 0 & 0 & 0 & -\Delta \\ 0 & 0 & \Delta & 0 \\ 0 & \Delta & 0 & 0 \\ -\Delta & 0 & 0 & 0 \end{pmatrix}, \tag{1.26}$$

where Δ is a material parameter. We now observe a term coupling the spin components. Structural asymmetry can be induced by an electric field, leading to k-dependent correction terms [16]. We Fourier transform the Hamiltonian back to real space,

$$\begin{aligned} H_{\mathrm{BHZ}} =& (C - \frac{4D}{a^2}) \sum_{ij\sigma} \left(e^\dagger_{ij\sigma} e_{ij\sigma} + h^\dagger_{ij\sigma} h_{ij\sigma} \right) + (M - \frac{4B}{a^2}) \sum_{ij\sigma} \left(e^\dagger_{ij\sigma} e_{ij\sigma} - h^\dagger_{ij\sigma} h_{ij\sigma} \right) \\ &+ \Bigg[\frac{D}{a^2} \sum_{ij\sigma} \left(e^\dagger_{i+1,j\sigma} e_{ij\sigma} + e^\dagger_{i,j+1\sigma} e_{ij\sigma} + h^\dagger_{i+1,j\sigma} h_{ij\sigma} + h^\dagger_{i,j+1\sigma} h_{ij\sigma} \right) \\ &+ \frac{B}{a^2} \sum_{ij\sigma} \left(e^\dagger_{i+1,j\sigma} e_{ij\sigma} + e^\dagger_{i,j+1\sigma} e_{ij\sigma} - h^\dagger_{i+1,j\sigma} h_{ij\sigma} - h^\dagger_{i,j+1\sigma} h_{ij\sigma} \right) \\ &+ \frac{A}{2a} \sum_{ij} \left(-ie^\dagger_{i+1,j\uparrow} h_{ij\uparrow} + ie^\dagger_{i-1,j\uparrow} h_{ij\uparrow} + ie^\dagger_{i+1,j\downarrow} h_{ij\downarrow} - ie^\dagger_{i-1,j\downarrow} h_{ij\downarrow} \right) \\ &+ \frac{A}{2a} \sum_{ij\sigma} \left(e^\dagger_{i,j+1\sigma} h_{ij\sigma} - e^\dagger_{i,j-1\sigma} h_{ij\sigma} \right) + \Delta \sum_{ij} \left(e^\dagger_{ij\uparrow} h_{ij\downarrow} - h^\dagger_{ij\uparrow} e_{ij\downarrow} \right) + \mathrm{h.c.} \Bigg] , \end{aligned} \tag{1.27}$$

where each site (i, j) has two orbitals: the electron-like orbital $e_{ij\sigma}$ and the hole-like orbital $h_{ij\sigma}$. This enables us, after partially transforming the Hamiltonian, to plot the band structure on a nanoribbon, as we observed for the KM model and silicene as shown in Fig. 1.8. We set $a = 1$, $A = 5$, $B = -1$, $M = -2$, $C = D = 0$ and $\Delta = 0.3$. Note that the crossing of the edge states occurs at the TRIM $k_y = 0$ and BIA does not break the particle-hole symmetry.

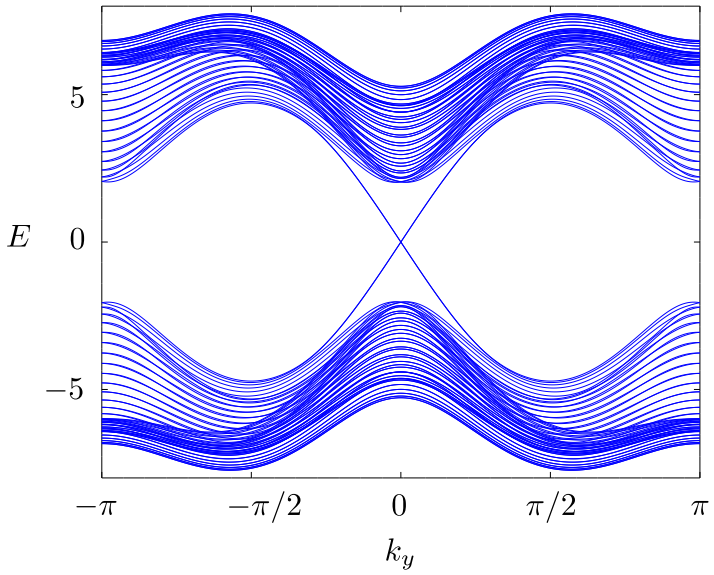

Figure 1.8: The energy spectrum of the BHZ Hamiltonian and BIA for a nanoribbon of L=32 unit cells. We set $a = 1$, $A = 5$, $B = -1$, $M = -2$, $C = D = 0$ and $\Delta = 0.3$.

Historically, the HgTe heterostructure was the first experimental realization of 2D TI in 2007 [12]. König et al. manufactured different sizes and thicknesses of heterostructures by molecular beam epitaxy. They measured the resistance for a four terminal Hall bar when the Fermi energy is tuned by the gate voltage V_g into the bulk gap. The results can be seen in Fig. 1.9 [12]. If the system is in the trivial regime (I), $d < d_c$, and the resistance is very high, which is what is expected of a normal insulator. If the system is larger than the critical width (III) & (IV), the resistance is quantized to $R = h/(2e^2)$, which is what we expect for ballistic edge states. It is also the case in the inset for different temperatures. Nonetheless if the length is longer than the mean free path (II), the resistance deviates from the quantized value due to the disorder. Other transport measurements, including non-local resistance measurements, were performed confirming the presence of edge modes [57–60]. Finally, another proof of the existence of edge states in the TI regime was provided by experiments unsig a superconducting quantum interference device (SQUID) [61, 62]. A superconducting loop scans the device, and measures the magnetic field induced by the current. Inverting the Biot-Savart law, the current density can be extracted enabling us to image of the current in the sample. It is also possible to spatially visualize the edge states via scanning gate microscopy [63].

1.4.2.1 InAs/GaSb heterostructures

Another similar structure to HgTe heterostructure is the one formed from a layer of InAs and a layer of GaSb sandwiched between two layers of AlSb. This heterostructure was theoretically proposed in 2008 [15]. It is possible to derive an effective Hamiltonian

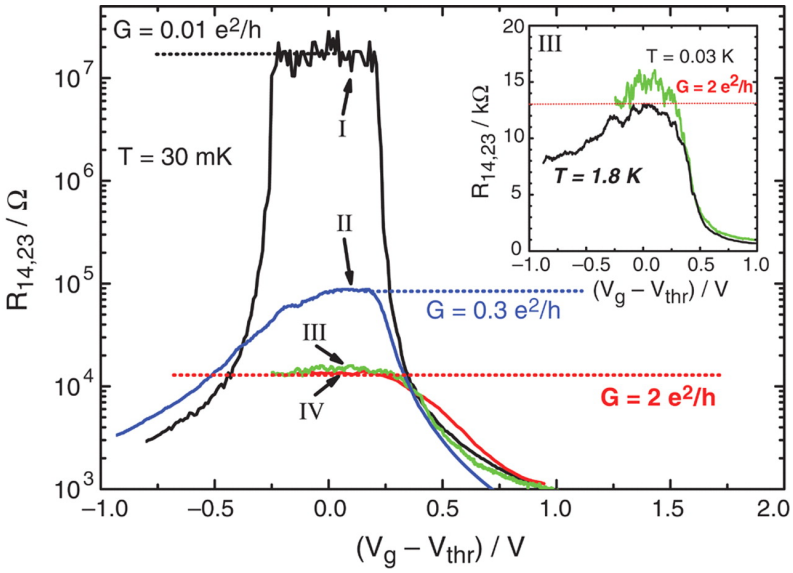

Figure 1.9: Resistance (conductance) measurements in the trivial regime (I), where the resistance is maximal showing a gap and in the inverted regime (II, III & IV), where the conductance should always be $G = 2e^2/h$. In the insert, several resistance measurements at different temperature. Taken from Ref. [12].

similar to the BHZ Hamiltonian (1.23). In this case, the trivial and non-trivial regimes are not only governed by the width of the central layer(s), but also the back voltage which enables us to switch between the two regimes, creating a more versatile tool for studying a topological phase transition. Secondly, neither of the two central layers have a band inversion in the central layer as shown in Fig. 1.10. It is the broken gap of the heterojunction which creates an inversion of the band. This leads to a spatial separation between the two bands, where the electron-like band is more localized in the InAs layer whereas the hole-like band is more localized in the GaSb layer. Additional terms appear due to the lack of structural and bulk inversion symmetry [15], which couples again the two spin blocks.

$$\mathcal{H}_{\mathrm{BIA}}(\mathbf{k}) = \begin{pmatrix} 0 & 0 & \Delta_e(k_x + ik_y) & -\Delta_0 \\ 0 & 0 & \Delta_0 & \Delta_e(k_x - ik_y) \\ \Delta_e(k_x - ik_y) & \Delta_0 & 0 & 0 \\ -\Delta_0 & \Delta_h(k_x + ik_y) & 0 & 0 \end{pmatrix}, \tag{1.28}$$

$$\mathcal{H}_{\mathrm{SIA}}(\mathbf{k}) = \begin{pmatrix} 0 & 0 & i\xi_e(k_x - ik_y) & 0 \\ 0 & 0 & 0 & 0 \\ -i\xi_e^*(k_x + ik_y) & 0 & 0 & 0 \\ 0 & 0 & 0 & 0 \end{pmatrix}, \tag{1.29}$$

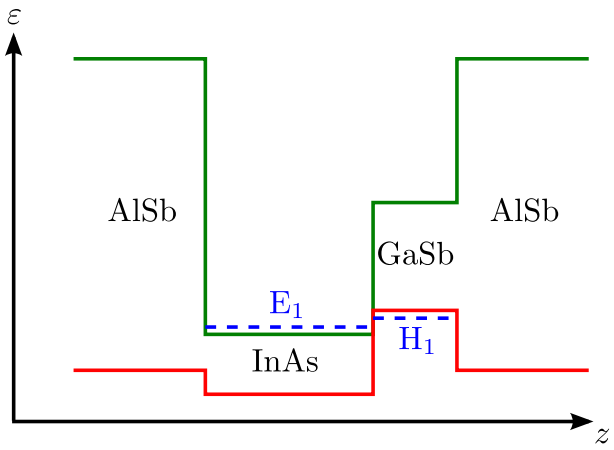

Figure 1.10: Band structure in the z-direction. The conduction band is indicated in each layer in green and the valence band is indicated in red. The (dashed) blue line shows the effective inverted bands representing electron-like and hole-like behavior near the Γ-point.

where Δ_0, Δ_e, Δ_h and ξ_e are material parameters. Note that BIA is nearly negligible in such a heterostructure [64], but the Rashba SOC seems to play an important role [65], More on this topic and on InAs/GaSb heterostructures will be presented in Chap. 4. After this theoretical prediction, experimental evidence of QSHE through transport measurements were first found in 2011 [13]. In the following years, other transport measurements were made on this heterostructure to confirm the presence of edge states [66–73]. In a similar manner as in the HgTe heterostructures, SQUID measurements were able to image current densities [74]. Very recently, evidence of trivial edge states, i.e. edge states remaining also in the trivial regime appeared using both transport and SQUID measurements [75, 76].

1.5 Generic helical edge states

In the models and materials presented above, several mechanisms were responsible for breaking the axial spin symmetry either intrinsically or extrinsically. It is therefore necessary to develop a more general framework, where only time-reversal symmetry is assumed. In this framework, the edge states are called generic helical edge states [17]. They are still characterized by their helicity, but they are no longer eigenstates of the spin operator. Using time-reversal symmetry, the right-moving edge state $\psi_+(k)$ in a translation-invariant system is linked to the left-moving edge states $\psi_-(k)$ through:

$$\begin{aligned} T\psi_+(k)T^{-1} &= \psi_-(-k), \\ T\psi_-(k)T^{-1} &= -\psi_+(-k), \end{aligned} \tag{1.30}$$

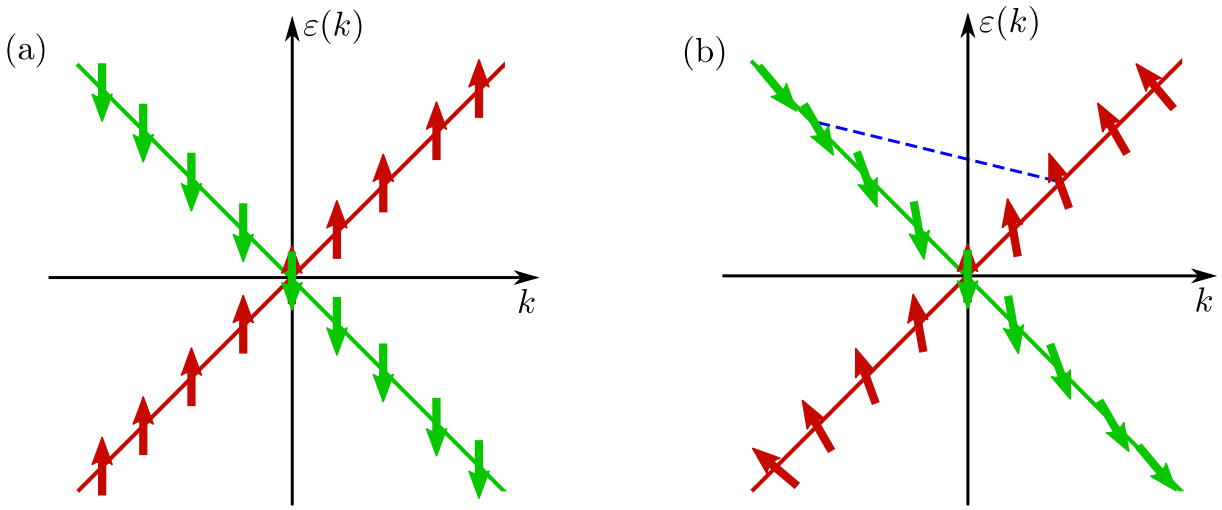

Figure 1.11: A sketch of the edge state dispersions plotted with respect to momentum. In panel (a), the axial spin symmetry is preserved, leading to orthogonal edge states at any momenta. In panel (b), the axial spin symmetry is broken, leading to a possible overlap for the edge states when their momenta differ.

where T is the anti-unitary time-reversal operator. Elastic backscattering is still not allowed: a term such as $\psi_+^\dagger(k)\psi_-(k) + \text{h.c.}$ would violate time-reversal symmetry. Moreover, due to Kramers' theorem, any overlap at the same energy would vanish, for example $\langle\psi_-(-k)|\psi_+(k)\rangle = 0$.

Nevertheless, new processes such as inelastic scattering induced by electron-electron interactions are now allowed. The overlap for states with different momenta can be finite [17, 77, 78], even if time-reversal symmetry is preserved. An example of such a case can be seen in Fig. 1.11. In panel (a), the edge states are indeed spin eigenvalues. The overlap is zero by construction, independent of momentum and inelastic backscattering is forbidden. In panel (b), the edge states no longer have any axial spin symmetry. Therefore, the overlap vanishes if the modulus of their momenta is equal due to TR-symmetry, i.e. $\langle\psi_-(\pm k)|\psi_+(k)\rangle = 0$, but it might not be the case at other momenta. Such a finite overlap between states of different momenta, such as those joined by the dashed blue line in Fig. 1.11 enables new processes. It can lead to new phenomena, such as a correction of the conductance at finite temperature [17, 79] or new interference effects in transport calculations [80, 81].

It is possible to relate the chiral basis $(\psi_+(k), \psi_-(k))^T$ to the spin basis $(\psi_\uparrow(k), \psi_\downarrow(k))^T$ at any momentum k through a SU(2) momentum-dependent matrix B_k,

$$\begin{pmatrix}\psi_\uparrow(k)\\ \psi_\downarrow(k)\end{pmatrix} = B_k \begin{pmatrix}\psi_+(k)\\ \psi_-(k)\end{pmatrix}. \tag{1.31}$$

B_k is only determined by unitarity and time-reversal symmetry. Its most generic form is

$$B_k = \begin{pmatrix} \cos(\theta_k) & -\sin(\theta_k) \\ \sin(\theta_k) & \cos(\theta_k) \end{pmatrix}, \tag{1.32}$$

where θ_k measures the rotation of the spin axis at the value of k. θ_k should be even in k, due to time-reversal symmetry. We can set the direction of the spin axis, such that $B_0 = \mathbb{1}_{2\times 2}$ at the Dirac point $k = 0$. If we expand B_k up to k^2, we find

$$B_k \approx \begin{pmatrix} 1 & -(k/k_0)^2 \\ (k/k_0)^2 & 1 \end{pmatrix}, \tag{1.33}$$

where k_0 can be understood as the characteristic scale for the rotation of the spin quantization axis. k_0 is a central concept in this thesis as it enables us to obtain some information about the spin texture and it can be quantified. Here, the spin texture describes the spin axis orientations in the edge states.

1.6 Outline

The remaining parts of this thesis are organized in the following manner. In the next chapter, we will start by describing how to extract the spin texture in a translational invariant system. As the system needs some boundary with a trivial system to get edge states, we focus our study on nanoribbons. This will enable us to extract the first information about nontrivial spin textures. Nonetheless, nanoribbons and translation invariant systems are not very realistic systems for more concrete measurements. We go on to probe how the nontrivial spin texture is expressed in real space. We will start by considering a rotationally invariant disk. We discover that in such system we can replace the lattice momentum by the total angular momentum. It is still possible to argue that such systems still preserve some spatial symmetry. Therefore, the last step will be to explore the spin texture in the absence of any spatial symmetry, i.e. in flakes. We will be able to show that the spin textures in nanoribbons and in disks or flakes coincide. Finally, as the spin texture can be extracted locally, we will investigate its spectroscopic properties.

In chapter 3, we study a Hall bar transport setup using our prior knowledge of the spin texture in (angular) momentum space. With the help of an antidot (i.e. a hole in the middle of the Hall bar), we will probe the spin texture in two cases: either neglecting Coulomb interaction for the electrons located on the antidot, or considering the Coulomb blockade regime. In the first case, we will use Landauer-Büttiker formalism to compute the (non)local resistance and understand the role of the spin texture. The results will

be compared to numeric calculations. In the second case, we will use Fermi's golden rule to compute the current flowing through the antidot in the sequential and cotunneling regimes. We will be able to detect a direct change of the tunneling current due to the nontrivial spin texture if the antidot is in the cotunneling regime.

Finally in chapter 4, we will focus on InAs/GaSb heterostructures. We will start with a small introduction about $k \cdot p$ theory and how to apply it to heterostructures. From the $k \cdot p$ Hamiltonian, we will derive an effective two-dimensional Hamiltonian, considering perturbatively the terms with components perpendicular to the growth direction. This Hamiltonian will exhibit anisotropies, therefore we expect that the band structure will be influenced by the crystallographic direction of measurement. We then compute the band structure for nanoribbons in different orientations. From there, we will apply the same method as in chapter 2 and extract the spin texture. We show that the spin texture will depend explicitly on the crystallographic orientation of the nanoribbons.

We summarize the findings presented in this thesis and propose new possible avenues of research and remaining open questions in chapter 5.

2 | Spin texture of generic helical edge states

After presenting the essential concepts relevant for this thesis, we first focus on the notion of generic helical edge states. We realized in Eq. (1.31) that it was possible to relate the chiral basis to a spin basis through a momentum-dependent matrix B_k. Therefore, B_k enables us to extract information about the spin texture. However, it is not possible to extract directly the matrix numerically, but we can extract k_0. To do so, one approach is to consider the scattering of edge states propagating in opposite directions on a nanoribbon similar to the one in Fig. 1.4, where the edges are parallel to the y direction. In the case of an impurity localized at (x_0, y_0), which generates a potential that has a wavelength shorter than the Fermi wavelength, but larger than the penetration length, the backscattering Hamiltonian can be expressed as $V_0\delta(y - y_0)$. By comparing it in the chiral basis with the Hamiltonian which originates from an impurity violating translation invariance, we get [17]

$$\left[B_{k_2}^\dagger B_{k_1}\right]^{-+} = \int dx\, \psi_{-,k_2}^*(x, y_0)\, \psi_{+,k_1}(x, y_0). \tag{2.1}$$

Near the Dirac point, the low-momentum expansion from Eq. (1.33) enables us to make the following approximation

$$\left[B_{k_2}^\dagger B_{k_1}\right]^{-+} \approx k_0^{-2} \left(k_1^2 - k_2^2\right). \tag{2.2}$$

We have now means of obtaining some information about the spin texture. Most of the results presented in this chapter were published in Ref. [77].

2.1 Extracting the spin texture in momentum space

In order to extract the numerical value of k_0, we have to modify slightly our expression for the spin texture by adding the modulus

$$\mathcal{K}(k_1, k_2) = \left| \int dx\, \psi^{\dagger}_{-,k_2}(x, y_0)\, \psi_{+,k_1}(x, y_0) \right| \approx k_0^{-2} \left| k_1^2 - k_2^2 \right| . \tag{2.3}$$

The absolute value makes this expression gauge invariant. When we extract the wave function of the edge states in our nanoribbon geometry, we need to diagonalize the Hamiltonian at each momentum k. This adds an overall $U(1)$ phase for each eigenfunction: this phase will be the same for the eigenfunctions at a given momentum, but the diagonalization procedure does not set the phase between two eigenfunctions at different momenta. We expect the spin texture to have the following properties:

- If there is no term mixing the spins, such as structural or bulk inversion asymmetry, the spin texture cannot be found, i.e. $\mathcal{K}(k_1, k_2) = 0$ for all k_1, k_2.
- Its strength will be determined by the value taken by k_0^{-2}.
- At $k_1 = k_2$, the spin texture vanishes, i.e. $\mathcal{K}(k_1, k_1) = 0$ for all k_1. The two eigenfunctions come from the same diagonalization procedure, they will be orthogonal by construction.
- At $k_1 = -k_2$, the spin texture also vanishes, i.e. $\mathcal{K}(k_1, -k_1) = 0$ for all k_1. The two eigenfunctions are TR-partners, thus they are orthogonal due to Kramers' theorem.
- Near the Dirac point ($E = 0$), the spin texture should behave as $\mathcal{K}(k_1, k_2) \approx k_0^{-2} |k_1^2 - k_2^2|$.

We will see in the next sections how to generalize the spin texture $\mathcal{K}(k_1, k_2)$, when we lose translation invariance.

Practically, we implement the KM model (1.10) or BHZ model with BIA (1.27) on a nanoribbon in the same manner we already did for Figs. 1.5 and 1.8. During the diagonalization procedure, we get the energy and the eigenvalues $\psi_{\pm,k_i}(x, y_0)$. We can assume that $y_0 = 0$, since the system is translation symmetric. Then the integral (2.3) can be directly computed by summing each overlap along the x-axis (the integral is changed to a sum, as there are a finite number of sites in the x-direction). The spin texture for the BHZ model is shown in Fig. 2.1. We use the same parameters as in Fig. 1.8 except for the BIA parameter set at $\Delta = 0.5$. It is totally symmetric with respect to momentum, showing a hyperbolic structure. This symmetry is not surprising, as the BHZ Hamiltonian with BIA preserves particle-hole symmetry.

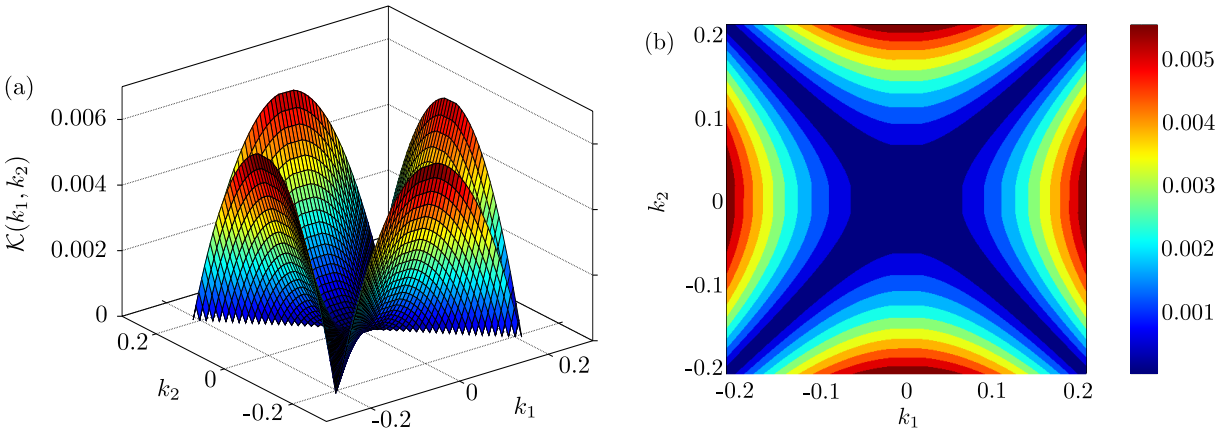

Figure 2.1: The spin texture of the BHZ Hamiltonian including BIA for a nanoribbon of L=32 unit cells. We set $a = 1$, $A = 5$, $B = -1$, $M = -2$, $C = D = 0$ and $\Delta = 0.5$. In panel (a), we have the three-dimensional plot and in panel (b), the corresponding contour plot.

We can extract in the same manner the spin texture for the KM Hamiltonian, where the spin mixing is created by Rashba SOC $\lambda_{\mathrm{R},1}$. In this case, the texture is shown in Fig. 2.2. We use the same parameters as in Fig. 1.5. We observe a small asymmetry where the spin texture deviates at large k from the perfect hyperbolic structure. Note that the full Hamiltonian is not particle-hole symmetric. Nonetheless, at low energy, the quadratic structure of the spin texture remains a good approximation and can still be used to evaluate the value of k_0^{-2}.

The effect of the intrinsic Rashba SOC term written in Eq. (1.20), which appears in materials such as silicene, can also lead to a nontrivial spin texture. From the same parameters used in Fig. 1.6, we can plot the spin texture. They are shown in Fig. 2.3 and in contrast to the spin texture with the extrinsic Rashba SOC $\lambda_{\mathrm{R},1}$, it is this time symmetric, as the full Hamiltonian preserves particle-hole symmetry. Nonetheless, the intrinsic Rashba SOC has a weaker effect, as there is a factor of 10 between the magnitudes of the two Rashba SOC in Figs. 2.2 and 2.3.

To extract the spin texture, we need to get the numerical value of k_0^{-2}. We used two methods, which led to similar conclusions and parameter values. The first method is to take the fits at constant value of k_1 (or k_2), where the only fitting parameter is the constant in front of $|k_1^2 - k_2^2|$ and we average the fitting values to get k_0. The other method is to directly perform a two-dimensional fit on the spin texture. If we start with the BHZ Hamiltonian, we can get the scaling of k_0^{-2} with respect to the BIA parameter Δ,

$$k_0^{-2} \propto |\Delta|, \tag{2.4}$$

which is independent of the length of the ribbon as we can see in Fig. 2.4. We used same

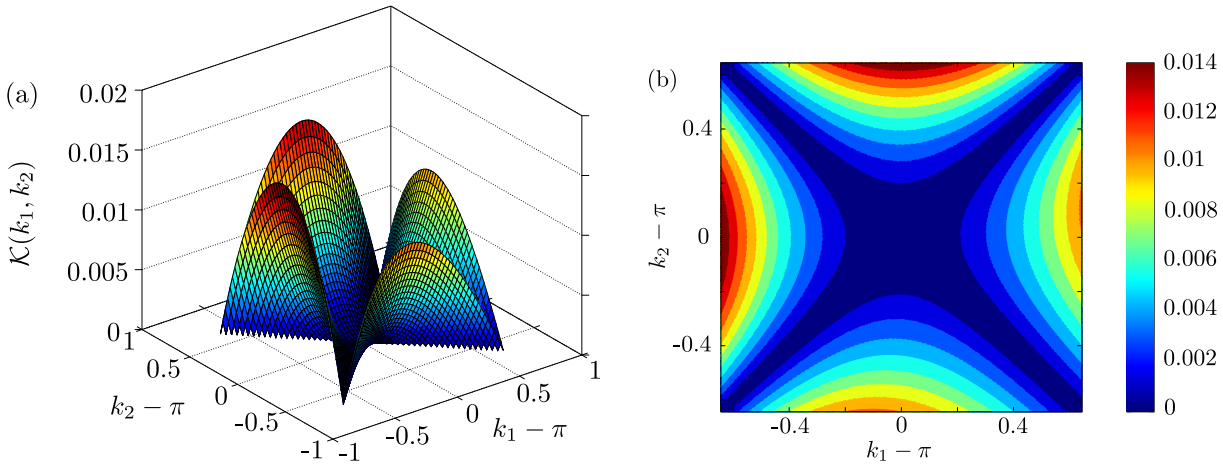

Figure 2.2: The spin texture of the KM Hamiltonian for a nanoribbon of L=32 unit cells. We set $a = 1$, $t = 1$, $\lambda_{\mathrm{SO}} = 0.2$ and $\lambda_{\mathrm{R},1} = 0.05$. In panel (a), we have the three-dimensional plot and in panel (b), the corresponding contour plot.

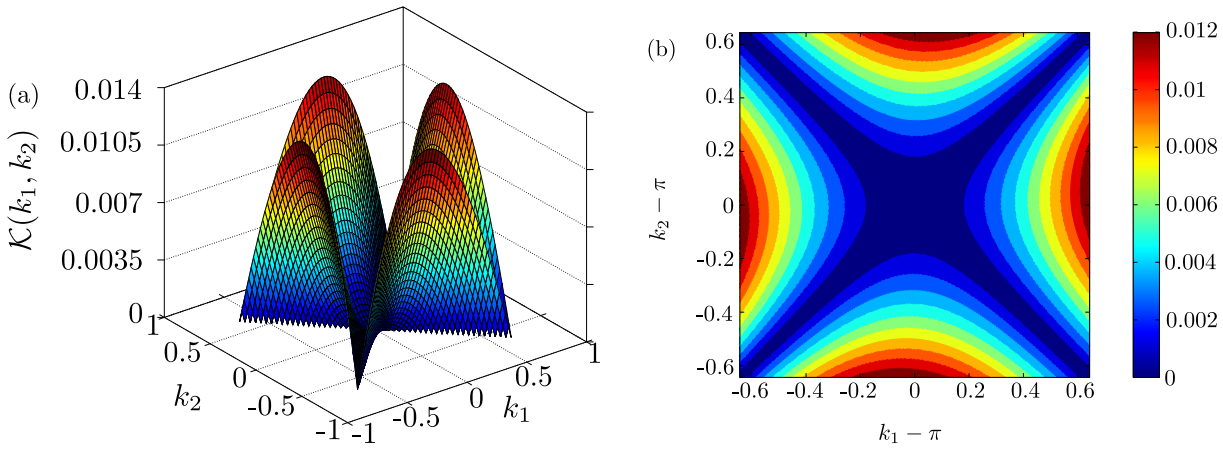

Figure 2.3: The spin texture of silicene, i.e. the KM Hamiltonian with the $\lambda_{\mathrm{R},2}$-term, for a nanoribbon of L=32 unit cells. We set $a = 1$, $t = 1$, $\lambda_{\mathrm{SO}} = 0.2$, $\lambda_{\mathrm{R},1} = 0$ and $\lambda_{\mathrm{R},2} = 0.5$. In panel (a), we have the three-dimensional plot and in panel (b), the corresponding contour plot.

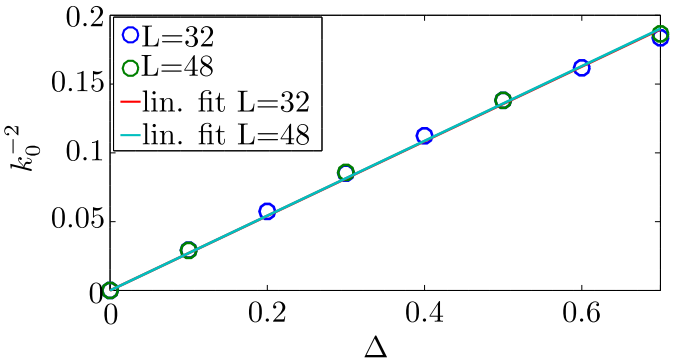

Figure 2.4: Parameter dependence for k_0^{-2} in the BHZ Hamiltonian including BIA for a nanoribbon of L=32 unit cells. We set $a = 1$, $A = 5$, $B = -1$, $M = -2$, $C = D = 0$.

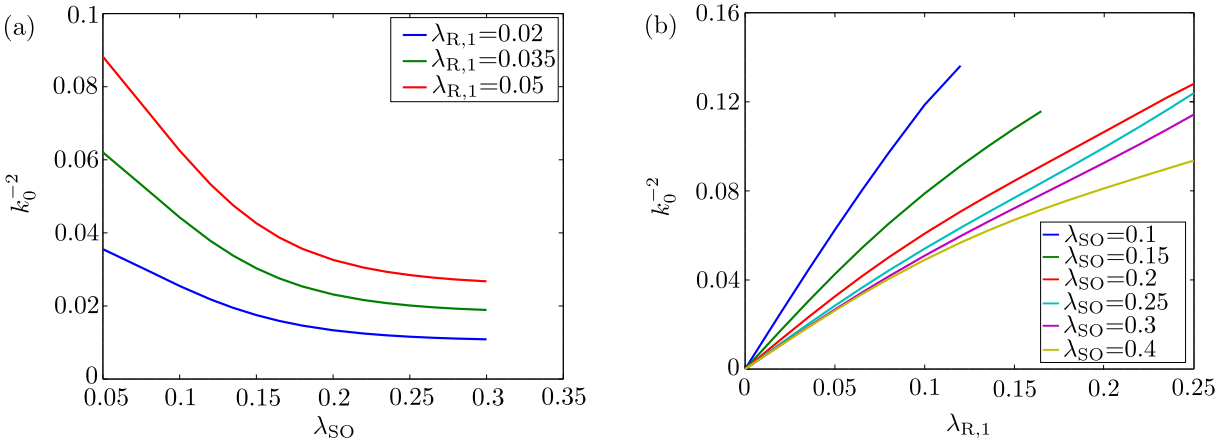

Figure 2.5: Parameter dependence for k_0^{-2} in the KM Hamiltonian for nanoribbons of L=32 as function of λ_{SO} (a) and $\lambda_{R,1}$ (b). We set $a = 1$, $t = 1$.

parameters as before ($a = 1$, $A = 5$, $B = -1$, $M = -2$, $C = D = 0$).

Regarding the KM Hamiltonian, we have two parameters which can influence the extracted value of k_0^{-2}: the intrinsic SOC and the extrinsic Rashba SOC. k_0 scales with the modulus of Rashba SOC and as the inverse square root of the intrinsic SOC modulus

$$k_0^{-2} \propto \frac{|\lambda_{R,1}|}{\sqrt{|\lambda_{SO}|}}. \tag{2.5}$$

This scaling can be seen in Fig. 2.5, where the parameters are kept similar in comparison to the previous plots ($a = 1$, and $t = 1$).

For silicene, germanene and stanene, we decide to compute realistic values of k_0^{-2}, but we exclude the extrinsic Rashba SOC. This can be justified as the extrinsic one can be tuned with an external electric field and its maximal value remains much weaker [55]. If we use the parameters from first principles computations [54], we get the results which are summarized on Table 2.1. We can see that for heavier elements such as germanium

	$k_0^{-2}\tilde{a}^{-2}$	$k_0\tilde{a}$
Silicene	$2.4341 \cdot 10^{-7}$	2027
Germanene	$6.8594 \cdot 10^{-5}$	121
Stanene	$1.0282 \cdot 10^{-4}$	99

Table 2.1: Values of k_0^{-2} and k_0 multiplied with $\tilde{a} = \sqrt{3}a$, the distance between two unit cells, for silicene, germanene and stanene. The system parameters are taken from Ref. [54] and the effect of extrinsic Rashba SOC is not considered.

or tin, the full rotation happens for a length of about 100 Brillouin zones.

We have now a good understanding of the spin texture on a nanoribbon, where the dependence on momentum is clearly stated. We have an explicit procedure to extract this information. We also determined the dependence on material parameters for different models and offered some realistic values of the spin texture. Note that results for the BHZ model with structural inversion asymmetry, Eq. (1.29), were published in Ref. [78].

2.2 Extracting the spin texture in a real space: continuum disks

Nonetheless, the notion of nanoribbon and momentum is not clear in an experimental realization. As we saw in Sec. 1.4, most of the experiments were made to measure some transport properties using Hall bars. Translation symmetry is lost and there is not necessarily any other spatial symmetry. The first step is to understand the spin texture when the rotational symmetry is still preserved, using disks.

To analyze these TIs disks, we use the continuous version of the BHZ model from Eq. (1.23) and bulk inversion asymmetry from Eq. (1.26). The latter is responsible for the nontrivial spin texture as we realized in the previous section. To have no penetration of the edge states in the surrounding media [82], we assume that the disk is surrounded by vacuum (i.e. the TI is surrounded by an infinite potential) as shown in Fig. 2.6. The edge states then counterpropagate at the radius R, the boundary between the TI disk and the infinite potential.

Circular geometry for TI was also studied in other works. In Ref. [83], Michetti and Recher investigated the energy spectrum as well as the wave functions for Aharonov-Bohm rings and disks using the BHZ model, Eq. (1.23), and structural inversion asymmetry, Eq. (1.29). The case of an antidot (an infinite TI with a circular hole in its middle) using only the BHZ model was also studied in Ref. [84]. Ref. [85] used the KM model for silicene where disks with and without intrinsic spin-orbit coupling were investigated under a magnetic field. Finally, short cylinders of three-dimensional TI were investigated

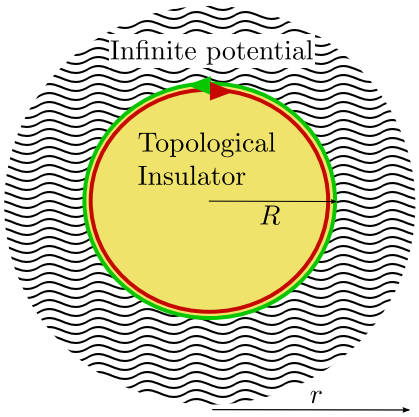

Figure 2.6: Sketch of the TI disk, surrounded by an infinite potential. R labels the radius of the disk, whereas r denotes the radial distance. The edge states are (counter)clockwise propagating at the boundary between the two media.

in Ref. [86].

As mentioned above, we use the BHZ model, Eq. (1.23), with bulk inversion asymmetry, Eq. (1.26). We set $C = D = 0$ as these material parameters do not interfere with the topological nature of the TI disk, but merely break the particle-hole symmetry. We need to transform from the momentum space representation of the Hamiltonian to real space by replacing $k_x = -i\partial_x$ and $k_y = -i\partial_y$. The Hamiltonian becomes

$$\begin{aligned}\mathcal{H} &= \mathcal{H}_{\mathrm{BHZ}} + \mathcal{H}_{\mathrm{BIA}} \\ &= -iA(\partial_x\sigma_x \otimes s_z - \partial_y\sigma_y \otimes \mathbb{1}_{2x2}) + (M + B\partial_x^2 + B\partial_y^2)\sigma_z \otimes \mathbb{1}_{2x2} + \Delta\sigma_y \otimes s_y.\end{aligned} \tag{2.6}$$

As the system is rotationally invariant, it is advantageous to transform the coordinates into the polar ones $x = r\cos(\phi)$, $y = r\sin(\phi)$. The partial derivatives become $\partial_x = \cos(\phi)\partial_r - i\frac{\sin(\phi)}{r}l_z$, $\partial_y = \sin(\phi)\partial_r + i\frac{\cos(\phi)}{r}l_z$, where $l_z = -i\partial_\phi$ is the orbital angular momentum. The bulk inversion asymmetry term is not affected by this change of coordinate, but the BHZ Hamiltonian now reads

$$\begin{aligned}\mathcal{H}_{\mathrm{BHZ}} = -A\left(e^{i\phi\sigma_z\otimes s_z} i\partial_r\sigma_x \otimes s_z + e^{i\phi\sigma_z\otimes s_z}\frac{l_z}{r}\sigma_y \otimes \mathbb{1}_{2x2}\right) \\ + \left(M + B\partial_r^2 - B\frac{l_z^2}{r^2} + B\frac{\partial_r}{r}\right)\sigma_z \otimes \mathbb{1}_{2x2}.\end{aligned} \tag{2.7}$$

Note that the system does not commute with the orbital angular momentum l_z. We define a total angular momentum j_z, such that

$$j_z = l_z - \frac{1}{2}(\sigma_z s_z). \tag{2.8}$$

This angular momentum commutes with the Hamiltonian $[\mathcal{H}, j_z] = 0$, therefore there

exists a basis where the elements are both eigenstates of the Hamiltonian and of the total angular momentum operator. This basis fulfills

$$j_z \Psi_j(r,\phi) = j\Psi_j(r,\phi). \tag{2.9}$$

When this differential equation is solved and the periodicity is set, the angular part of the wave function is completely established. The differential equation leads to

$$\begin{pmatrix} \Psi_{jE_1+}(r,\phi) \\ \Psi_{jH_1+}(r,\phi) \\ \Psi_{jE_1-}(r,\phi) \\ \Psi_{jH_1-}(r,\phi) \end{pmatrix} = e^{ij\phi} \begin{pmatrix} \Psi_{jE_1+}(r)e^{i\phi/2} \\ \Psi_{jH_1+}(r)e^{-i\phi/2} \\ \Psi_{jE_1-}(r)e^{-i\phi/2} \\ \Psi_{jH_1-}(r)e^{i\phi/2} \end{pmatrix}. \tag{2.10}$$

The periodicity of the wave function imposes $\Psi_j(r,\phi) = \Psi_j(r,\phi+2\pi)$, such that j is a half-integer, $j+1/2 \in \mathbb{Z}$.

Solving the radial part requires more sophistry. To start with, we apply the Hamiltonian to the wave function $\mathcal{H}\Psi_j(r,\phi) = E\Psi_j(r,\phi)$, creating the following set of equations:

$$\begin{aligned}
&\left(M + B\partial_r^2 - B\frac{(j+1/2)^2}{r^2} + B\frac{1}{r}\partial_r - E\right)\Psi_{jE_1+}(r) \\
&+ Ai\left(-\partial_r + \frac{j-1/2}{r}\right)\Psi_{jH_1+}(r) - \Delta\Psi_{jH_1-}(r) = 0 \\
&Ai\left(-\partial_r - \frac{j+1/2}{r}\right)\Psi_{jE_1+}(r) + \Delta\Psi_{jE_1-}(r) \\
&+ \left(-M - B\partial_r^2 + B\frac{(j-1/2)^2}{r^2} - B\frac{1}{r}\partial_r - E\right)\Psi_{jH_1+}(r) = 0 \\
&\Delta\Psi_{jH_1+}(r) + Ai\left(\partial_r + \frac{j+1/2}{r}\right)\Psi_{jH_1-}(r) \\
&+ \left(M + B\partial_r^2 - B\frac{(j-1/2)^2}{r^2} + B\frac{1}{r}\partial_r - E\right)\Psi_{jE_1-}(r) = 0 \\
&- \Delta\Psi_{jH_1-}(r) + Ai\left(\partial_r - \frac{j-1/2}{r}\right)\Psi_{jE_1-}(r) \\
&+ (-M - B\partial_r^2 + B\frac{(j+1/2)^2}{r^2} - B\frac{1}{r}\partial_r - E)\Psi_{jH_1-}(r) = 0.
\end{aligned} \tag{2.11}$$

The ansatz for each radial component is

$$\Psi_{j\alpha}(r) = \Psi_{j\alpha} Z_j(\sqrt{p}r), \tag{2.12}$$

where Z_j is a Bessel function of the first or second kind, or a Hankel function, depending

on the boundary conditions. α encodes the subband and the spin degrees of freedom $\alpha = \{E_1/H_1, \pm\}$. The Bessel functions above obey the following useful recursion relation [87]

$$\sqrt{p}Z_{j\pm1}(\sqrt{p}r) = \frac{j}{r}Z_j(\sqrt{p}r) \mp \partial_r Z_j(\sqrt{p}r). \tag{2.13}$$

It enables us to eliminate all the differential parts from the coupled equations as

$$\left(\partial_r^2 - \frac{j^2}{r^2} + \frac{1}{r}\partial_r\right) Z_j(\sqrt{p}r) = \left(\partial_r + \frac{j+1}{r}\right)\left(\partial_r - \frac{j}{r}\right) Z_j(\sqrt{p}r) = -pZ_j(\sqrt{p}r). \tag{2.14}$$

We have now only linear coupled equations, which can be compactly rewritten into a matrix equation.

$$\begin{pmatrix} M-Bp-E & Ai\sqrt{p} & 0 & -\Delta \\ -Ai\sqrt{p} & -M+Bp-E & \Delta & 0 \\ 0 & \Delta & M-Bp-E & Ai\sqrt{p} \\ -\Delta & 0 & -Ai\sqrt{p} & -M+Bp-E \end{pmatrix} \begin{pmatrix} \Psi_{jE_1+} \\ \Psi_{jH_1+} \\ \Psi_{jE_1-} \\ \Psi_{jH_1-} \end{pmatrix} \equiv \tilde{\mathcal{H}}\vec{\Psi} = 0. \tag{2.15}$$

Our solutions appear when the determinant of the matrix vanishes, $\det(\tilde{\mathcal{H}}) = 0$. It yields the following characteristic polynomial:

$$\left[(M-Bp)^2 - E^2 + \Delta^2 + A^2p\right]^2 - 4\Delta^2A^2p = 0\ . \tag{2.16}$$

The four roots of this quartic polynomial equation are labeled p_n, $n = 1, 2, 3, 4$. Note that if $\Delta = 0$, $\tilde{\mathcal{H}}$ is now formed of two identical blocks and p_n is doubly degenerate. The closed form of these roots can be expressed as functions of A, B, M, Δ and E, but we omit them here as the expressions are very lengthy.

One of the boundary condition should be that the wave function should not diverge at $r = 0$. This constraint requires a Bessel function of the first kind, labeled $J_j(\sqrt{p}r)$. The full wave function can be expressed as

$$\Psi_j(r,\phi) = \sum_n A_n e^{ij\phi} \begin{pmatrix} i\dfrac{(M-Bp_n)^2 - E^2 + \Delta^2 - A^2p_n}{2A\sqrt{p_n}(M-Bp_n-E)} J_{j+1/2}(\sqrt{p_n}r)e^{i\phi/2} \\ J_{j-1/2}(\sqrt{p_n}r)e^{-i\phi/2} \\ \dfrac{(M-Bp_n)^2 - E^2 - \Delta^2 + A^2p_n}{2\Delta(M-Bp_n-E)} J_{j-1/2}(\sqrt{p_n}r)e^{-i\phi/2} \\ i\dfrac{(M-Bp_n)^2 - E^2 + \Delta^2 + A^2p_n}{2\Delta A\sqrt{p_n}} J_{j+1/2}(\sqrt{p_n}r)e^{i\phi/2} \end{pmatrix}, \tag{2.17}$$

where A_n are constant parameters to ensure the normalization of the wave function. The

TI regime is respected by the chosen values of the parameters A, B, M and Δ. Moreover, E should be smaller than M to have solutions for the edge states. The second boundary condition enables us to find the energy: the wave function should vanish at the boundary between the TI disk and the vacuum $\Psi_j(r = R, \phi) = 0$. This condition on the wave function leads to a null determinant for the following coefficient matrix:

$$\det \begin{pmatrix} \zeta_1 J_{j+1/2}(\sqrt{p_1}R) & \zeta_2 J_{j+1/2}(\sqrt{p_2}R) & \zeta_3 J_{j+1/2}(\sqrt{p_3}R) & \zeta_4 J_{j+1/2}(\sqrt{p_4}R) \\ J_{j-1/2}(\sqrt{p_1}R) & J_{j-1/2}(\sqrt{p_2}R) & J_{j-1/2}(\sqrt{p_3}R) & J_{j-1/2}(\sqrt{p_4}R) \\ \eta_1 J_{j-1/2}(\sqrt{p_1}R) & \eta_2 J_{j-1/2}(\sqrt{p_2}R) & \eta_3 J_{j-1/2}(\sqrt{p_3}R) & \eta_4 J_{j-1/2}(\sqrt{p_4}R) \\ \xi_1 J_{j+1/2}(\sqrt{p_1}R) & \xi_2 J_{j+1/2}(\sqrt{p_2}R) & \xi_3 J_{j+1/2}(\sqrt{p_3}R) & \xi_4 J_{j+1/2}(\sqrt{p_4}R) \end{pmatrix} = 0, \tag{2.18}$$

where the coefficients are

$$\zeta_n = \frac{(M - Bp_n)^2 - E^2 + \Delta^2 - A^2 p_n}{\sqrt{p_n}(M - Bp_n - E)}, \tag{2.19}$$

$$\eta_n = \frac{(M - Bp_n)^2 - E^2 - \Delta^2 + A^2 p_n}{(M - Bp_n - E)}, \tag{2.20}$$

$$\xi_n = \frac{(M - Bp_n)^2 - E^2 + \Delta^2 + A^2 p_n}{\sqrt{p_n}}. \tag{2.21}$$

By substituting numerical values of the parameters A, B, M and Δ, and choosing a disk size R as well as the value of the total angular momentum j, the determinant (2.18) gives only two solutions for the energy: one for $+E$ and one for $-E$. This is in perfect agreement with the particle-hole symmetry of the Hamiltonian. Using this energy and the numerical values of the parameters, we are able to plot the wave function. If the radius of the disk R increases, there are more energy levels with higher total angular momentum j in the bulk gap.

We plot the energy spectrum for several disk sizes R, two examples can be seen in Fig. 2.7. Each energy is doubly degenerate, as required by Kramers' theorem. For clarity, we focused only on clockwise-moving edge states in Fig. 2.7, where the highest energy level is labeled by $j = -13/2$ and the lowest one is labeled by $j = 13/2$. The counterclockwise edge states have the same spectrum, except that the value of the total angular momentum has the opposite sign. We observe that the levels are determined by the value of the energy as well as the value of the total angular momentum. When the disk is large enough, we find that the energy levels seem to increase with the same energy spacing. In contrast to an antidot [84], there is a minimal radius R where edge states start to appear. This behavior is reasonable, when the size of the disk is too small (of the order of the edge state penetration length) the edge states can overlap and gap out [88]. When the bulk inversion asymmetry is increased, we observe that the energy levels appear for smaller radii and

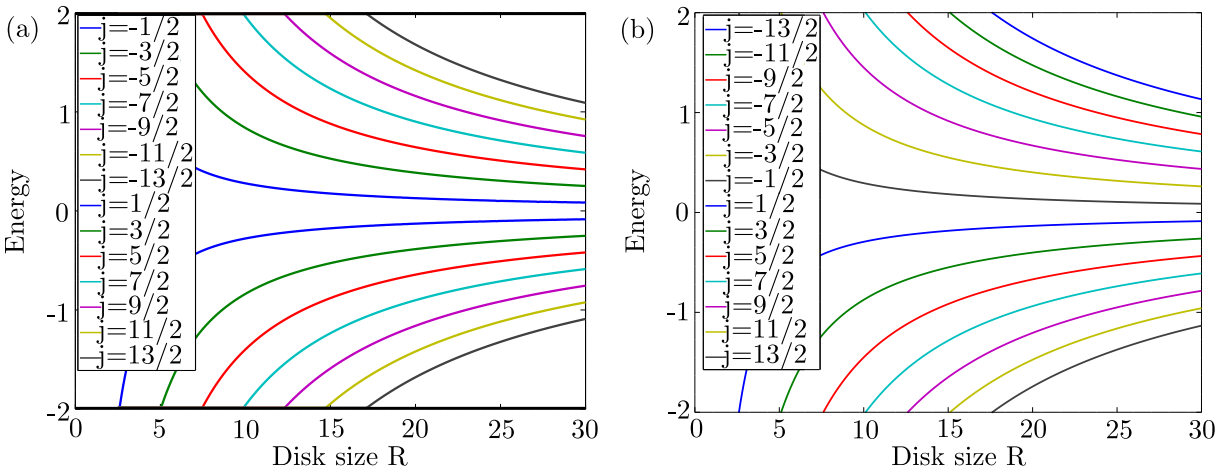

Figure 2.7: Energy spectrum of the clockwise-moving edge states as a function of R, for the parameters: $A = 5$, $B = -1$ and $M = -2$. In panel (a), we set $\Delta = 0.5$, whereas in panel (b), we have $\Delta = 0$.

the energy spacing is also smaller, as shown in Fig. 2.7. To check the consistency of our results, we also recovered the limit $\Delta \to 0$ shown in panel (b) of Fig. 2.7, in agreement what is expressed in Ref. [83].

Now that the energy level spectra are fully understood, we can focus on the wave functions and on their spatial distribution. The radial density $|\Psi_j(r, \phi = 0)|^2$ is directly obtained from Eq. (2.17), where the normalization is taken into account. Due to rotational symmetry, the value of the angle can be set to $\phi = 0$, since there is no preferred angular direction. The wave function should also vanish at the boundary and should be rather localized at the edge. The radial density for a disk size of $R = 30$ can be observed on Fig. 2.7. Surprisingly it has a rather significant penetration length. Note that we plot only the clockwise-moving wave functions, because the counterclockwise-moving eigenfunctions will be similar to those plotted. The only difference will come from the change of sign of the total angular momentum ($j \to -j$).

It is also possible to plot the spin-resolved radial densities, where the spin-resolved clockwise-moving eigenfunctions are shown in Fig. 2.9. The major component (on panel (a) in Fig. 2.9) of the wave function is the up-spin sector, whereas the minor component (on panel (b) in Fig. 2.9) is the down-spin sector. In the case of counterclockwise-moving edge states, the sign of the total angular momentum will be switched. Moreover, the major/minor component will switch spins, i.e. the major or minor component will now be the down-spin or the up-spin sector respectively. We can see that the total radial density is mainly composed by the majority spin density: there are 2 orders of magnitude in comparison with the minority spin density. Nevertheless, the latter penetrates deeper into the disk and its shape is rather different compared to the majority spin, as there is

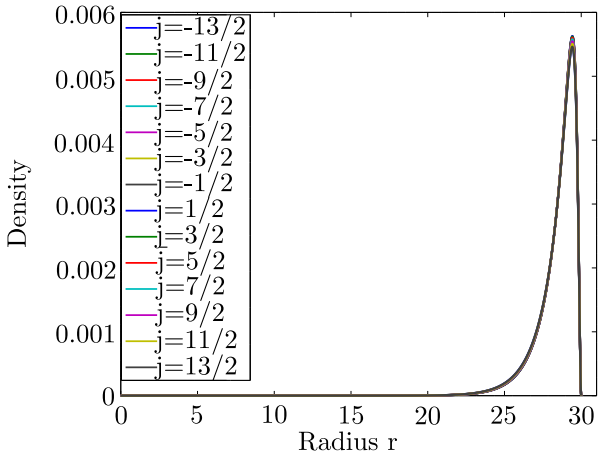

Figure 2.8: Probability density of the clockwise-moving edge states as a function of r for a disk size $R = 30$. The parameters are $A = 5$, $B = -1$, $M = -2$ and $\Delta = 0.5$.

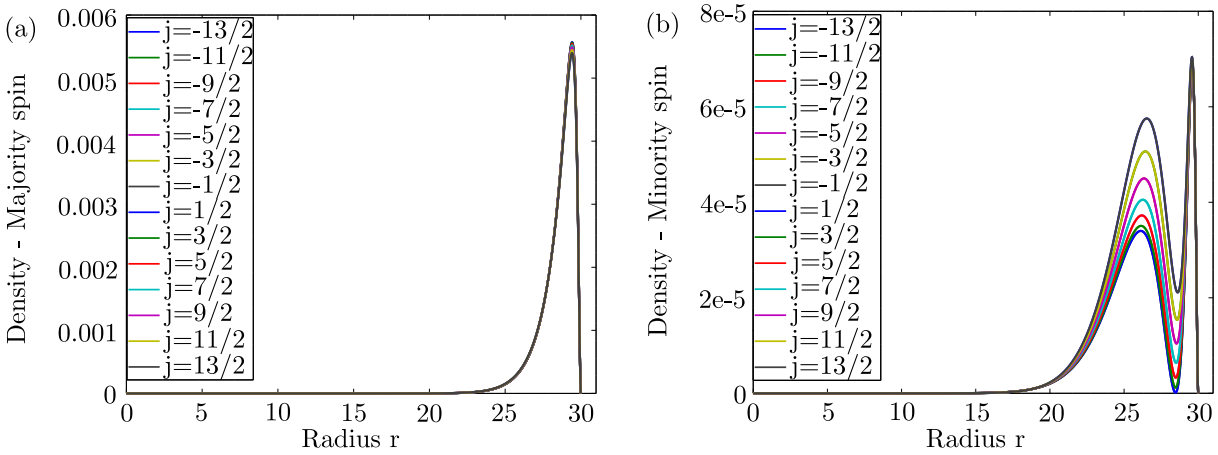

Figure 2.9: Spin-resolved probability densities of the clockwise-moving edge states as a function of r for a disk size $R = 30$. The parameters are $A = 5$, $B = -1$, $M = -2$ and $\Delta = 0.5$.

a second maximum situated more deeply in the TI. The effect of this second maximum on the total density is still weak (there is a very small broadening seen in Fig. 2.8). We will see in the next section that this behavior appears to be generic and is not due to any approximation or to the model.

We now have enough knowledge about the wave function and how to classify it completely. We know which wave function is clockwise- or counterclockwise-moving. We are thus able to compute the spin texture for different values of the total angular momentum j. An example can be seen in Fig. 2.10. As we can see, the structure is very similar to what we observed for the nanoribbon in Figs. 2.1, 2.2 and 2.3. We assume that the spin texture should follow a structure very close to Eq. (2.3): we have rotation invariance instead of translation invariance, therefore the momentum should be replaced by the total angular momentum. The edge is parametrized by the angular direction and the rotation

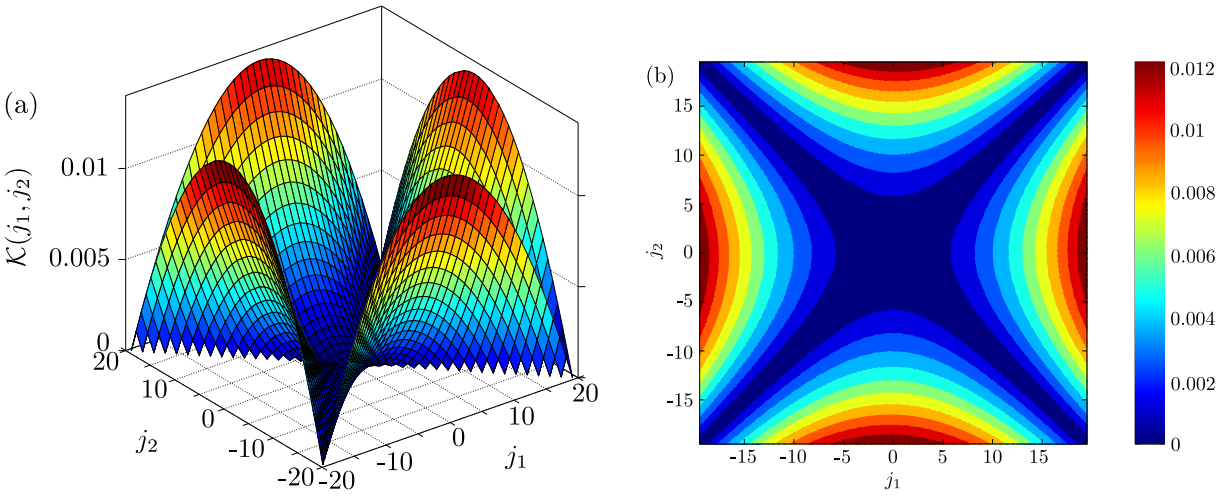

Figure 2.10: The spin texture of the continuous BHZ Hamiltonian including BIA for a disk of R=50. We set $A = 5$, $B = -1$, $M = -2$ and $\Delta = 0.5$. In panel (a), we have the three-dimensional plot and in panel (b), the corresponding contour plot.

of the spin axis is characterized by some parameter j_0^{-2}. By analogy, we can make the ansatz

$$\mathcal{K}(j_1, j_2) \;=\; \left| \int dr \psi^{\dagger}_{-,j_2}(r, \phi_0) \psi_{+,j_1}(r, \phi_0) \right| \approx \; j_0^{-2} \left| j_1^2 - j_2^2 \right|, \tag{2.22}$$

where $\psi_{+,j_1}(r, \phi_0)$ is the clockwise-moving eigenstate with a total angular momentum of j_1 and $\psi_{-,j_2}(r, \phi_0)$ is the counterclockwise-moving eigenstate with a total angular momentum of j_2. We perform the integral in the radial direction and without loss of generality, we set $\phi_0 = 0$. We observe that the diagonal terms of the spin texture vanish. If $j_1 = j_2$, the eigenstates are orthogonal by construction. If $j_1 = -j_2$, the eigenstates are TR-partners and should be orthogonal following Kramers' theorem.

Finally, we investigate the spin texture dependence on the BIA parameter, as we did for the nanoribbon. We notice that the parameter j_0^{-2} is dependent upon the size of the disk R. When the spin texture parameter is multiplied by R^2, the dependence disappears as can be seen in Fig. 2.11. Moreover, the engineering dimension of $j_0^{-2}R^2$ is similar to the one of k_0^{-2}. Nonetheless, the dependence on Δ seems to differ from the one for a nanoribbon as written in Eq. (2.4) (and shown with dashed lines in Fig. 2.11). It appears to scale as

$$j_0^{-2} R^2 \propto |\Delta|^{3/2}. \tag{2.23}$$

Even if the two systems are described by the same model, the geometry is rather different. More importantly, the nanoribbon is based on a tight-binding model regularized on a lattice, whereas the disk relies on a continuous model. All these points make it surprising that the two parameters agree so well.

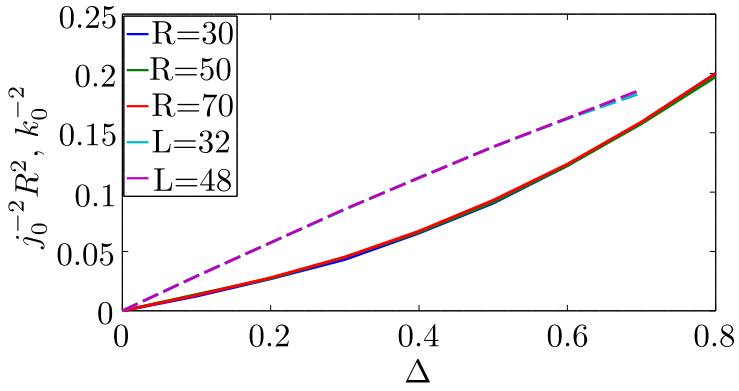

Figure 2.11: Dependence of $j_0^{-2}R^2$ on BIA Δ for disks of, R=30, R=50 and R=70. The dashed lines are the results of Fig. 2.4 to enables us to compare the two approaches. We had for the disks and for the nanoribbons $A = 5$, $B = -1$ and $M = -2$.

2.3 Extracting the spin texture in real space: discrete disks

Up to now, there was always a symmetry in the model to describe the spin texture: either translation symmetry or rotation symmetry. Nonetheless, it is possible to observe a non-trivial spin texture in a more general case, where we do not have any spatial symmetry. We study the tight-binding version of the KM Hamiltonian (1.10) for disks and flakes (rectangles). We encode the position of the sites during the construction of the Hamiltonian. We can exactly diagonalize it and directly get the energies and the eigenfunctions. An example of the energy spectrum and the density of states can be seen in Fig. 2.12. We observe an asymmetry in the density of states, due to Rashba SOC. In the bulk gap, the states are doubly degenerate and are nearly at equal spacing (a feature that we also observed in our continuum disks). At $E/t = \pm 1$, we observe some traces of a Van Hove singularity, that is usually seen in graphene [89].

If we select one energy level located inside the gap, the eigenfunction can be directly accessed and its density distribution over the lattice is expressed as

$$\rho_\sigma(i,j) = |\Psi_\sigma(i,j)|^2, \tag{2.24}$$

where σ stands for the spin-sector (the wave function at site (i,j) has always two components: one for spin-up and the other one for spin-down). One example of the wave function is shown in Fig. 2.13. The mixing is done by Rashba SOC and the minority spin density is again about two orders of magnitude smaller than the majority spin density. The states are indeed localized at the edge, but the minority spin density has the same behavior as in the continuum disk: it penetrates slightly deeper into the bulk.

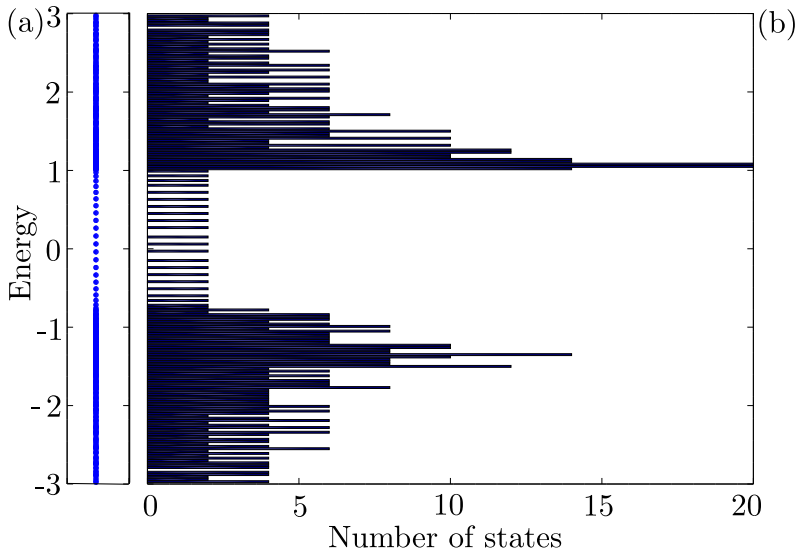

Figure 2.12: Energy levels (a) and density of states (b) for the KM model in the case of a rectangular flake of $N = 400$ sites (20×20 sites) for $t = 1$, $\lambda_{\mathrm{SO}} = 0.2$ and $\lambda_{\mathrm{R},1} = 0.1$.

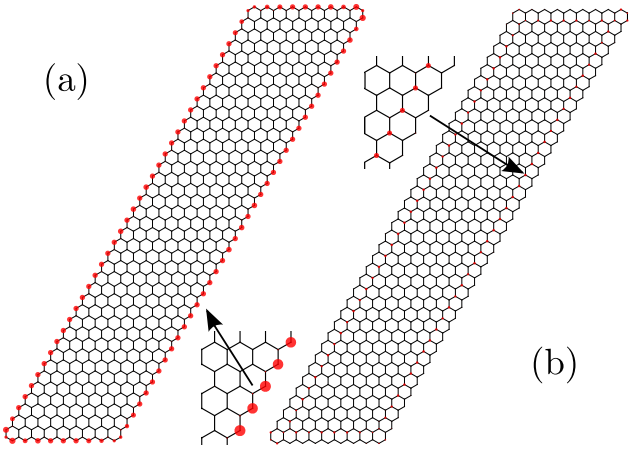

Figure 2.13: Example of a spin-resolved density distribution for the KM model in the case of a rectangular flake of $N = 800$ sites (20×40 sites) for $t = 1$, $\lambda_{\mathrm{SO}} = 0.2$ and $\lambda_{\mathrm{R},1} = 0.1$. The size of the dots is proportional to the density on the site. Panel (a) shows the density distribution for the majority spin whereas panel (b) shows the density distribution for the minority spin. Note that the minority spin was amplified by a factor of 20.

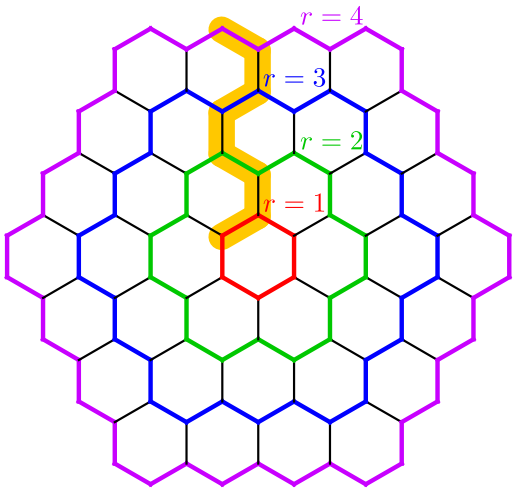

Figure 2.14: Example of a "disk" (having a hexagonal shape). We define the radius "r" with the different color. The set Λ of sites, which are highlighted in yellow, are those used to compute the spin texture as described in the text.

We will now consider the tight-binding disks as shown on Fig. 2.14. They are made in a hexagonal shape, as it is convenient to use the symmetries of the lattice. The rotational symmetry is lost, but we remain relatively close to a circle (we still have a 6-fold symmetry). The radius is defined such that all the sites on the same "rings" (defined by the color coding in Fig. 2.14) are considered at the same radius, as their distance from the center is approximately the same.

In the same way that we set $\phi_0 = 0$ for the continuum disks, we set here $\phi_0 = 0$ and only consider the sites on the highlighted yellow path in Fig. 2.14 to contribute to the radial density. In this manner, the outer sites do not have more weight compared to the inner sites, just because there are more outer sites than inner sites. Such radial density can also be spin-resolved and an example is shown on Fig. 2.15. The majority spin will be spin-up for clockwise-moving or spin-down for counterclockwise moving edge states, whereas the minority spin will be spin-down for clockwise-moving or spin-up for counterclockwise-moving edge states. Note that the lattice is finite and the maximal radius is relatively small. That is the reason why the wave functions appear less smooth than in Fig. 2.8. Nonetheless, their behavior is quite similar to what we observed previously. The majority spin is quite localized on the outermost sites and is the main component of the density. The minority spin penetrates deeper into the bulk, in perfect agreement with the continuum disks.

With the wave functions, we can compute the overlap. In analogy to the continuum disks and the nanoribbons, we compute the overlap along the highlighted path in Fig. 2.14 (the direction where $\phi_0 \simeq 0$). We cannot directly apply the formula (2.22): the total angular momentum cannot be defined in our tight-binding disks, because the continuous

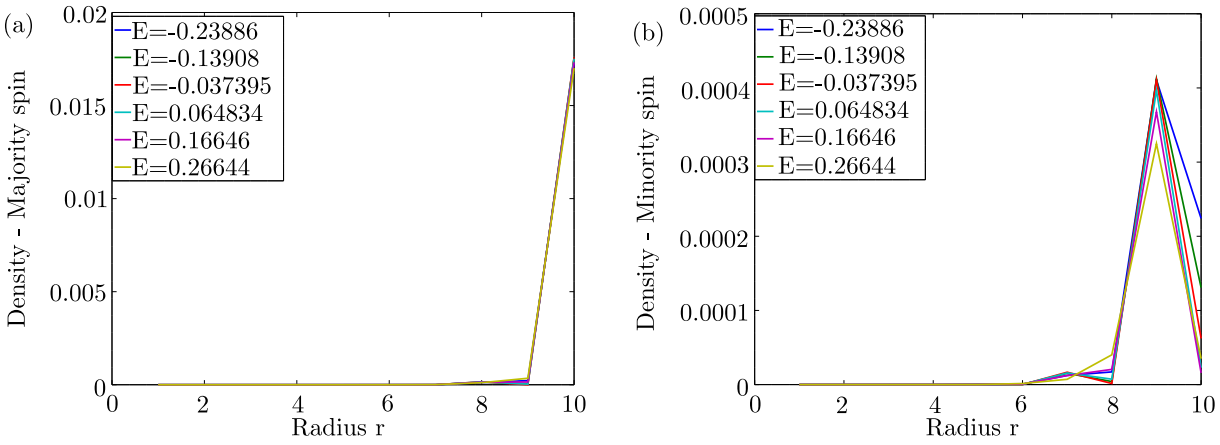

Figure 2.15: Representative examples of the spin-resolved densities with $t = 1$, $\lambda_{\mathrm{SO}} = 0.2$ and $\lambda_{\mathrm{R},1} = 0.1$. The densities are extracted along the path highlighted in Fig. 2.14. In panel (a), we have the majority spin and in panel (b), the minority spin.

rotational symmetry is not preserved. Moreover, if we consider the rectangular flakes presented above, we are even further from a rotationally symmetric arrangement. The characterizing quantity for the edge states is still the energy. As we observed in Fig. 2.12, the energy levels of the edge states are well defined, each being doubly degenerate with one edge state moving clockwise and the other one moving counterclockwise. Thus we can generalize our spin texture expression with labeling the edge states with their energy such that

$$\mathcal{K}(E_1, E_2) = \left| \sum_{(i,j)\in\Lambda} \psi^{\dagger}_{-,E_2}(i,j)\, \psi_{+,E_1}(i,j) \right| \approx \varepsilon_0^{-2} \left| E_1^2 - E_2^2 \right|, \tag{2.25}$$

where Λ is the highlighted path as shown in Fig. 2.14 and $\psi_{\pm,E_k}(i,j)$ is the wave function moving clockwise (counterclockwise) at the energy E_k at the site (i,j) on the lattice. Such a spin texture is plotted in Fig 2.16. We see the same similar features as in the previous setups: the diagonals vanish and the same hyperbolic shape is observed, agreeing with the low energy expression.

The spin texture is now characterized by ε_0^{-2}. It has the same engineering dimension as j_0^{-2}, therefore if we would like to compare with k_0^{-2} we also need to multiply all the extracted data by R^2. We can extract ε_0^{-2} for different disk sizes and different (Rashba) SOCs. The dependence should be the same as presented in Eq. (2.5), when it is properly rescaled. The results are shown on Fig. 2.17, where they agree well with the previous data from Fig. 2.5 (red dashed line). Note that the data of the nanoribbon had to be rescaled by a factor of 3, because the translation vector was considered as the unit vector, such that the Brillouin zone spanned from 0 to 2π. In the tight-binding disks, the distance

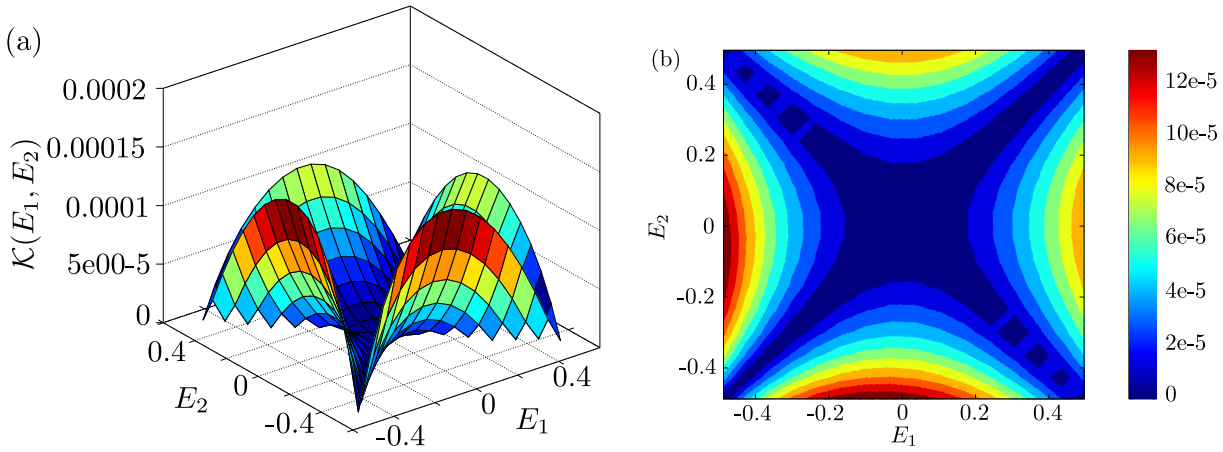

Figure 2.16: The spin texture of the tight-binding KM Hamiltonian for a disk of R=15 (1350 lattice sites). We set $t = 1$, $\lambda_{\mathrm{SO}} = 0.2$ and $\lambda_{\mathrm{R},1} = 0.05$. In panel (a), we have the three-dimensional plot and in panel (b), the corresponding contour plot.

between unit cells is $\sqrt{3}$. As the spin texture scales as the momentum squared at low energy, we need to multiply it by a factor of 3.

It is possible to argue that the shape of the hexagonal disks is still close to the one of the continuum disks, that it is just the discrete version. The correspondence is therefore not surprising. Nonetheless, we also extracted the spin texture on a rectangular flake as shown in Fig. 2.18. The highlighted path is again the sites where the spin structure was extracted and we observe no qualitative difference with the discrete disks. This enables us to conclude that the spin texture will be observed for any generic helical edge states with broken spin axis symmetry, independently of the considered model and of the chosen geometry.

2.3.1 Spectroscopic aspect of the spin texture

As the spin texture can be found in real space, independently of the considered geometry, this means that the spin texture can be extracted locally. We noticed that it was sufficient to sum all the contribution coming from the highlighted yellow path in Figs. 2.14 and 2.18. The notion of edge states suggests that the information should be located at the outermost sites, naïvely at the outermost site. The numerical evidence (see Figs. 2.13 and 2.15) indicates that indeed the outermost sites support most of the wave function. We could imagine that in an idealized case, the spin texture could be extracted on a single site using spectroscopic energy-resolved measurements. Thus, we need to understand how many sites from the edges are involved to be able to observe a non-trivial spin texture.

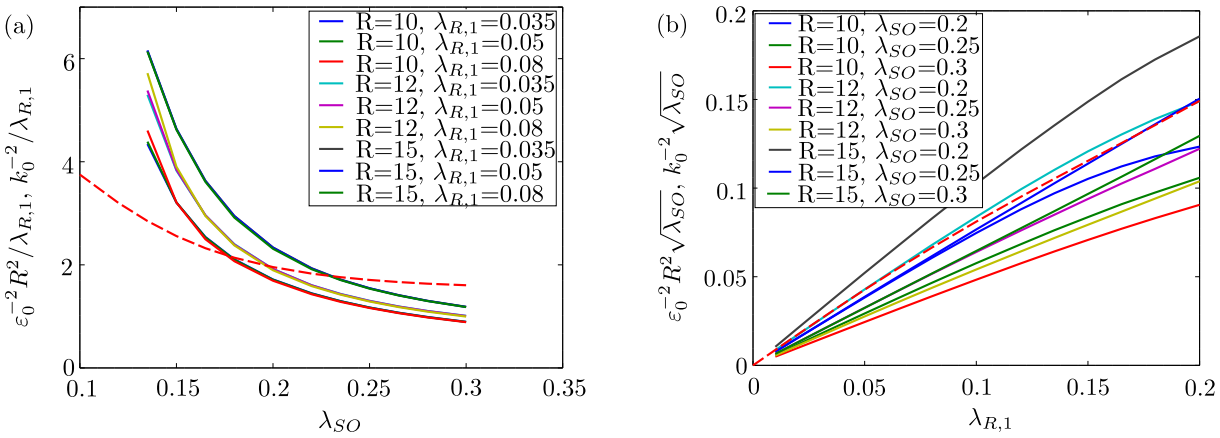

Figure 2.17: Dependence of $\varepsilon_0^{-2}R^2$ on the intrinsic SOC (a) and Rashba SOC (b) for disks of R=10 (600 lattice sites), R=12 (864 lattice sites) and R=15 (1350 lattice sites). We set $t = 1$. The dashed line in (a) and (b) corresponds to k_0^{-2} from Fig. 2.5, which has been rescaled by a factor 3 (see text for details).

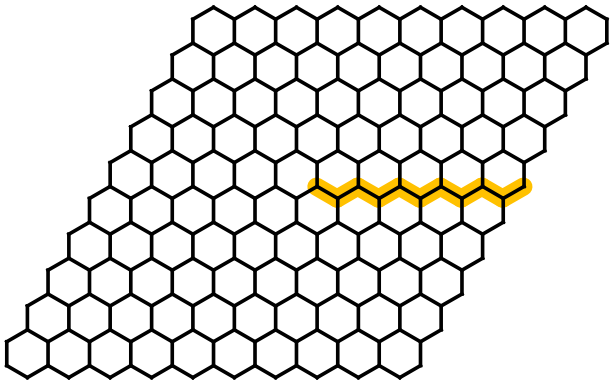

Figure 2.18: Example of a rectangular flake, the set of highlighted sites are those used to compute the spin texture as described in the text.

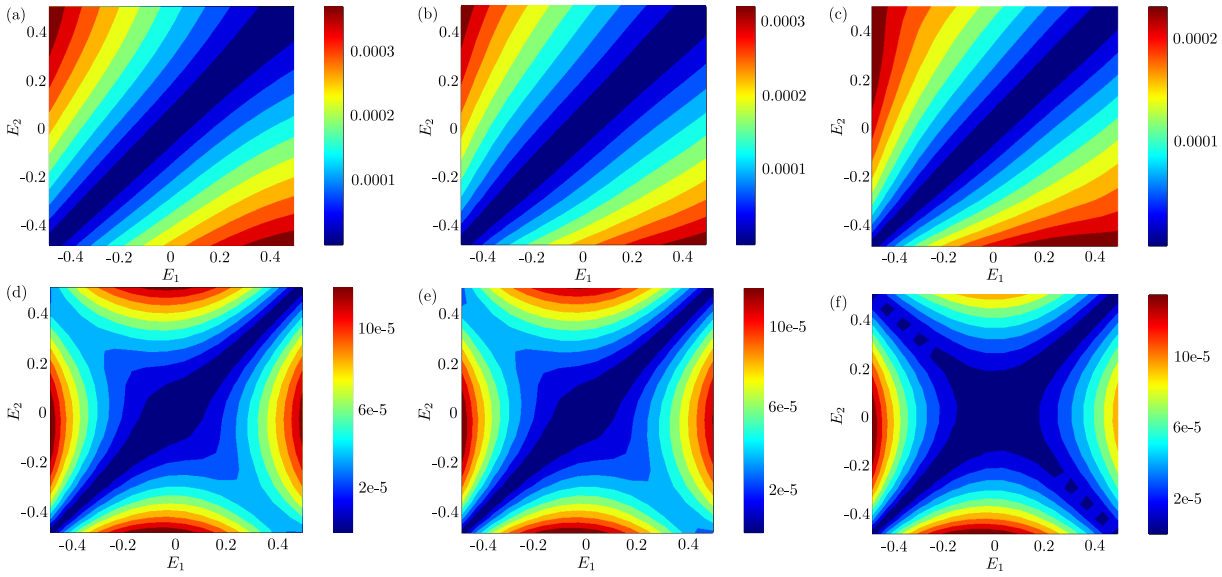

Figure 2.19: The partial spin texture of the tight-binding KM Hamiltonian for a disk of R=15 (1350 lattice sites). We only measure the overlap between the wave function for the $n = 1, \ldots, 6$ outermost sites. Panel (a) corresponds to the outermost site, (b) to the two outermost sites, (c) to the three outermost sites, (d) to the four outermost sites, (e) to the five outermost sites and (f) to the six outermost sites. We set $t = 1$, $\lambda_{\mathrm{SO}} = 0.2$ and $\lambda_{\mathrm{R},1} = 0.05$.

We slightly modify Eq. (2.25) in the following manner

$$\mathcal{K}(E_1, E_2) = \left| \sum_{(i,j)\in\Lambda_n} \psi^{\dagger}_{-,E_2}(i,j)\, \psi_{+,E_1}(i,j) \right|, \tag{2.26}$$

where Λ_n is the subset of the n outermost sites from the set Λ highlighted in yellow in Fig. 2.14. For example, Λ_1 corresponds to the outermost site of Λ, Λ_2 corresponds to the two outermost sites of Λ and so on. We can see the resulting depiction in Fig. 2.19, where we used a disk of size $R = 15$ (1350 lattice sites), which is relatively small. We observe that the non-trivial spin texture starts to emerge at $n = 4$ and is very close to the total one at $n = 6$ (i.e. the one plotted in Fig. 2.16). In comparison to experimental devices, the disk modeled here is several orders of magnitude smaller. We could imagine that in the experimental cases, it is just necessary to probe the two or three outermost sites to get the full spin texture. The spectroscopic measurements would be a direct way to probe the spin texture.

3 Transport and spectroscopic measurements of the spin texture

We managed in the previous chapter to characterize the non-trivial spin texture in several geometries, even when no spatial symmetry was present. We can now use this knowledge to extract some additional information in a transport setup and spectroscopically investigate the spin texture. Investigating transport properties is reasonable as most of the experimental setups for proving the existence of TIs and edge states are done within transport experiments as described in Sec. 1.4. To be able to do some transport and spectroscopic measurements, we studied a TI Hall bar with an embedded antidot (i.e. a hole in the middle of the Hall bar). We have then two quantum point contacts between the antidot and the border of the Hall bar, where the edge states can tunnel onto the antidot and propagate around the circumference of the hole.

This kind of setup has been investigated for a long time in the context of the IQHE [90–93]. Antidot systems were also studied in two-dimensional TIs to produce spin-polarized currents [94], nonlinear thermoelectric effects [95, 96], entanglement [97], or Kondo physics [98–100]. Quantum percolation was induced in TI nanorribons and Hall bars by the bound states of multiple antidots [101]. As antidots can be small, the confinement of the edge states is then important and the charging energy induced by Coulomb interaction might not be negligible. From a technological point of view, antidots can be engineered by lithographically etching Hall bars. If the TI is made of an InAs/GaSb heterostructure, the antidot can be created by locally gating the central region to the trivial regime. Some of the results presented in this chapter were already published in Ref. [80].

3.1 Transport model

The model we consider is sketched in Fig. 3.1. We have three pairs of helical edge states: one is located around the antidot (d), two pairs at the upper (U) and at the lower

(L) edges of the Hall bar. The tunneling regions between the outer edges and the antidot appear when the wave functions of the edge states overlap. The total Hamiltonian can written as

$$\mathcal{H} = \mathcal{H}_U + \mathcal{H}_L + \mathcal{H}_d + \mathcal{H}_{dU} + \mathcal{H}_{dL}, \tag{3.1}$$

where $\mathcal{H}_{U(L)}$ is the Dirac Hamiltonian describing the upper (lower) edge states, $\mathcal{H}_d$ is the Hamiltonian representing the edge channels of the antidot, and $\mathcal{H}_{dU(dL)}$ is the tunneling Hamiltonian between the upper (lower) edge and the antidot. The Hamiltonian of the upper and lower edges given by

$$\mathcal{H}_s = -isv_F \sum_{\alpha=\pm} \alpha \int_{-l/2}^{l/2} dx\, \Psi^\dagger_{s\alpha}(x)\partial_x \Psi_{s\alpha}(x), \tag{3.2}$$

where $s = U, L \equiv +, -$ and $\alpha = \pm$ is the chirality of the edge state. v_F is the Fermi velocity and l is the length of the Hall bar. We will mostly consider $l \to \infty$, therefore the edge states on the outer edges will be considered as continuous. This is not the case for the antidot: the energy levels are discrete and are characterized by the radius R of the antidot, leading to an energy spacing of $\Delta E \approx v_F/R$. If the axial spin symmetry is not broken, the chiral direction will also correspond to the spin axis projection: the spin-up states will propagate along the upper (lower) edge to the right (left) and vice versa for the spin-down states. However, we are not interested in this limit, but in the more general scheme of generic helical edge states. To do so, we need to go to momentum space, where it is clear, as shown in Secs. 1.5 and 2.1, how to relate the chiral and the spin basis. The operators in momentum space are written for the chiral basis as $c_{s\alpha k} = \int dx e^{-ikx}\Psi_{s\alpha}(x)/\sqrt{l}$, where $\alpha = \pm$ and for the spin basis as $c_{s\sigma k} = \int dx e^{-ikx}\Psi_{s\sigma}(x)/\sqrt{l}$ where $\sigma = \uparrow, \downarrow$. Using the form of B_k as given in Eq. (1.32), we are able to relate the two bases. Note that the rotation on the two edges are not necessarily identical and are characterized by the parameters θ_{Uk} and θ_{Lk}.

The antidot Hamiltonian is very similar to those of the outer edges

$$\mathcal{H}_d = -iv_F \sum_{\alpha=\pm} \alpha \int_0^{2\pi R} dr\, \Psi^\dagger_{d\alpha}(r)\partial_r \Psi_{d\alpha}(r) + E(n). \tag{3.3}$$

As we have to consider the confinement of the electron on the antidot through the charging energy, we have an additional term

$$E(n) = \frac{E_c}{2}\left(n - \frac{eV_g}{E_c}\right)^2, \tag{3.4}$$

where V_g is the gate voltage, E_c is the Coulomb energy and $n = \sum_\alpha \int_0^{2\pi R} \Psi^\dagger_{d\alpha}(r)\Psi_{d\alpha}(r)$

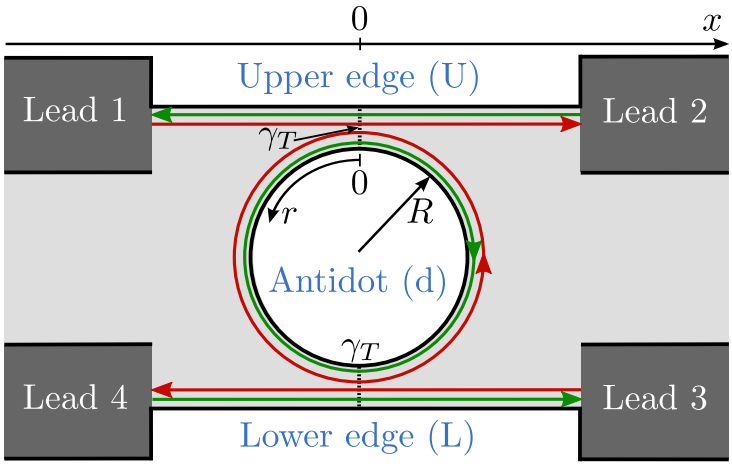

Figure 3.1: Sketch of the model. The light gray area is the QSH bar, where in its middle an antidot with a radius R is embedded. The leads are symbolized by the dark gray areas. The tunnelings point contacts (black dashed lines) are located at $x = 0$, $r = 0$ and $x = 0$, $r = \pi R$. The chirality of the edge states is either " + " (red color) or " − " (green color).

is the number operator on the antidot. The charging energy varies with the number of electrons on the antidot as well as with the gate voltage applied on it. The wave functions are not eigenstates of the spin operator, but they remain chiral, propagating clockwise/counterclockwise around the antidot. As we saw in Sec. 2.2, we can replace the momentum by the angular momentum to describe the spin texture. By analogy, we can relate the chiral basis $d_{\alpha j} = \int dr e^{-ijr/R} \Psi^\dagger_{d\alpha}(r)/\sqrt{2\pi R}$, with $\alpha = \pm$ to the spin basis $d_{\sigma j} = \int dr e^{-ijr/R} \Psi^\dagger_{d\sigma}(r)/\sqrt{2\pi R}$, with $\sigma = \uparrow, \downarrow$ using the following rotation matrix

$$\tilde{B}_j = \begin{pmatrix} \cos(\theta_j) & -\sin(\theta_j) \\ \sin(\theta_j) & \cos(\theta_j) \end{pmatrix}. \tag{3.5}$$

The tunneling processes occur for the upper edge near $x = 0$ and $r = 0 \equiv r_U$ and for the lower edge $x = 0$ and $r = \pi R \equiv r_L$ as shown in Fig. 3.1. We consider the most general form of the tunneling Hamiltonian containing spin-preserving and spin-flipping terms [102]

$$\mathcal{H}_{ds} = \sum_{\sigma\sigma'} \int dx dr \left[\Psi^\dagger_{s\sigma}(x) \gamma^s_{\sigma\sigma'}(x, r) \Psi_{d\sigma'}(r_s + sr) + \text{h.c.} \right], \tag{3.6}$$

where $s = U, L \equiv +, -$ and $\sigma, \sigma' = \{\uparrow, \downarrow\}$. We can notice that the Hall bar has a reflection symmetry around the x-axis: $(x, y) \to (x, -y)$ and $(p_x, p_y) \to (p_x, -p_y)$. Since spin has the same structure as the angular momentum, such a reflection symmetry leads to the transformation of $\sigma_z \to -\sigma_z$. This means that the wave functions must transform as $\Psi_{U\sigma}(x) \to \Psi_{L\bar{\sigma}}(x)$ and $\Psi_{d\sigma}(r) \to \Psi_{d\bar{\sigma}}(\pi R - r)$. Note that $\mathcal{H}_{dU} + \mathcal{H}_{dL}$ remains invariant under this symmetry, which leads to the following equivalences $\gamma^U_{\sigma\sigma'} = \gamma^L_{\bar{\sigma}\bar{\sigma}'}$. It enables us

to eliminate the tunneling coefficient from the antidot to the lower edge and we define $\gamma_{\sigma\sigma'} = \gamma^U_{\sigma\sigma'}$. Moreover, the tunneling Hamiltonian is assumed to preserve TR-symmetry, this symmetry acts locally in space on the edge states $\Psi_{s\sigma}(x) \to \sigma\Psi_{s\bar{\sigma}}(x)$, where here $s = \{U, L, d\}$ and $\sigma = \{\uparrow, \downarrow\} = +, -$. In addition to the behavior of the wave function, the tunneling amplitudes also respect TR-symmetry: $\gamma_{\uparrow\uparrow} = \gamma_{\downarrow\downarrow}$ and $\gamma_{\uparrow\downarrow} = -\gamma_{\downarrow\uparrow}$, such that we define only the spin-preserving amplitude $\gamma_{\mathrm{sp}} \equiv \gamma_{\uparrow\uparrow}$ and the spin-flipping amplitude $\gamma_{\mathrm{sf}} \equiv \gamma_{\uparrow\downarrow}$ [103, 104]. We can rewrite the Hamiltonian now as

$$\mathcal{H}_{ds} = \sum_{\sigma} \int dx dr \big[\Psi^\dagger_{s\sigma}(x)\gamma_{\mathrm{sc}}(x,r)\Psi_{d\sigma}(r_s + sr) + s\sigma\Psi^\dagger_{s\sigma}(x)\gamma_{\mathrm{sf}}(x,r)\Psi_{d\bar{\sigma}}(r_s + sr) + \mathrm{h.c.}\big]. \tag{3.7}$$

Note that the symmetry used here is reflection symmetry and not inversion symmetry $(x, y) \to (-x, -y)$. We will see later that inversion symmetry is not preserved in the KM model, Eq. (1.10), due to the Rashba SOC. Rashba SOC indeed appears at the interface due to the lack of inversion symmetry, see Sec. 1.3.

The tunneling Hamiltonian is currently expressed in terms of spin eigenstates. However, we would like to express it in the chiral eigenstate basis. We Fourier transform our tunneling Hamiltonian into momentum and angular momentum space, and use the rotation matrices described in Eqs. (1.32) and (3.5). It becomes

$$\begin{aligned}\mathcal{H}_{ds} = \frac{1}{\sqrt{2\pi Rl}} \sum_{\sigma} \sum_{k,j} \sum_{\alpha\alpha'} \big[&e^{ijr_s/R}\tilde{\gamma}_{\mathrm{sp}}(k, sj)(B^\dagger_{s,k})^{\alpha\sigma}\tilde{B}^{\sigma\alpha'}_j c^\dagger_{s\alpha k} d_{\alpha' j} \\ &+ e^{ijr_s/R}\tilde{\gamma}_{\mathrm{sf}}(k, sj)(B^\dagger_{s,k})^{\alpha\sigma}\tilde{B}^{\bar{\sigma}\alpha'}_j s\sigma c^\dagger_{s\alpha k} d_{\alpha' j} + \mathrm{h.c.}\big].\end{aligned} \tag{3.8}$$

To simplify the above expression, we assume that the Fourier transformed tunneling amplitudes $\tilde{\gamma}_{\{\mathrm{sp,sf}\}}(k, j)$ are slow-varying functions of k and j. We can justify this assumption when the tunneling region can be considered to be small compared to the Fermi wavelength. This is the case when the temperature and the bias voltage are small compared to $v_F k_{0\{U,L\}}$. We are then able to replace the (angular) momentum dependent tunnelings as well as the (angular) momentum rotation matrices by their values at the Fermi energy such that

$$\begin{aligned}\gamma_T \cos(\theta_T) &= \tilde{\gamma}_{\mathrm{sp}}(k_F, j_F) \\ \gamma_T \sin(\theta_T) &= \tilde{\gamma}_{\mathrm{sf}}(k_F, j_F) \\ \tilde{B} &= \tilde{B}_{j_F} \\ B_s &= B_{s,k_F} \quad \text{for } s \in \{U, L\},\end{aligned} \tag{3.9}$$

where $k_F = \mu/v_F$ and $j_F = \mu R/v_F$ are evaluated at the chemical potential μ. The ratio between the tunneling amplitudes for spin-preserving and spin-flipping tunnelings

is defined as θ_T, such that $\theta_T = \tan^{-1}(\tilde{\gamma}_{\rm sp}(k_F, j_F)/\tilde{\gamma}_{\rm sf}(k_F, j_F))$. If we Fourier transform back to real space, we get

$$\begin{aligned} \mathcal{H}_{ds} &= \gamma_T \sum_{\alpha\alpha'} \Psi^\dagger_{s\alpha}(0)\phi_{s\alpha\alpha'}\Psi_{d\alpha'}(r_s) + \text{h.c.}, \\ \phi_{s\alpha\alpha'} &= \sum_\sigma (B^\dagger_s)^{\alpha\sigma}\left(\cos\theta_T \tilde{B}^{\sigma\alpha'} + s\sigma \sin\theta_T \tilde{B}^{\bar{\sigma}\alpha'}\right). \end{aligned} \tag{3.10}$$

The Hamiltonian $\mathcal{H}$ is now fully described in terms of chiral eigenstates. We can proceed to evaluate the transport properties of this Hamiltonian.

3.2 Probing the spin texture with a non-interacting antidot

We first investigate the transport properties without considering the interaction between the electrons using the scattering matrix formalism [105]. To evaluate the scattering matrix, we compute the Heisenberg equations of motion $i\partial_t \Psi_{s\alpha} = [\Psi_{s\alpha}, \mathcal{H}]$ and $i\partial_t \Psi_{\mathrm{d}\alpha} = [\Psi_{\mathrm{d}\alpha}, \mathcal{H}]$, where $\mathcal{H}$ is the full Hamiltonian written in Eq. (3.1). The wave functions are plane-waves

$$\begin{aligned} \Psi_{U\pm} &= \frac{e^{-i\mu t}}{\sqrt{2\pi v_F}} \begin{cases} a_1(b_2)e^{\pm ik_F x} & x < 0 \\ b_1(a_2)e^{\pm ik_F x} & x > 0 \end{cases}, \\ \Psi_{L\pm} &= \frac{e^{-i\mu t}}{\sqrt{2\pi v_F}} \begin{cases} a_4(b_3)e^{\mp ik_F x} & x < 0 \\ b_4(a_3)e^{\mp ik_F x} & x > 0 \end{cases}, \end{aligned} \tag{3.11}$$

for the states emerging from the contact i (with amplitude a_i) and entering the contact j (with amplitude b_j), $i, j = 1, ..., 4$ as written in Fig. 3.1. The aim of this computation is to find the scattering matrix S_{ij} that relates the incoming to the outgoing states

$$b_i = \sum_j S_{ij} a_j. \tag{3.12}$$

The details of the computation for obtaining the scattering matrix can be found in appendix A. We consider first when the chemical potential in the leads μ corresponds to one of the energy levels of the antidot. From these results, we were able to generalize it, when the antidot energy level does not coincide with chemical potential in the leads. The full scattering matrix depends then on the chemical potential μ in the leads as well as on difference in energy with the closest energy level in the antidot. It can therefore be

expressed as

$$S = \frac{1}{(1+\Gamma^2)\sin\phi + 2i\Gamma\cos\phi} \times \begin{pmatrix} 0 & (1-\Gamma^2)\sin\phi & 2i\Gamma\sin\Theta & -2i\Gamma\cos\Theta \\ (1-\Gamma^2)\sin\phi & 0 & -2i\Gamma\cos\Theta & -2i\Gamma\sin\Theta \\ -2i\Gamma\sin\Theta & -2i\Gamma\cos\Theta & 0 & (1-\Gamma^2)\sin\phi \\ -2i\Gamma\cos\Theta & 2i\Gamma\sin\Theta & (1-\Gamma^2)\sin\phi & 0 \end{pmatrix}, \tag{3.13}$$

where the dimensionless tunneling coefficient is defined as $\Gamma = |\gamma_T|^2/(4v_F^2)$. The chemical potential sets the value of the phase in the scattering matrix $\phi = \pi R\mu/v_F$ and we define the parameter $\Theta = \theta_{Uk_F} - \theta_{Lk_F} + 2\theta_T$. Landauer-Büttiker formalism [106–110] enables us to evaluate from Eq. (3.13) the current at the ith contact

$$I_i = \frac{G_0}{e}\sum_j \int_{\mu+eV_j}^{\mu+eV_i} dE\, T_{ij}(E), \tag{3.14}$$

where the conductance quantum is $G_0 = e^2/(2\pi)$. The transmission elements are given by $T_{ij} = |S_{ij}|^2$ and $\{V_j\}$ are the bias potentials applied at the four contacts. Note that the spin texture of the antidot does not influence the transport calculations, but that transport measurements can be affected by the spin texture of the outer edges through Θ. This means that if we can separately tune the spin textures on the lower and upper edges, for example using an electric field gradient, current measurements can resolve them, even without interactions. This is analogous to what was described for a tunnel junction between two edges [81]. In the case of a homogeneous spin texture over the whole Hall bar, i.e. $\theta_{Uk_F} = \theta_{Lk_F}$, we have $\Theta = 2\theta_T$. Therefore, the ratio between spin-preserving and spin-flipping tunneling is the only determining quantity in the transport calculations. We assume that we are at resonance, when the chemical potential corresponds to one energy level of the antidot $\mu = v_F j/R$. In this case, the phase factor becomes $\phi = \pi j$ and the electrons are fully transmitted across the antidot to the leads on the opposite edge. If we are away from one of the eigenenergies of the antidot, we get a Lorentzian for the transmission coefficient. This results in what we expect for transport measurements across a quantum (anti)dot [111].

These analytical results are confirmed numerically using the python-based package KWANT [112], which is designed to perform quantum transport calculations using tight-binding models. To investigate the spin texture, we studied mainly the KM model, such as written in Eq. (1.10), but also the BHZ model with BIA, as in Eq. (1.27). We will only consider numerically the homogeneous case when $\theta_{Uk_F} = \theta_{Lk_F}$.

Due to Rashba SOC, inversion symmetry $(x, y) \to (-x, -y)$ is not preserved in the

KM model [113]. Spin is a pseudovector, so it is unaffected by inversion. However, the sublattices (a & b) are exchanged, but the phase ν_{ij} remains the same. Therefore, inversion symmetry leaves the kinetic and the intrinsic SOC terms invariant. Rashba SOC gets a minus sign under inversion, which ensures that inversion symmetry is not a symmetry of the full Hamiltonian. On the other hand, reflection symmetry around the x axis $(x, y) \to (x, -y)$ is preserved by the full Hamiltonian. The y and z components of the spin are changing signs and the sublattices are also exchanged. Therefore, the kinetic part is invariant. For the intrinsic SOC part, the phase ν_{ij} changes sign, which implies preservation of the reflection symmetry. For the Rashba SOC part, the y component of the lattice vectors switches sign, whereas the x component does not switch. Taking into account the changes of sign for the spin, we observe that the whole Hamiltonian is invariant. It confirms that the symmetry to consider for the Hall bar is the reflection symmetry.

Numerically, we are able to represent the finite-size lattice of the Hall bar connected to the four leads as shown in Fig. 3.2. We have chosen the antidot to be hexagonal, in order to avoid dangling bonds. The numerical simulation enables us to have access to the full scattering matrix and we can focus, without loss of generality, on electrons originating from lead 1. As the lattice has a finite size, there are additional pairs of edge states along the vertical edges. These channels are fully ballistic as they are further away from the antidot, and so are not able to tunnel to it, making them easy to identify. The spin-resolved density is shown in Fig. 3.2 where the weight of each spin sector is characterized by the size of the points and we are investigating their propagation around the antidot and along the edges for small Rashba SOC ($\theta_{sk_F} \ll 1$).

Spin flips at the tunneling contacts are enabled by Rashba SOC only. Its amplitude can be quantified by the taken values of the transmission probabilities as we will explain below. Without loss of generality as the four leads are equivalent, we can compute the transmission probability from lead 1 to lead i T_{i1} evaluated at a given potential μ (except T_{11}, which is always 0, as backscattering is forbidden). The different transmission probabilities are given in Fig. 3.3 for different strengths of the Rasbha SOC. We find in Fig. 3.3(a) that the transmission T_{21} disappears each time the chemical potential corresponds to an energy level of the antidot. This agrees with the results obtained analytically in Eqs. (3.13), (A.7) and (A.11) (i.e. when $\phi = \pi j$). As T_{11} is always zero, the electrons are fully transmitted across the antidot to the opposite sites. If we focus now on the leads on the opposite side, we can first conclude that T_{31} is only present when Rashba SOC is turned on (i.e. spin flips are now enabled) as shown in Fig. 3.3(b). Fig 3.3(c) shows that in the absence of Rashba SOC, the electrons are only transmitted to lead 4, when the chemical potential reaches one of the energy levels of the antidot. This is in perfect

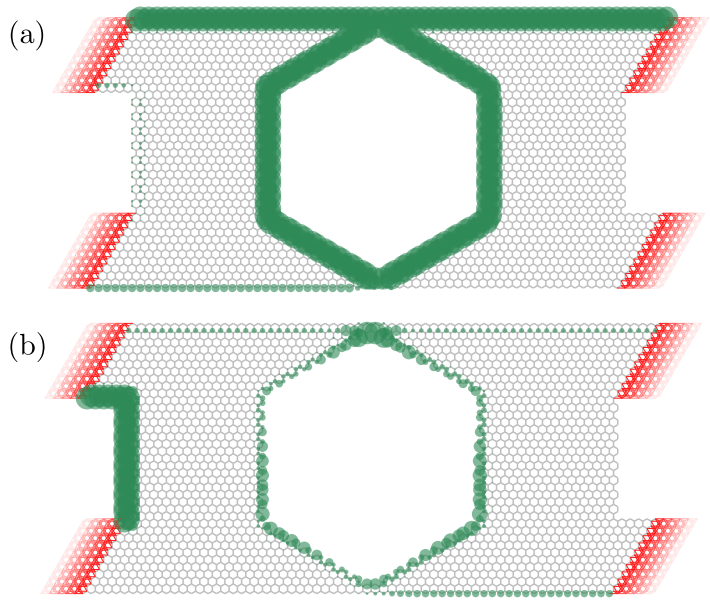

Figure 3.2: Representative example of the spin-resolved densities close to resonance, when they originate from lead 1. On panel (a), we have the propagation for the spin-up sector of the density and on panel (b), we have the propagation for the spin-down sector of the density. The lattice is 60 unit cells long and 34 unit cells wide and the leads are 10 unit cells wide. We used the following parameters $a = 1$, $t = 1$, $\lambda_{\mathrm{SO}} = 0.2$, $\lambda_{\mathrm{R},1} = 0.1$ and $\mu = 0.157$.

agreement from our analytical results. Finally, we can note that the transmission probability is symmetric with respect to the value of the chemical potential, i.e. $T_{ij}(\mu) = T_{ij}(-\mu)$, when there is no Rashba SOC. Once Rashba SOC is turned on, we lose this symmetry as we can see in the different panels of Fig. 3.3. Moreover, we already noticed the breaking of the particle-hole symmetry due to Rashba SOC in Chap. 2.

We observe that the shape of the peaks in the transmission probabilities are following a Lorentzian near resonance. This was also predicted analytically, but their widths are energy-dependent. With the height of the peaks for the extracted $T_{31}(\mu)$ or $T_{41}(\mu)$, $\theta_T(\mu)$ can be evaluated numerically, as shown in Fig. 3.4(a). $\gamma_T(\mu)$ can be similarly evaluated using the width of the peaks for $T_{31}(\mu)$ or $T_{41}(\mu)$. The transmission probabilities in Fig. 3.3 show that that $\theta_T(\mu)$ and $\gamma_T(\mu)$ evolve slowly enough with respect to the antidot energy level spacing for considering them constant at each peak. Moreover, the peaks follow well the Lorentzian shape. Therefore, our numerical results enable us to estimate $\theta_T(\mu)$ and $\gamma_T(\mu)$ as well as their dependence on the model parameters. The only unknown is the Fermi velocity, which can be calculated via the band structure obtained in the semi-infinite leads. The numerical simulations allow us to give estimates of all the variables entering into the analytical model.

As stated before, the calculations were also performed for the BHZ model with BIA,

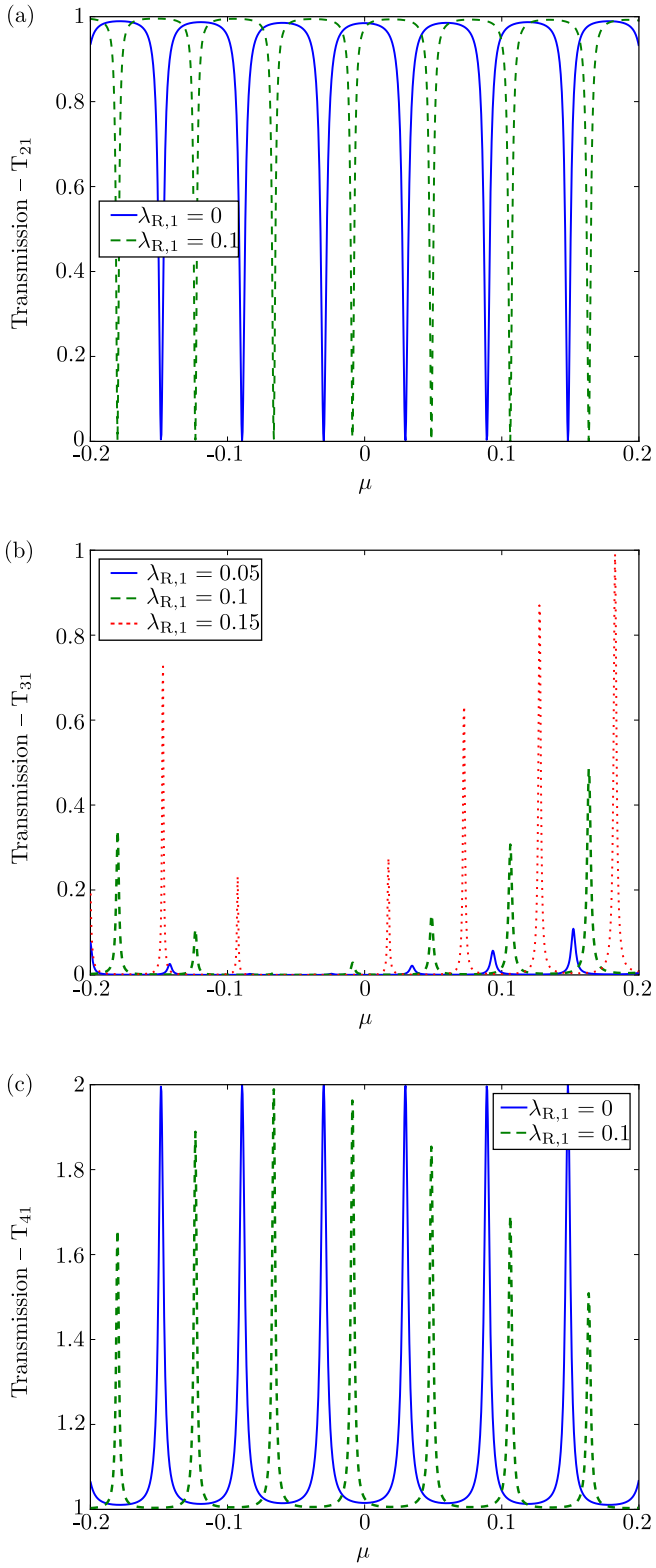

Figure 3.3: Transmission probabilites T_{i1} computed from lead 1 to lead i as a function of the chemical potential and for different values of the Rashba SOC. We have the transmission to lead 2 in panel (a), lead 3 in panel (b), and lead 4 in panel (c). We used the following parameters $a = 1$, $t = 1$ and $\lambda_{\mathrm{SO}} = 0.2$.

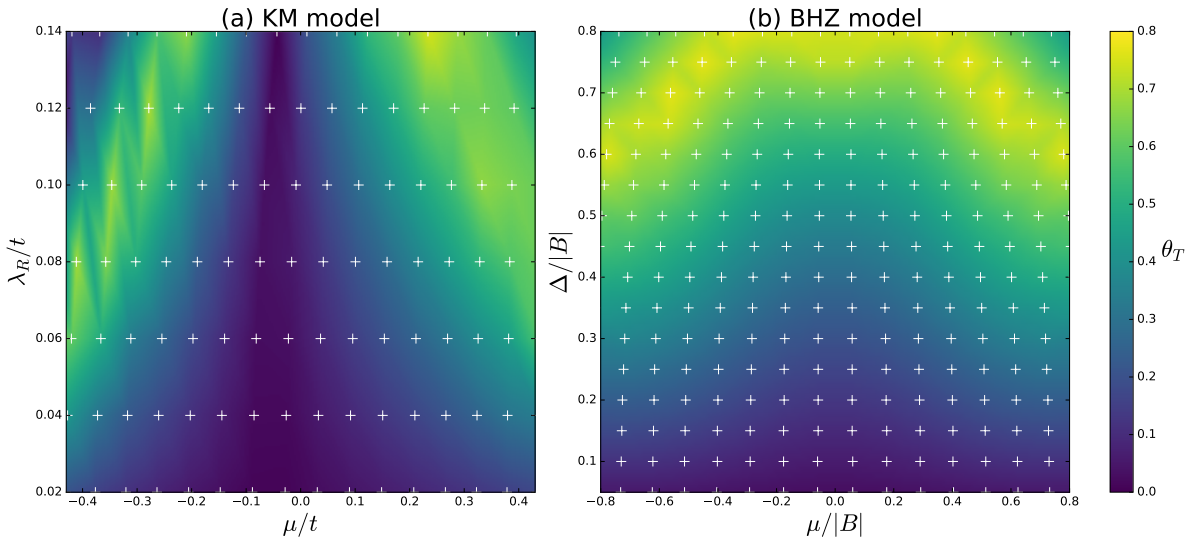

Figure 3.4: Evaluation of $\theta_T(\mu)$ when the chemical potential corresponds to one of the resonance energies. We evaluated it for the KM model (a) and for the BHZ model with BIA (b). The white crosses are located at the resonances, where θ_T is extracted. We used the following parameters $a = 1$, $t = 1$ and $\lambda_{\mathrm{SO}} = 0.2$ for the KM model (a) and $a = 1$, $A = 3$, $B = -1$, $M = -2$ and $C = D = 0$ for the BHZ model (b).

Eq. (1.27). The effect of BIA is quite similar to that of Rashba SOC in the KM model. There is no major qualitative difference between the two models as one would expect. The main difference comes from the fact that the BHZ model when BIA is also included remains particle-hole symmetric as shown in Fig. 3.4(b).

We are also able to compute the (non)local resistance. Using Eq. (3.14) in the linear regime (such that T_{ij} is considered as constant in the bias window), we can compare the analytic outcomes with our numerical simulations. Note that we consider the additional purely ballistic channels along the edges from lead 1 to lead 4 (and vice versa) and from lead 2 to lead 3 (and vice versa). These ballistic channels appear on Fig. 3.2. We find the following transmission matrix

$$T = \begin{pmatrix} 0 & 0 & 0 & 1 \\ 0 & 0 & 1 & 0 \\ 0 & 1 & 0 & 0 \\ 1 & 0 & 0 & 0 \end{pmatrix} + \frac{1}{(1-\Gamma^2)^2 \sin^2\phi + 4\Gamma^2} \begin{pmatrix} 0 & (1-\Gamma^2)^2 \sin^2\phi & 4\Gamma^2 \sin^2\Theta & 4\Gamma^2 \cos^2\Theta \\ (1-\Gamma^2)^2 \sin^2\phi & 0 & 4\Gamma^2 \cos^2\Theta & 4\Gamma^2 \sin^2\Theta \\ 4\Gamma^2 \sin^2\Theta & 4\Gamma^2 \cos^2\Theta & 0 & (1-\Gamma^2)^2 \sin^2\phi \\ 4\Gamma^2 \cos^2\Theta & 4\Gamma^2 \sin^2\Theta & (1-\Gamma^2)^2 \sin^2\phi & 0 \end{pmatrix}. \tag{3.15}$$

To compute the (non)local resistance [105], we need to inverse the matrix relating the

current and the voltage.

$$\begin{pmatrix} I_1 \\ I_2 \\ I_3 \\ I_4 \end{pmatrix} = G_0 \begin{pmatrix} 2 & 0 & 0 & -1 \\ 0 & 2 & -1 & 0 \\ 0 & -1 & 2 & 0 \\ -1 & 0 & 0 & 2 \end{pmatrix} \begin{pmatrix} V_1 \\ V_2 \\ V_3 \\ V_4 \end{pmatrix} - \frac{G_0}{(1-\Gamma^2)^2 \sin^2\phi + 4\Gamma^2} \begin{pmatrix} 0 & (1-\Gamma^2)^2 \sin^2\phi & 4\Gamma^2 \sin^2\Theta & 4\Gamma^2 \cos^2\Theta \\ (1-\Gamma^2)^2 \sin^2\phi & 0 & 4\Gamma^2 \cos^2\Theta & 4\Gamma^2 \sin^2\Theta \\ 4\Gamma^2 \sin^2\Theta & 4\Gamma^2 \cos^2\Theta & 0 & (1-\Gamma^2)^2 \sin^2\phi \\ 4\Gamma^2 \cos^2\Theta & 4\Gamma^2 \sin^2\Theta & (1-\Gamma^2)^2 \sin^2\phi & 0 \end{pmatrix} \begin{pmatrix} V_1 \\ V_2 \\ V_3 \\ V_4 \end{pmatrix} \tag{3.16}$$

This matrix is singular (i.e. the determinant is zero), but we can eliminate one voltage by setting it to zero, as the current is determined by the difference of voltages. One current can be eliminated using Kirchhoff's current law. This enables us to eliminate one row and one column of the conductance matrix presented in Eq. (3.14), creating a new matrix which is invertible.

$$\begin{pmatrix} I_1 \\ I_2 \\ I_3 \end{pmatrix} = G_0 \begin{pmatrix} 2 & -\frac{\left(1-\Gamma^2\right)^2 \sin^2\phi}{(1-\Gamma^2)^2 \sin^2\phi + 4\Gamma^2} & -\frac{4\Gamma^2 \sin^2\Theta}{(1-\Gamma^2)^2 \sin^2\phi + 4\Gamma^2} \\ -\frac{\left(1-\Gamma^2\right)^2 \sin^2\phi}{(1-\Gamma^2)^2 \sin^2\phi + 4\Gamma^2} & 2 & -1 - \frac{4\Gamma^2 \cos^2\Theta}{(1-\Gamma^2)^2 \sin^2\phi + 4\Gamma^2} \\ -\frac{4\Gamma^2 \sin^2\Theta}{(1-\Gamma^2)^2 \sin^2\phi + 4\Gamma^2} & -1 - \frac{4\Gamma^2 \cos^2\Theta}{(1-\Gamma^2)^2 \sin^2\phi + 4\Gamma^2} & 2 \end{pmatrix} \begin{pmatrix} V_1 \\ V_2 \\ V_3 \end{pmatrix} \tag{3.17}$$

The resistance matrix R is then obtained by inverting the matrix above. For example, if we would like to compute the resistance when the current is flowing from lead 1 to lead 4 and the voltage is biased between the same leads we have

$$R_{14,14} = \left.\frac{V_1 - V_4}{I_1}\right|_{I_4=-I_1, I_2=I_3} \tag{3.18}$$

such that at resonance ($\phi = 0$) and when the Hall bar is homogeneous ($\theta_{Uk} = \theta_{Lk}$), we get

$$R_{14,14} = G_0^{-1} \left[\frac{1}{\cos(4\theta_T) + 3} + \frac{1}{4}\right]. \tag{3.19}$$

The numerical outcome is shown on Fig. 3.5. We can distinguish the two limiting cases: if the tunneling is entirely spin-preserving or enterily spin-flipping ($\theta_T = 0$ or $\theta_T = \pi/2$), we get $R_{14,14} = (2G_0)^{-1}$, if the tunneling is equally composed of spin-preserving and spin-flipping terms ($\theta_T = \pi/4$), we have in this case $R_{14,14} = 3/(4G_0)$. The minima correspond to the resonance energies, where their values are given by the value of $\theta_T(\mu)$. If we are

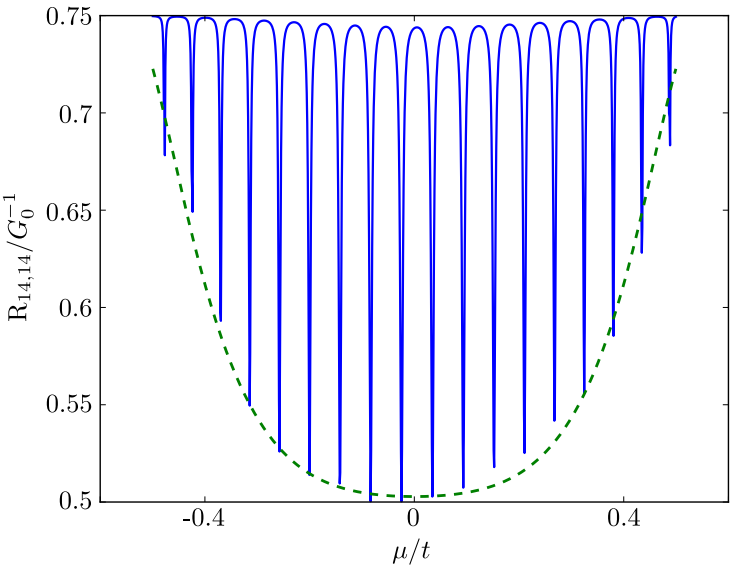

Figure 3.5: The resistance $R_{14,14}$ with respect to the chemical potential μ. We used the following parameters $a = 1$, $t = 1$, $\lambda_{\mathrm{SO}} = 0.2$ and $\lambda_{\mathrm{R},1}$. The continuous (blue) line corresponds to the numerical results from the tight-binding model. The dashed (green) line corresponds to the fitting from the analytic model assuming that $\theta_T(\mu) \approx \alpha\mu^2 + \beta$.

further away from resonance, the resistance corresponds to the value of a normal Hall bar without an antidot: $R_{14,14} = 3/(4G_0)$. We find that around $\mu = 0$ there is a small dip, deviating from the quantized value (it is already seen in the transmission plots of Fig. 3.3). Its origin is in the finite length of the tunneling region, which tends to open a small spectral gap [114, 115]. We are able to evaluate the behavior of $\theta_T(\mu)$ at small μ by fitting Eq. (3.19) (green dashed line), such that $\theta_T(\mu) - \theta_T(0) \propto \mu^2$.

To summarize this section, the spin texture is expressed explicitly by the difference of spin texture between the two external edges if the Hall bar has an inhomogeneous Rashba SOC. In the case of a homogeneous Rashba SOC, the spin texture is implicitly expressed by θ_T. The numerical simulations enable us to evaluate the analytic parameters as functions of the chemical potential and extract their dependence on the tight-binding parameters.

3.3 Probing the spin texture with an interacting antidot

To complete the discussion about spin texture in a Hall bar, we need to take into account the interactions between the electrons and how they affect the transport calculations. Due to the interactions, computing the transport quantities with scattering

matrices are no longer possible any more. Moreover, if the strength of the tunneling is arbitrary, it is not possible to obtain an analytic and exact expression for the transport quantities. Hence, only the lowest-order contributions to the tunneling current across the antidot are computed. The first-order contribution gives sequential tunneling and the second-order contribution gives cotunneling [116].

3.3.1 Sequential tunneling regime

In the sequential tunneling regime, we assume single-electron transfers between the outer edges and the antidot to dominate the transport processes. This happens when the dwell time τ is the largest time scale involved, $1/\tau \ll \{eV_i, k_BT\}$. In this regime we are able to evaluate the transport quantities as a first-order perturbation expansion in $|\gamma_T|^2$. We make the assumption that the antidot has a ground state containing N electrons and without loss of generality, N is even. In the leads, the initial state contains an electron in one of the s leads. It has a certain momentum k and certain chirality α. We can describe the total initial state, which includes the leads and the antidot as:

$$|i^{s\alpha}(N,k)\rangle = |N\rangle \otimes c^{\dagger}_{s\alpha k}|\text{vac}\rangle. \tag{3.20}$$

The final state can be described as the state where an electron from the s edge with momentum k and chirality α tunnels to the antidot with a final chirality α' and an angular momentum j. It can be expressed as

$$|f^{s\alpha\alpha'}(N+1,k,j)\rangle = d^{\dagger}_{\alpha' j} c_{s\alpha k}|i^{s\alpha}(N,k)\rangle. \tag{3.21}$$

We can then compute the transmission probability from the initial to the final state using Fermi's golden rule [116]

$$\Gamma^{s\alpha\alpha'}_{N+1,N}(k,j) = 2\pi|\langle f|\mathcal{H}_{d,s}|i\rangle|^2 F_i \delta(E_f - E_i), \tag{3.22}$$

where the energy is conserved between the final and initial state $E_f - E_i = E(N+1) - E(N) + \varepsilon_{d\alpha'}(j) - \varepsilon_{s\alpha}(k)$ and F_i is the Fermi function, which indicates the probability to have the initial state $|i\rangle$. The eigenenergy of the antidot with angular momentum j and chirality α' is denoted $\varepsilon_{d\alpha'}(j)$, and $\varepsilon_{s\alpha}(k)$ is the eigenenergy of the s edge with chirality α and momentum k. One transmission process can be seen for example in Fig. 3.6. We obtain the total transmission probability by summing over all initial and final states

$$\Gamma^{s\alpha\alpha'}_{N+1,N} = \sum_{j,k} \Gamma^{s\alpha\alpha'}_{N+1,N}(k,j). \tag{3.23}$$

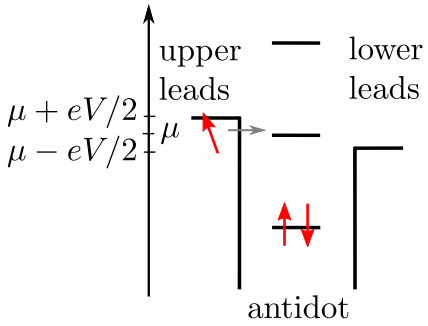

Figure 3.6: Sketch of a possible sequential tunneling process from the upper edge to the lower edge. There is an even number of electrons on the antidot, such that the electron from the upper edge can tunnel to the antidot with an arbitrary chirality.

We can compute the sequential tunneling current using a rate-equation approach. We can consider two occupation numbers only: N and $N+1$ and the dc limit, these approximations are valid as long as the charging energy is large enough to forbid other occupation numbers. At the steady state, it yields the following recursion relation

$$\Gamma_{N+1,N} P(N) = \Gamma_{N,N+1} P(N+1), \tag{3.24}$$

where $\Gamma_{N+1,N} = \sum_{s,\alpha,\alpha'} \Gamma^{s\alpha\alpha'}_{N+1,N}$ and similarly for $\Gamma_{N,N+1}$. As N is even, there is only one possible occupation probability, namely $P(N)$. However, the probability of an occupation of $N+1$ electrons is two-fold degenerate due to the two possible chiralities. Conservation of probability then requires that $P(N) + 2P(N+1) = 1$. With the help of the recursion relation and the conservation of probability constraint, the occupation probabilities can be computed in terms of the transition rates as

$$\begin{aligned} P(N) &= \frac{\Gamma_{N,N+1}}{\Gamma_{N,N+1} + 2\Gamma_{N+1,N}}, \\ P(N+1) &= \frac{\Gamma_{N+1,N}}{\Gamma_{N,N+1} + 2\Gamma_{N+1,N}}. \end{aligned} \tag{3.25}$$

The transitions between the N and the $N+1$ occupations are only allowed near the resonance condition $\Delta E(N+1) \equiv E(N+1) - E(N) = 0$. This condition happens when the gate voltage is tuned such that $n_g \approx N + 1/2$, with $n_g = eV_g/E_c$. Note that the charging energy E_c also influences the occupation number. The total current can be expressed in terms of probabilities and transition rates as

$$I = -e\left[P(N)\Gamma^U_{N+1,N} - P(N+1)\Gamma^U_{N,N+1}\right], \tag{3.26}$$

where $\Gamma^U_{N+1,N} = \sum_{\alpha,\alpha'} \Gamma^{U\alpha\alpha'}_{N+1,N}$ and similarly for $\Gamma^U_{N,N+1}$. The current expression is still

complicated as it can involve, as many levels as can be found in the bias window. If we restrict the width of the bias window sufficiently, there is only one energy level $\varepsilon_d(j)$ located near the chemical potential μ. We get the following current

$$I = -e\frac{2\Gamma_T}{\pi R}\frac{n_F(\varepsilon_d(j)-\mu_U) - n_F(\varepsilon_d(j)-\mu_L)}{2+[n_F(\varepsilon_d(j)-\mu_U) + n_F(\varepsilon_d(j)-\mu_L)]}, \tag{3.27}$$

with $\Gamma_T = |\gamma_T|^2/(2v_F)$ and $n_F(\varepsilon)$ is the Fermi-Dirac distribution. We set the chemical potentials to $\mu_U = \mu + eV/2$ and $\mu_L = \mu - eV/2$, where V is the bias voltage between upper and lower edges. At zero temperature and finite voltage, the current becomes

$$I_{T=0} = -\frac{2e\Gamma_T}{3\pi R}. \tag{3.28}$$

Whereas at finite temperature and at small voltage $eV \ll k_BT$, the current in the linear regime becomes

$$I_{T\neq 0} = -\frac{1}{4k_BT}\frac{\Gamma_T}{\pi R}\frac{e^2V}{1+n_F(\tilde{\varepsilon}_d)}\frac{1}{\cosh^2(\tilde{\varepsilon}_d/(2k_BT))}, \tag{3.29}$$

with $\tilde{\varepsilon}_d = \varepsilon_d(j) - \mu$. Note that these two different results are not contradicting, as the two limits $eV \to 0$ and $k_BT \to 0$ do not commute in the sequential tunneling regime [117].

The rate-equation approach assumes that the electrons relax to the ground state between two tunneling events so that we have two well separated time scales: the fast relaxation time and the slow tunneling time. Nonetheless due to time-reversal symmetry, we have either an initial state $|N\rangle$ or a twofold degenerate final state $|N+1\rangle$. We are not able to keep track of the chirality of the electrons in the antidot using this approach, and then to compute chirality-resolved currents. Therefore, we are only able to compute the total current I, which contains no information about the spin texture. We continue to second order perturbation theory in order to explore coherent transport across the antidot.

3.3.2 Cotunneling regime

If the bias window is chosen such that there is no energy level in it, the sequential tunneling is forbidden. Still a current can be created through the antidot, via a virtual state: this is what we call the cotunneling regime. A sketch of a possible process is shown in Fig. 3.7. We will consider elastic cotunneling, i.e. the initial and the final states of the antidot are the same. As the antidot has a discrete number of levels, such process becomes more relevant in this regime, compared to the inelastic one [116].

The initial state $|i^{s\alpha}(N,k)\rangle$ is similar to what we described in the sequential regime:

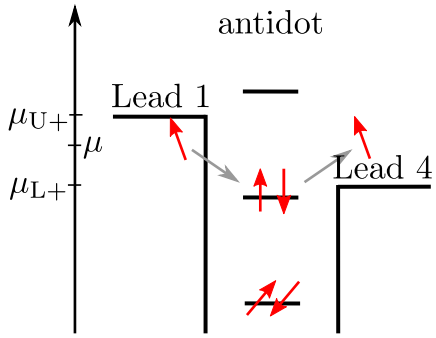

Figure 3.7: Sketch of a possible cotunneling tunneling process from lead 1 to lead 4. The antidot energy level is fully occupied. One electron of the antidot escape towards lead 4, creating a virtual hole on the antidot. The final state is attained when the energy level of the antidot is again filled by an electron originating from lead 1.

the antidot has N electrons and on the s edge, there is an electron with momentum k and chirality α. Analogously, the final state $|f^{s'\alpha'}(N,k')\rangle$ has N electrons in the antidot and an electron on the s' edge with momentum k' and chirality α'. The cotunneling rate is defined as

$$\Gamma_{i\to f} = 2\pi\delta(E_f - E_i)F_i \left| \left\langle f \left| \mathcal{H}_{d,L}\frac{1}{E_i - \mathcal{H}_0}\mathcal{H}_{d,U} + \mathcal{H}_{d,U}\frac{1}{E_i - \mathcal{H}_0}\mathcal{H}_{d,L} \right| i \right\rangle \right|^2 , \tag{3.30}$$

where $\mathcal{H}_0 = \mathcal{H}_U + \mathcal{H}_L + \mathcal{H}_d$, and E_i (E_f) is the initial (final) energy. F_i represents again the Fermi distribution, which describes the probability to have the initial state $|i^{s\alpha}(N,k)\rangle$. Note that the electrons in the antidot N remain in the ground state in the initial and in the final states.

To obtain the chirality-resolved cotunneling rates $\Gamma^{\alpha\alpha'}_{U\to L}$ and $\Gamma^{\alpha\alpha'}_{L\to U}$, we need to sum over all possible initial and final momenta. We need as well to sum over all angular momenta and chiralities of the intermediate state in the antidot. With these chirality-resolved cotunneling rates, we are able to express a chirality-resolved current

$$I^{\alpha\alpha'} = (-e)\left[\Gamma^{\alpha\alpha'}_{U\to L} - \Gamma^{\alpha'\alpha}_{L\to U}\right]. \tag{3.31}$$

To connect these chirality-resolved currents with the ones described in the previous section and in the setup in Fig. 3.1, we are able to identify I^{++} as the current flowing from lead 1 to lead 4, I^{+-} the current flowing from lead 1 to lead 3, I^{-+} the current flowing from lead 2 to lead 4, and I^{--} the current flowing from lead 2 to lead 3. The final results for these currents are strongly influenced by the initial antidot occupation, i.e. if the antidot has an even or an odd number of electrons.

We can start with an even occupation consisting of N electrons on the antidot. This means that all the energy levels up to the chemical potential are doubly occupied, similarly

to what is shown in Fig. 3.7. We get the following chirality-resolved tunnelings

$$\Gamma^{\alpha\alpha'}_{U\to L} = -\frac{e\Gamma_T^2}{2\pi^3 R^2}\sum_j \int d\varepsilon n_F(\varepsilon-\mu_{U\alpha})[1-n_F(\varepsilon-\mu_{L\alpha'})]\frac{\cos^2(2\theta_T)\delta_{\alpha'\alpha}+\sin^2(2\theta_T)\delta_{\bar{\alpha}'\alpha}}{\left[\varepsilon-\varepsilon_d(j)-\Delta E\right]^2},$$
$$\Gamma^{\alpha'\alpha}_{L\to U} = -\frac{e\Gamma_T^2}{2\pi^3 R^2}\sum_j \int d\varepsilon n_F(\varepsilon-\mu_{L\alpha'})[1-n_F(\varepsilon-\mu_{U\alpha})]\frac{\cos^2(2\theta_T)\delta_{\alpha\alpha'}+\sin^2(2\theta_T)\delta_{\bar{\alpha}\alpha'}}{\left[\varepsilon-\varepsilon_d(j)-\Delta E\right]^2}, \tag{3.32}$$

where $\varepsilon_d(j)+\Delta E$ is the energy of the intermediate virtual state. If the intermediate state is an additional hole at the jth energy level, then $\Delta E = \Delta E(N)$. Otherwise, if the intermediate state is an additional electron, then $\Delta E = \Delta E(N+1)$. The two cases can be differentiated by the value of the gate voltage. Using Eq. (3.31), and taking into account the properties of Fermi-Dirac distributions, we get

$$I^{\alpha\alpha'}_{N\ \text{even}} = -\frac{e\Gamma_T^2}{2\pi^3 R^2}\sum_j \int d\varepsilon [n_F(\varepsilon-\mu_{U\alpha})-n_F(\varepsilon-\mu_{L\alpha'})]\frac{\cos^2(2\theta_T)\delta_{\alpha'\alpha}+\sin^2(2\theta_T)\delta_{\bar{\alpha}'\alpha}}{\left[\varepsilon-\varepsilon_d(j)-\Delta E\right]^2}. \tag{3.33}$$

In the linear response limit for the bias voltage, the Fermi functions can be expanded near the chemical potential μ. Moreover, we consider that the j_0th energy level of the antidot, the one which is the closest to the chemical potential, contributes to the cotunneling current and $\Delta E + \varepsilon_d(j_0) \gg \mu_{U/L,\alpha/\alpha'}$. The current then becomes

$$I^{\alpha\alpha'}_{N\ \text{even}} \approx -\frac{e^2(V_\alpha - V_{\alpha'})\Gamma_T^2}{2\pi^3 R^2}\frac{\cos^2(2\theta_T)\delta_{\alpha'\alpha}+\sin^2(2\theta_T)\delta_{\bar{\alpha}'\alpha}}{\left[\mu-\varepsilon_d(j_0)-\Delta E\right]^2}, \tag{3.34}$$

where θ_T is estimated at the chemical potential μ. We observe that the spin texture is again implicitly encoded in the value of θ_T. The effect of the interactions is to shift the energy in the denominator by the Coulomb charging energy. By inverting the expression for the current, we are able to extract the value of θ_T and its dependence on the current, voltage and charging energy. It would then be in theory an easy manner to implicitly compare the effect of interaction and its absence on the spin texture.

We can now calculate the current in the case of an odd occupation number. This means that all the energy levels up to the chemical potential are doubly occupied, except the last one. We will see that the behavior is quite different from the previous case. An example of such a process can be seen in Fig. 3.8. We have to take into account now the degeneracy of the antidot energy level in our computations. The initial state $|i^{s\alpha\beta}(N,k)\rangle$ includes the chirality β of the antidot and the final state $|f^{s'\alpha'\beta'}(N,k')\rangle$ also depends upon the chirality β' of the antidot [118]. The cotunneling rates are obtained using Eq. (3.30), where F_i takes also into account the additional degree of freedom due to the chirality of

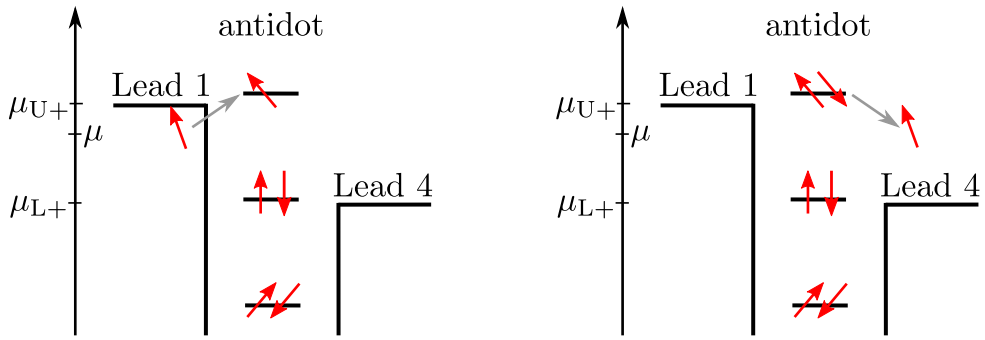

Figure 3.8: Sketch of a possible cotunneling tunneling process occurring between lead 1 and lead 4. The antidot energy level is considered to be half occupied. Initially, one electron from lead 1 tunnels to the half occupied antidot level. The final state is attained when one of the electron tunnels towards lead 4.

the antidot. We get 16 different transition rates

$$\Gamma^{\alpha\alpha\beta\beta}_{U\to L} = \frac{\Gamma_T^2}{8\pi^3 R^2}\sum_j \int d\varepsilon n_F(\varepsilon-\mu_{U\alpha})[1-n_F(\varepsilon-\mu_{L\alpha})] \left[\frac{\cos(2\theta_T)+\alpha\beta\cos(2\theta_k-2\theta_j)}{\varepsilon_d(j)+\Delta E(N)-\varepsilon}+\frac{\cos(2\theta_T)-\alpha\beta\cos(2\theta_k-2\theta_j)}{\varepsilon-\varepsilon_d(j)-\Delta E(N+1)}\right]^2, \tag{3.35}$$

$$\Gamma^{\alpha\alpha\beta\bar{\beta}}_{U\to L} = \frac{\Gamma_T^2}{8\pi^3 R^2}\sum_j \int d\varepsilon n_F(\varepsilon-\mu_{U\alpha})[1-n_F(\varepsilon-\mu_{L\alpha})] \left[\frac{\sin(2\theta_T)+\alpha\beta\sin(2\theta_k-2\theta_j)}{\varepsilon_d(j)+\Delta E(N)-\varepsilon}+\frac{\sin(2\theta_T)+\alpha\beta\sin(2\theta_k-2\theta_j)}{\varepsilon-\varepsilon_d(j)-\Delta E(N+1)}\right]^2, \tag{3.36}$$

$$\Gamma^{\alpha\bar{\alpha}\beta\beta}_{U\to L} = \frac{\Gamma_T^2}{8\pi^3 R^2}\sum_j \int d\varepsilon n_F(\varepsilon-\mu_{U\alpha})[1-n_F(\varepsilon-\mu_{L\bar{\alpha}})] \left[\frac{\sin(2\theta_T)-\alpha\beta\sin(2\theta_k-2\theta_j)}{\varepsilon_d(j)+\Delta E(N)-\varepsilon}+\frac{\sin(2\theta_T)+\alpha\beta\sin(2\theta_k-2\theta_j)}{\varepsilon-\varepsilon_d(j)-\Delta E(N+1)}\right]^2, \tag{3.37}$$

$$\Gamma^{\alpha\bar{\alpha}\beta\bar{\beta}}_{U\to L} = \frac{\Gamma_T^2}{8\pi^3 R^2}\sum_j \int d\varepsilon n_F(\varepsilon-\mu_{U\alpha})[1-n_F(\varepsilon-\mu_{L\bar{\alpha}})] \left[\frac{\cos(2\theta_T)-\alpha\beta\cos(2\theta_k-2\theta_j)}{\varepsilon_d(j)+\Delta E(N)-\varepsilon}+\frac{\cos(2\theta_T)-\alpha\beta\cos(2\theta_k-2\theta_j)}{\varepsilon-\varepsilon_d-\Delta E(N+1)}\right]^2. \tag{3.38}$$

The other transition rates $\Gamma^{\alpha'\alpha\beta\beta'}_{L\to U}$ are obtained by detailed balance. Moreover due to the

chirality degree of freedom, the current is now

$$I^{\alpha\alpha'} = (-e)\sum_{\beta,\beta'}\left[\Gamma^{\alpha\alpha'\beta\beta'}_{\mathrm{U}\to\mathrm{L}} - \Gamma^{\alpha'\alpha\beta\beta'}_{\mathrm{L}\to\mathrm{U}}\right]p_\beta. \tag{3.39}$$

The probabilities p_β correspond to the probabilities of the highest level of the antidot to have an electron with chirality β. The conservation of probability requires that $p_+ + p_- = 1$ and the rate equation gives

$$\frac{dp_\beta}{dt} = -\Gamma^{\beta\bar{\beta}}p_\beta + \Gamma^{\bar{\beta}\beta}p_{\bar{\beta}} = 0, \tag{3.40}$$

with $\Gamma^{\beta\bar{\beta}} = \sum_{\alpha\alpha'}\Gamma^{\alpha\alpha'\beta\bar{\beta}}_{U\to L} + \Gamma^{\alpha\alpha'\beta\bar{\beta}}_{L\to U}$ determining them. If we can compute the tunneling rates at the chosen chemical potentials, we are able to evaluate the cotunneling currents.

We will look for two different chemical potential configurations. If we start with having a difference of voltage between the upper and the lower leads, we get the following chemical potentials: $\mu_{U+} = \mu_{U-} = \mu + \frac{eV}{2}$ and $\mu_{L+} = \mu_{L-} = \mu - \frac{eV}{2}$. The chirality probabilities are evaluated to be $p_+ = p_- = 1/2$. The current is then evaluated in the linear regime and we assume that only the closest j_0th level contribute by being half occupied, such that

$$I^{\alpha\alpha'}_{N\ \mathrm{odd}} \approx -\frac{2\Gamma_T^2 G_0 V}{v_F^2}\left[\frac{1}{\xi^2(N)} + \frac{1}{\xi^2(N+1)} + \frac{\alpha\alpha'\cos\left(4\theta_{k_F} - 4\theta_{j_0}\right) - 1}{\xi(N)\xi(N+1)}\right], \tag{3.41}$$

with $\xi(N) = 2\pi R[\varepsilon_d(j_0) + \Delta E(N) - \mu]/v_F$. Note that we supposed that the rotation is slow enough to approximate the spin texture of the outer edges as the one evaluated at the chemical potential, before we perform the integrals over the energy. This approximation is consistent with the values obtained in Tab. 2.1. We observe that the current is explicitly dependent on the spin texture through θ_{k_F} and θ_{j_0}, even in the case of homogeneous Rashba SOC. In this cotunneling configuration, a current measurement would enable us to gain some information about the relative difference of spin texture between the antidot and the outer edges. As the intermediate state is virtual, i.e. the energy is not conserved, the spin texture measured by θ_{k_F} will in principle differ from the one measured on the antidot, θ_{j_0}. In particular, if we study the difference of current between the lower contacts, we will get

$$I^{+-}_{N\ \mathrm{odd}} - I^{++}_{N\ \mathrm{odd}} \approx G_0 V\left(\frac{2\Gamma_T}{v_F}\right)^2\frac{\cos\left(4\theta_{k_F} - 4\theta_{j_0}\right)}{\xi(N)\xi(N+1)}, \tag{3.42}$$

which gives us a direct means to obtain the spin texture.

The second configuration is when only one lead is biased, for example lead 1. The chemical potentials are set to $\mu_{U+} = \mu + eV$ and $\mu_{U-} = \mu_{L+} = \mu_{L-} = \mu$. The chirality probabilities are now slightly more complicated $p_+ \approx \cos^2(\theta_{k_F} - \theta_{j_0} + \theta_T)$ and $p_- \approx$

$\sin^2(\theta_{k_F} - \theta_{j_0} + \theta_T)$. Two of the currents I^{-+} and I^{--} are zero, as there is no voltage bias between their leads. We are also able to evaluate the two other chirality-resolved currents

$$\begin{aligned} I^{+-}_{N\ \mathrm{odd}} \approx -\frac{2\Gamma_T^2 G_0 V}{v_F^2}\left(\frac{1}{\xi(N+1)\xi(N)}\right)^2 \{&\xi^2(N+1)+\xi^2(N) \\ &-\xi(N+1)\xi(N)\left[1+\cos\left(4\theta_{k_F}-4\theta_{j_0}\right)\right] \\ &-\left[\xi(N+1)-\xi(N)\right]\cos\left(2\theta_{k_F}-2\theta_{j_0}+2\theta_T\right) \\ &\times\left[\xi(N+1)\cos\left(2\theta_{k_F}-2\theta_{j_0}-2\theta_T\right)-\xi(N)\cos\left(2\theta_{k_F}+2\theta_{j_0}+2\theta_T\right)\right]\}, \end{aligned} \tag{3.43}$$

$$\begin{aligned} I^{++}_{N\ \mathrm{odd}} \approx -\frac{2\Gamma_T^2 G_0 V}{v_F^2}\left(\frac{1}{\xi(N+1)\xi(N)}\right)^2 \{&\xi^2(N+1)+\xi^2(N) \\ &-\xi(N+1)\xi(N)\left[1-\cos\left(4\theta_{k_F}-4\theta_{j_0}\right)\right] \\ &+\left[\xi(N+1)-\xi(N)\right]\cos\left(2\theta_{k_F}-2\theta_{j_0}+2\theta_T\right) \\ &\times\left[\xi(N+1)\cos\left(2\theta_{k_F}-2\theta_{j_0}-2\theta_T\right)+\xi(N)\cos\left(2\theta_{k_F}+2\theta_{j_0}+2\theta_T\right)\right]\}. \end{aligned} \tag{3.44}$$

The current expressions are more complicated than the ones in the previous example. To check the consistency of our result, we compute the case in the absence of Rashba SOC, i.e. $\theta_k = \theta_j = \theta_T = 0$. The chirality probabilities become $p_+ = 1$ and $p_- = 0$. Only electrons with + chirality can tunnel in to and out of the antidot. Moreover, the currents become

$$I^{+-}_{N\ \mathrm{odd}} = 0, \tag{3.45}$$

$$I^{++}_{N\ \mathrm{odd}} \approx -\frac{4\Gamma_T^2 G_0 V}{v_F^2}\frac{1}{\xi(N)^2}. \tag{3.46}$$

The current flowing to lead 3 vanishes as expected. The current flowing to lead 4 can be understood as a spin-up polarized current, leading to an occupation of the last level of the antidot to be up-spin only. The current will then be the same (up to a shift of the charging energy) as in the even case. The cotunneling process will be: first, the electron enters lead 4 from the antidot and then an electron from lead 1 enters the antidot. Such a current distribution is schematically shown in Fig. 3.9(a). On the contrary, if Rashba SOC is important, we could reach a regime where the spin-flipping current is the dominant current contribution. This would mean that most of the electrons entering in lead 1 would exit the setup in lead 3. Such a process is also schematically shown in Fig. 3.9(b).

To summarize this exploration of the interacting sector, the transport measurements are strongly influenced by the occupation of the antidot in the cotunneling regime. This occupation can be tuned by the gate voltage. If we have an even number of electrons on the antidot, the spin texture will appear implicitly by enabling spin-flipping currents and its strength will be measured by the value of θ_T. We recover a behavior on the spin texture relatively similar to what we observed in the non-interacting regime. On the other

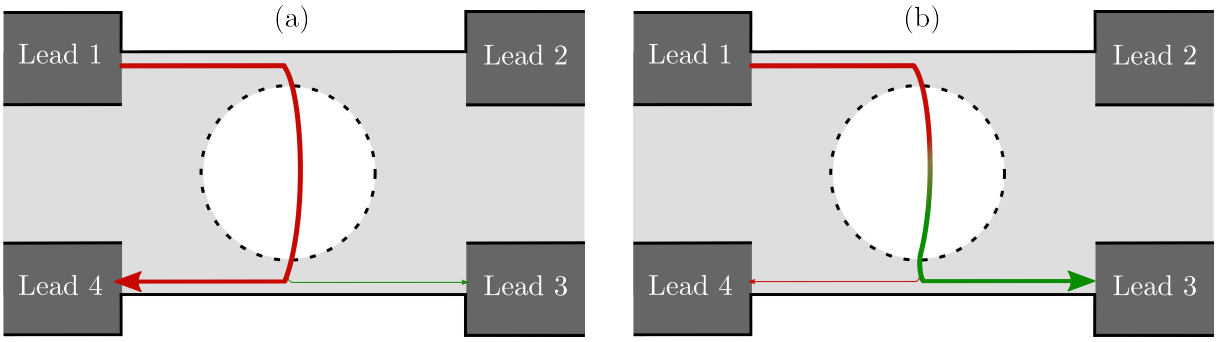

Figure 3.9: Schematic picture of the two current processes $I^{+-}_{N\,\mathrm{odd}}$ and $I^{++}_{N\,\mathrm{odd}}$ when the bias configuration is set to $\mu_{U+} = \mu + eV$ and $\mu_{U-} = \mu_{L+} = \mu_{L-} = \mu$. In panel (a), we have weak Rashba SOC, which implies that most of the electrons are transmitted to lead 4. On the other hand, if Rashba SOC is large enough, the majority of the electrons can flow to lead 3 as shown in panel (b).

hand, if we have an odd number of electrons on the antidot, there is this time an explicit dependence on the spin texture. By tuning the chemical potential configurations, we are able to probe the behavior of the spin texture via the implicit dependence on θ_T and also via the explicit dependence on θ_{k_F} and θ_{j_0}.

4 | Spin texture in InAs/GaSb heterostructures

Up to now, we characterized the spin texture and developed spectroscopic frameworks to extract information about the spin texture. One of the key ingredients to measure the spin texture is to have either bulk and/or structural inversion asymmetries. It was pointed out recently [65], that in the presence of SOC, the bandstructure shows anisotropic behavior, which makes it spatially dependent on the crystallographical orientation. To analyze the spin texture, we will start from the $k \cdot p$ Hamiltonian presented in [65] and we will derive an effective two-dimensional Hamiltonian similar to the BHZ model, Eq. (1.23). We will restore $\hbar$ and c in this chapter for dimensional purposes.

4.1 Basics about $k \cdot p$ theory

$k \cdot p$ theory is a method used to describe the band structure of semiconductors. Several books, for example [49, 56], introduce $k \cdot p$ theory and provide more details than the present introduction. Here, we will only present the most relevant derivations and features of the theory.

The idea behind the $k \cdot p$ approach is to apply perturbation theory near one extremum of the energy at momentum $\mathbf{k_0}$ to obtain the band structure. We will start by considering the n^{th} band. As the electrons are located in a lattice, we can use Bloch's theorem to describe the wave function

$$\psi_{n\mathbf{k}}(\mathbf{r}) = e^{i\mathbf{kr}} u_{n\mathbf{k}}(\mathbf{r}). \tag{4.1}$$

This wave function should also satisfy the Schrödinger equation $\mathcal{H}\psi_{n\mathbf{k}}(\mathbf{r}) = E_n(\mathbf{k})\psi_{n\mathbf{k}}(\mathbf{r})$. We consider the Hamiltonian

$$\mathcal{H} = \frac{p^2}{2m_0} + V(\mathbf{r}) + \frac{\hbar}{4m_0^2c^2}(\boldsymbol{\sigma} \times \nabla V) \cdot \mathbf{p}, \tag{4.2}$$

where the first term is the kinetic term and m_0 is the free electron mass. The second term of the Hamiltonian is the external potential and the last term is the SOC. It leads to the

following equation for the functions $u_{n\mathbf{k}}$

$$\left[\frac{p^2}{2m_0}+\frac{\hbar^2k^2}{2m_0}+V+\frac{\hbar}{m_0}\mathbf{k}\cdot\boldsymbol{\pi}+\frac{\hbar}{4m_0^2c^2}(\boldsymbol{\sigma}\times\nabla V)\cdot\mathbf{p}\right]u_{n\mathbf{k}}(\mathbf{r})=E_n(\mathbf{k})u_{n\mathbf{k}}(\mathbf{r}), \tag{4.3}$$

where $\boldsymbol{\pi}=\mathbf{p}+\frac{\hbar}{4m_0^2c^2}\boldsymbol{\sigma}\times\nabla V$. Note that we distinguish the lattice momentum $\mathbf{k}$, which is a number from the momentum operator $\mathbf{p}$. Moreover, the functions $u_{n\mathbf{k}}$ form a complete basis, such that they exactly diagonalize the (infinite) Hamiltonian.

To simplify the calculation, we apply a canonical transformation [49, 56, 119, 120] to get an approximate solution at small $\mathbf{k}$ near one extremum of energy

$$\frac{\partial E_n(\mathbf{k_0})}{\partial k_i}=0. \tag{4.4}$$

If we assume that the energy extremum is at $\mathbf{k_0}=\mathbf{0}$, the unperturbed Hamiltonian becomes

$$\mathcal{H}_0=\frac{p^2}{2m_0}+V+\frac{\hbar}{4m_0^2c^2}(\boldsymbol{\sigma}\times\nabla V)\cdot\mathbf{p}. \tag{4.5}$$

The solutions of this Hamiltonian are given by $u_{n\mathbf{0}}$ and their energy is $E_n(\mathbf{0})$. The perturbation is then

$$\mathcal{H}_1=\frac{\hbar^2k^2}{2m_0}+\frac{\hbar}{m_0}\mathbf{k}\cdot\boldsymbol{\pi}. \tag{4.6}$$

We can decompose the functions $u_{n\mathbf{k}}$ as

$$u_{n\mathbf{k}}=\sum_{n'}b_{nn'}(\mathbf{k})u_{n'\mathbf{0}}, \tag{4.7}$$

where the $u_{n'\mathbf{0}}$ functions still form a complete set of orthogonal functions. We replace $u_{n\mathbf{k}}$ in Eq. (4.3) by this decomposition and use $\frac{(2\pi)^3}{\Omega}\int d^3\mathbf{r}u^*_{n\mathbf{0}}(\mathbf{r})u_{n'\mathbf{0}}(\mathbf{r})=\delta_{nn'}$ to get

$$\begin{aligned}b_{nn}(\mathbf{k})E_n(\mathbf{0})+\frac{\hbar^2k^2}{2m_0}b_{nn}(\mathbf{k})+\frac{\hbar}{m_0}\mathbf{k}\cdot\sum_{n'}b_{nn'}(\mathbf{k})\frac{(2\pi)^3}{\Omega}\int d^3\mathbf{r}u^*_{n\mathbf{0}}(\mathbf{r})\boldsymbol{\pi}u_{n'\mathbf{0}}(\mathbf{r})&=b_{nn}(\mathbf{k})E_n(\mathbf{k}),\\ b_{nn}(\mathbf{k})E_n(\mathbf{0})+\frac{\hbar^2k^2}{2m_0}b_{nn}(\mathbf{k})+\frac{\hbar}{m_0}\mathbf{k}\cdot\sum_{n'}b_{nn'}(\mathbf{k})\boldsymbol{\pi}_{nn'}&=b_{nn}(\mathbf{k})E_n(\mathbf{k}),\end{aligned} \tag{4.8}$$

where $\boldsymbol{\pi}_{nn'}=\frac{(2\pi)^3}{\Omega}\int d^3\mathbf{r}u^*_{n\mathbf{0}}(\mathbf{r})\boldsymbol{\pi}u_{n'\mathbf{0}}(\mathbf{r})$. The equation above is more complicated than the previous version as there is now a coupling term between the different bands. The solution is to apply a canonical transformation, namely the Schrieffer-Wolff transformation. We can define a new Hamiltonian using the following transformation, $\tilde{\mathcal{H}}=T^{-1}\mathcal{H}T$. $T=e^S$ decouples the n^{th} band from the n' bands. We define now $\tilde{\mathcal{H}}_0=\mathcal{H}_0+\frac{\hbar^2k^2}{2m_0}$ and $\tilde{\mathcal{H}}_1=\frac{\hbar}{m_0}\mathbf{k}\cdot\boldsymbol{\pi}$,

the latter being the term coupling the bands. We expand T in terms of S, such that

$$\tilde{\mathcal{H}} = \tilde{\mathcal{H}}_0 + \tilde{\mathcal{H}}_1 + [\tilde{\mathcal{H}}_0, S] + [\tilde{\mathcal{H}}_1, S] + \frac{1}{2}[[\tilde{\mathcal{H}}_0, S], S] + \mathcal{O}(k^3) \tag{4.9}$$

Since the coupling with the other bands is induced by $\tilde{\mathcal{H}}_1$, we can cleverly choose S such that $\tilde{\mathcal{H}}_1 + [\tilde{\mathcal{H}}_0, S] = 0$, so that $\tilde{\mathcal{H}} = \tilde{\mathcal{H}}_0 + \frac{1}{2}[\tilde{\mathcal{H}}_1, S] + \mathcal{O}(k^3)$. When $n \neq n'$, the elements of S are then determined as

$$\langle u_{n\mathbf{0}}|S|u_{n'\mathbf{0}}\rangle = -\frac{\hbar}{m_0}\frac{\mathbf{k}\cdot\boldsymbol{\pi}_{nn'}}{E_n(\mathbf{0}) - E_{n'}(\mathbf{0})}. \tag{4.10}$$

We are able to express, up to second order in $\mathbf{k}$, the matrix elements of the Hamiltonian $\tilde{\mathcal{H}}$

$$\langle u_{n\mathbf{0}}|\tilde{\mathcal{H}}|u_{n'\mathbf{0}}\rangle \approx \left(E_n(\mathbf{0}) + \frac{\hbar^2k^2}{2m_0}\right)\delta_{nn'} + \frac{\hbar^2}{2m_0^2}\sum_{n''\neq n'}\frac{\mathbf{k}\cdot\boldsymbol{\pi}_{nn''}\mathbf{k}\cdot\boldsymbol{\pi}_{n''n'}}{E_{n'}(\mathbf{0}) - E_{n''}(\mathbf{0})} + \sum_{n''\neq n}\frac{\mathbf{k}\cdot\boldsymbol{\pi}_{nn''}\mathbf{k}\cdot\boldsymbol{\pi}_{n''n'}}{E_n(\mathbf{0}) - E_{n''}(\mathbf{0})}. \tag{4.11}$$

We can directly notice that the more distant bands will then have weaker corrections compared to the closest ones, as the energy difference is in the denominator. We can then approximate the Hamiltonian with only the contribution of the closest bands. Moreover, we are able to compute a correction of the band mass as

$$\frac{m_0}{m_n^*} \approx 1 + \frac{2}{m_0}\sum_{n'\neq n}\frac{|\pi|^2_{nn'}}{E_n(\mathbf{0}) - E_{n'}(\mathbf{0})}. \tag{4.12}$$

Up to now, we considered the effect on a single band, labelled by n. However, we would like to approximate the complete bandstructure of the zinc blende lattice using its space group symmetries near the Γ point ($\mathbf{k} = \mathbf{0}$). We focus on only the four bands near the Fermi energy: one conduction band and three valence bands. Due to TR-symmetry, these bands are always doubly-degenerate. We have the s-like conduction band ($l = 0$), with total angular momentum $j = 1/2$. Its irreducible representation is Γ_6. The p-like valence band ($l = 1$) splits into three subbands. Two subbands remain degenerate at $\mathbf{k} = \mathbf{0}$ and have a total angular momentum of $j = 3/2$. These are the heavy and light hole bands and their irreducible representation is Γ_8. The last subband is also split at $\mathbf{k} = \mathbf{0}$ by an energy Δ due to SOC, and has a total angular momentum $j = 1/2$. It is called the spin-orbit split-off valence band and has a Γ_7 irreducible representation. The gap at $\mathbf{k} = \mathbf{0}$ between the Γ_8 and Γ_6 bands is given by $E_g = E_c - E_v$. The band structure is shown in Fig. 4.1. When the other bands are perturbatively included to this 8 band model, it is called the Kane model [121]. Due to the symmetry of the bands, we can rewrite them as combination of $|S\rangle$, $|X\rangle$, $|Y\rangle$ and $|Z\rangle$, the elements forming s-like and p-like orbitals

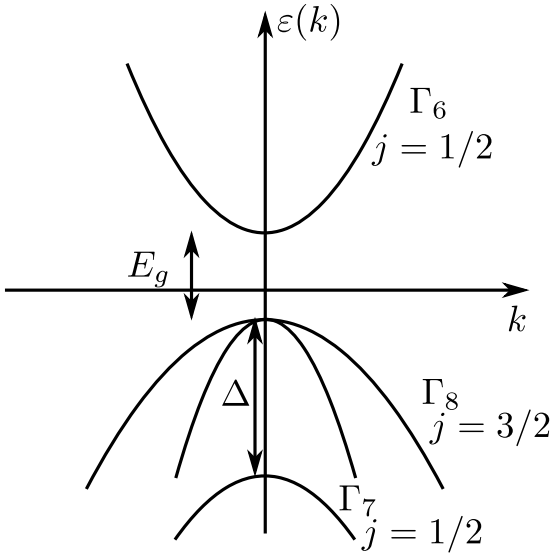

Figure 4.1: Sketch of the bandstructure considered in the Kane model. We classify the band by their irreducible representation and their total angular momentum.

respectively. We are able to rewrite the bands using Clebsch-Gordan coefficients in the following manner [49, 56]:

$$\left|\Gamma_6, \pm\frac{1}{2}\right\rangle = |S\rangle \left|\pm\frac{1}{2}\right\rangle \tag{4.13}$$

$$\left|\Gamma_8, \pm\frac{3}{2}\right\rangle = \frac{1}{\sqrt{2}}(|X\rangle \pm i\,|Y\rangle) \left|\pm\frac{1}{2}\right\rangle \tag{4.14}$$

$$\left|\Gamma_8, \pm\frac{1}{2}\right\rangle = \pm\frac{1}{\sqrt{6}}(|X\rangle \pm i\,|Y\rangle) \left|\mp\frac{1}{2}\right\rangle - \sqrt{\frac{2}{3}}\,|Z\rangle \left|\pm\frac{1}{2}\right\rangle \tag{4.15}$$

$$\left|\Gamma_7, \pm\frac{1}{2}\right\rangle = \pm\frac{1}{\sqrt{3}}(|X\rangle \pm i\,|Y\rangle) \left|\mp\frac{1}{2}\right\rangle + \frac{1}{\sqrt{3}}\,|Z\rangle \left|\pm\frac{1}{2}\right\rangle \tag{4.16}$$

As the bands we would like to consider might be quasi degenerate, we apply a canonical transformation to separate them from the others, and treat the other bands as a perturbation. The structure is similar to what we showed above with a single band. If the 8 bands correspond to the A set and the other bands correspond to the B set, we can use the variational principle [56, 119, 122] to obtain the new matrix elements as

$$\langle u_{n\mathbf{0}}|\tilde{\mathcal{H}}|u_{n'\mathbf{0}}\rangle = \langle u_{n\mathbf{0}}|\mathcal{H}|u_{n'\mathbf{0}}\rangle + \sum_{|u_{k\mathbf{0}}\rangle\in B} \frac{\langle u_{n\mathbf{0}}|\mathcal{H}|u_{k\mathbf{0}}\rangle\langle u_{k\mathbf{0}}|\mathcal{H}|u_{n'\mathbf{0}}\rangle}{E_n - E_k}, \tag{4.17}$$

where $|u_{n\mathbf{0}}\rangle$ and $|u_{n'\mathbf{0}}\rangle$ are in the A set. We can now describe the coupled the coupled

differential equations for elements of the set A as [120]

$$\sum_{n'\in A}\left(D^{ij}_{nn'}k_ik_j+\pi^i_{nn'}k_i+\frac{\hbar}{4m_0^2c^2}[(\boldsymbol{\sigma}\times\nabla V)\mathbf{p}]_{nn'}+E'_n\delta_{nn'}\right)u_{n'\mathbf{0}}=Eu_{n\mathbf{0}}, \tag{4.18}$$

where $D^{ij}_{nn'}=\frac{\hbar^2}{2m_0}\left\{\delta_{nn'}\delta_{ij}+\frac{1}{m_0}\sum_{\alpha\in B}\pi^i_{n\alpha}\pi^j_{\alpha n'}\left[\frac{1}{E_n-E_\alpha}+\frac{1}{E_{n'}-E_\alpha}\right]\right\}$ is the correction due to the remote bands. For example, if we neglect for now this correction term, we can compute the element

$$\left\langle\Gamma_6,\frac{1}{2}\middle|\tilde{\mathcal{H}}\middle|\Gamma_8,\frac{3}{2}\right\rangle=\frac{1}{\sqrt{2}}\left\langle S,\frac{1}{2}\middle|\tilde{\mathcal{H}}\middle|X+iY,\frac{1}{2}\right\rangle. \tag{4.19}$$

The SOC term $\frac{\hbar}{4m_0^2c^2}(\boldsymbol{\sigma}\times\nabla V)\cdot\mathbf{p}$ does not contribute in this case, due to symmetry. The only part of the Hamiltonian entering the computation is $\frac{\hbar}{m_0}\mathbf{k}\cdot\boldsymbol{\pi}$. The $\mathbf{k}$-dependent SOC term is much weaker compared to the first SOC term, as the electron momentum p is larger than the lattice momentum k. The second term can be therefore neglected [123]. The matrix element is then

$$\frac{1}{\sqrt{2}}\frac{\hbar}{m_0}\left\langle S,\frac{1}{2}\middle|\mathbf{k}\cdot\mathbf{p}\middle|X+iY,\frac{1}{2}\right\rangle=-\frac{1}{\sqrt{2}}P(k_x+ik_y), \tag{4.20}$$

where $P=-\frac{\hbar}{m_0}\langle S|p_x|X\rangle$ is the "Kane momentum" [123]. Note that due to symmetry, we expect that $\langle S|p_x|X\rangle=\langle S|p_y|Y\rangle=\langle S|p_z|Z\rangle$. The Kane momentum can be found in experimental measurements or from first principles computations and it describes the coupling between the conduction and the valence bands. Similarly, we can define the Kane energy as $E_P=\frac{2m_0P^2}{\hbar^2}$.

We repeat the same procedure for all the other terms contributing to the 8×8 Hamiltonian. We use the symmetries of the lattice to restrict the number of elements composing the $k\cdot p$ Hamiltonian. If we also take into account the contribution of the remote bands, we can define the dimensionless Luttinger parameters γ_1, γ_2 and γ_3 [124]. γ_1 and γ_2 split the Γ_8 at $\mathbf{k}\neq0$. γ_3 introduces anisotropies in the valence bands if $\gamma_3\neq\gamma_2$. Note that the Luttinger parameters were introduced in a model where the conduction band is considered as one of the remote bands. If we introduce the conduction band explicitly, we need to renormalize accordingly these parameters [125]. The advantage of the Luttinger parameters is that they are measureable in experiments, or calculable in first principles computations.

We are then able to write the 8×8 Kane Hamiltonian in the basis $\{|\Gamma_6,+1/2\rangle$, $|\Gamma_6,-1/2\rangle,|\Gamma_8,+3/2\rangle,|\Gamma_8,+1/2\rangle,|\Gamma_8,-1/2\rangle,|\Gamma_8,-3/2\rangle,|\Gamma_7,+1/2\rangle,|\Gamma_7,-1/2\rangle\}$, see Tab. C.8 of Ref. [49]. There are a few more terms appearing in this Hamiltonian, which were not described up to now: the coefficient C appears due to the inversion asymmetry [126],

and $B_{8v}^{\pm}$ and B_{7v} come from the second order perturbation corrections, as written in Eq. (4.17) [127].

4.1.1 $k \cdot p$ theory for heterostructures

We are now able to describe the band structure near the Γ point for a homogeneous zinc blende lattice, made of only one crystal structure. Nonetheless, it is possible to use $k \cdot p$ theory to describe more complex geometries such as heterostructures using the envelope-function theory. The idea is to consider that the heterostructure is grown along the z direction, such that k_x and k_y remain good quantum numbers. k_z is then replaced by $-i\partial_z$. This is the method developed by Burt [128, 129] and Foreman [130, 131]. More details are present in Chap. 12 of Ref. [56]. The key point is to write the wave function as

$$\psi(\mathbf{r}) = \sum_n F_n(\mathbf{r}) u_n(\mathbf{r}), \tag{4.21}$$

where $F_n(\mathbf{r})$ is the envelope function. This function should be smooth, slowly varying and continuous in the z direction. Moreover, it can be expanded in plane waves in the x and y direction:

$$F_n(\mathbf{r}) = \frac{1}{\sqrt{S}} e^{i(k_x x + k_y y)} f_n(z). \tag{4.22}$$

$u_n(\mathbf{r})$ forms a complete set of periodic functions, which are expressed over the whole heterostructure, i.e. the functions now are not only defined over one layer of the hetereostructure. At the boundary between two different material layers, we assume that the potential change is step-like, leading to $f_n(z)$ and $Df_n(z)$ being continuous at the boundary. D is the differential operator defined after integrating the differential equations of the wave function near the boundary [128, 129, 131, 132] and ensures the continuity of the probability current. We will see later an explicit example of such a differential operator.

We are able to apply $k \cdot p$ theory to solve the multiband system [132]. We get a set of coupled differential equations, which is very similar to Eq. (4.18),

$$\sum_{n' \in A} \left(k_i D^{ij}_{nn'} k_j + \pi^i_{nn'} k_i + \frac{\hbar}{4m_0^2 c^2} [(\boldsymbol{\sigma} \times \nabla V)\mathbf{p}]_{nn'} + E'_n(z)\delta_{nn'} \right) f_{n'}(z) = E f_n(z). \tag{4.23}$$

When we generalize Foreman model [130] to include also the conduction band, we get a full 8×8 Hamiltonian for a heterostructure grown along the z direction [65, 132, 133], in the basis $\{|\Gamma_6, +1/2\rangle, |\Gamma_6, -1/2\rangle, |\Gamma_8, +3/2\rangle, |\Gamma_8, +1/2\rangle, |\Gamma_8, -1/2\rangle, |\Gamma_8, -3/2\rangle, |\Gamma_7, +1/2\rangle, |\Gamma_7, -1/2\rangle\}$. This Hamiltonian is very close to the Kane Hamiltonian and takes the

following form

$$\mathcal{H} = \begin{pmatrix} T & 0 & -\frac{1}{\sqrt{2}}Pk_+ & \sqrt{\frac{2}{3}}Pk_z & \frac{1}{\sqrt{6}}Pk_- & 0 & -\frac{1}{\sqrt{3}}Pk_z & -\frac{1}{\sqrt{3}}Pk_- \\ 0 & T & 0 & -\frac{1}{\sqrt{6}}Pk_+ & \sqrt{\frac{2}{3}}Pk_z & \frac{1}{\sqrt{2}}Pk_- & -\frac{1}{\sqrt{3}}Pk_+ & \frac{1}{\sqrt{3}}Pk_z \\ -\frac{1}{\sqrt{2}}k_-P & 0 & U+V & -\bar{S}_- & R & 0 & \frac{1}{\sqrt{2}}\bar{S}_- & -\sqrt{2}R \\ \sqrt{\frac{2}{3}}k_zP & -\frac{1}{\sqrt{6}}k_-P & -\bar{S}_-^\dagger & U-V & C & R & \sqrt{2}V & -\sqrt{\frac{3}{2}}\tilde{S}_- \\ -\frac{1}{\sqrt{6}}k_-P & \sqrt{\frac{2}{3}}k_zP & R^\dagger & C^\dagger & U-V & \bar{S}_+^\dagger & -\sqrt{\frac{3}{2}}\tilde{S}_+ & -\sqrt{2}V \\ 0 & \frac{1}{\sqrt{2}}k_+P & 0 & R^\dagger & \bar{S}_+ & U+V & \sqrt{2}R^\dagger & \frac{1}{\sqrt{2}}\bar{S}_+ \\ -\frac{1}{\sqrt{3}}k_zP & -\frac{1}{\sqrt{3}}k_-P & \frac{1}{\sqrt{2}}\bar{S}_-^\dagger & \sqrt{2}V & -\sqrt{\frac{3}{2}}\tilde{S}_+^\dagger & \sqrt{2}R & U-\Delta & C \\ -\frac{1}{\sqrt{3}}k_+P & \frac{1}{\sqrt{3}}k_zP & -\sqrt{2}R^\dagger & -\sqrt{\frac{3}{2}}\tilde{S}_-^\dagger & -\sqrt{2}V & \frac{1}{\sqrt{2}}\bar{S}_+^\dagger & C^\dagger & U-\Delta \end{pmatrix}, \tag{4.24}$$

where $k_\parallel^2 = k_x^2 + k_y^2$, $k_\pm = k_x \pm ik_y$ and $k_z = -i\partial_z$ and P is the Kane momentum as before. Note the ordering of the momentum operators, which ensures the hermiticity of the Hamiltonian. The different terms of the Hamiltonian are

$$\begin{aligned} T &= E_c + \frac{\hbar^2}{2m_0}\left(\gamma_0' k_\parallel^2 + k_z\gamma_0' k_z\right), & U &= E_v - \frac{\hbar^2}{2m_0}\left(\gamma_1' k_\parallel^2 + k_z\gamma_1' k_z\right), \\ V &= -\frac{\hbar^2}{2m_0}\left(\gamma_2' k_\parallel^2 - 2k_z\gamma_2' k_z\right), & R &= -\frac{\sqrt{3}\hbar^2}{4m_0}\left[(\gamma_3' - \gamma_2')k_+^2 - (\gamma_3' + \gamma_2')k_-^2\right], \\ \bar{S}_\pm &= -\frac{\sqrt{3}\hbar^2}{2m_0}k_\pm\left(\{\gamma_3', k_z\} + [\kappa', k_z]\right), & \tilde{S}_\pm &= -\frac{\sqrt{3}\hbar^2}{2m_0}k_\pm\left(\{\gamma_3', k_z\} - \frac{1}{3}[\kappa', k_z]\right), \\ & & C &= \frac{\hbar^2}{m_0}k_-[\kappa', k_z], \end{aligned} \tag{4.25}$$

where $[A, B] = AB - BA$ and $\{A, B\} = AB + BA$. As it was mentioned before, the Luttinger parameters (as well as κ and the mass of the conduction band m_c) need to be renormalized. They become now [123, 125]

$$\begin{aligned} \gamma_0' &= \frac{m_0}{m_c} - \frac{E_P}{E_g}\frac{E_g + 2/3\Delta}{E_g + \Delta} & \gamma_1' &= \gamma_1 - \frac{1}{3}\frac{E_P}{E_g} \\ \gamma_2' &= \gamma_2 - \frac{1}{6}\frac{E_P}{E_g} & \gamma_3' &= \gamma_3 - \frac{1}{6}\frac{E_P}{E_g} \\ & & \kappa' &= \kappa - \frac{1}{6}\frac{E_P}{E_g} \end{aligned} \tag{4.26}$$

Note that these parameters are all position dependent, as they are material dependent.

The differential operator D is

$$D = \begin{pmatrix} t & 0 & 0 & 0 & 0 & 0 & 0 & 0 \\ 0 & t & 0 & 0 & 0 & 0 & 0 & 0 \\ 0 & 0 & u+v & -\bar{s}_- & 0 & 0 & \frac{1}{\sqrt{2}}\bar{s}_- & 0 \\ \sqrt{\frac{2}{3}}P & 0 & -\bar{s}'_+ & u-v & c & 0 & \sqrt{2}v & -\sqrt{\frac{3}{2}}\tilde{s}_- \\ 0 & \sqrt{\frac{2}{3}}P & 0 & c^* & u-v & \bar{s}'_- & -\sqrt{\frac{3}{2}}\tilde{s}_+ & -\sqrt{2}v \\ 0 & 0 & 0 & 0 & \bar{s}_+ & u+v & 0 & \frac{1}{\sqrt{2}}\bar{s}_+ \\ -\frac{1}{\sqrt{3}}P & & \frac{1}{\sqrt{2}}\bar{s}'_+ & \sqrt{2}v & -\sqrt{\frac{3}{2}}\tilde{s}'_- & 0 & u & c \\ 0 & \frac{1}{\sqrt{3}}P & 0 & -\sqrt{\frac{3}{2}}\tilde{s}'_+ & -\sqrt{2}v & \frac{1}{\sqrt{2}}\bar{s}'_- & c^* & u \end{pmatrix}, \quad (4.27)$$

such that Df is continuous across the interface [132]. The parameters are now defined as

$$\begin{aligned} t &= -\frac{\hbar^2}{2m_0}\gamma'_0\partial_z, & u &= \frac{\hbar^2}{2m_0}\gamma'_1\partial_z, & v &= \frac{\hbar^2}{m_0}\gamma'_2\partial_z, \\ \bar{s}_\pm &= \frac{\sqrt{3}\hbar^2}{2m_0}ik_\pm\left(\gamma'_3-\kappa'\right), & & & \bar{s}'_\pm &= \frac{\sqrt{3}\hbar^2}{2m_0}ik_\pm\left(\gamma'_3+\kappa'\right), \\ \tilde{s}_\pm &= \frac{\sqrt{3}\hbar^2}{2m_0}ik_\pm\left(\gamma'_3+\frac{\kappa'}{3}\right) & & & \tilde{s}'_\pm &= \frac{\sqrt{3}\hbar^2}{2m_0}ik_\pm\left(\gamma'_3-\frac{\kappa'}{3}\right), \\ & & c &= \frac{\hbar^2}{m_0}ik_-\kappa'. & & \end{aligned} \quad (4.28)$$

We have now enough understanding about the origins of the $k.p$ Hamiltonian presented in Eq. (4.24) to apply it to our heterostructure.

4.2 Effective model for InAs/GaSb heterostructures

We will mainly use the same technique as described in [8]. We want to create a two-dimensional effective model to describe the heterostructure. We will first neglect the split-off valence band, as it lies far enough from the other bands at $\mathbf{k} = \mathbf{0}$ and thus has little influence on the remaining bands [65]. We will use the same layered system as presented in Fig. 1.10 and repeated in Fig. 4.2. The structure is such that the InAs and the GaSb layers are sandwiched between two layers of AlSb. We consider the data presented in [65], in particular that the layer of InAs is 12.5 nm-thick ($d_1 = 12.5$ nm) and the layer of GaSb is 5 nm-thick ($d_2 = 5$ nm). The different material-dependent constants are presented in Tab. 4.1, and are taken from Refs. [65, 134, 135]. We take into account the valence offsets between the layers such that $E_v^{AlSb} - E_v^{InAs} = 0.18$ eV, $E_v^{InAs} - E_v^{GaSb} = -0.56$ eV, and

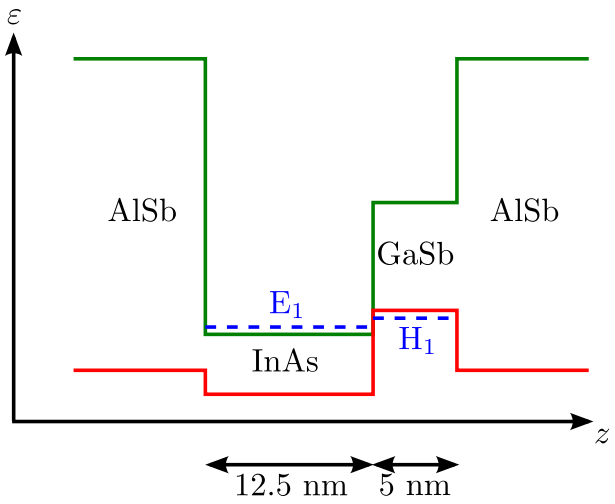

Figure 4.2: Band structure in the z-direction. The conduction band is indicated in each layer in green and the valence band is indicated in red. In dashed (blue), the effective inverted bands representing electron-like and hole-like behavior near the Γ-point.

	E_g [eV]	Δ [eV]	E_P [eV]	m_c/m_0	γ_1	γ_2	γ_3	κ
InAs	0.41	0.38	22.2	0.024	19.67	8.37	9.29	7.68
GaSb	0.8128	0.752	22.4	0.042	11.80	4.03	5.26	3.18
AlSb	2.32	0.75	18.7	0.18	4.15	1.01	1.75	0.31

Table 4.1: Values of the parameters for the different materials entering the Hamiltonian presented in Eq. (4.24). Data taken from Refs. [134, 135].

$E_v^{GaSb} - E_v^{AlSb} = 0.38$ eV [65, 134].

We will first start by considering the case $k_x = k_y = 0$. We will introduce nonzero k_x and k_y later using perturbation theory. The Hamiltonian in Eq. (4.24) becomes

$$\mathcal{H}_0 = \begin{pmatrix} T & 0 & 0 & -i\sqrt{\frac{2}{3}}P(z)\partial_z & 0 & 0 \\ 0 & T & 0 & 0 & -i\sqrt{\frac{2}{3}}P(z)\partial_z & 0 \\ 0 & 0 & U+V & 0 & 0 & 0 \\ -i\sqrt{\frac{2}{3}}\partial_z P(z) & 0 & 0 & U-V & 0 & 0 \\ 0 & -i\sqrt{\frac{2}{3}}\partial_z P(z) & 0 & 0 & U-V & 0 \\ 0 & 0 & 0 & 0 & 0 & U+V \end{pmatrix}. \tag{4.29}$$

We can rewrite the diagonal terms as

$$T = E_c(z) - \frac{\hbar^2}{2m_0}\partial_z\gamma_0(z)\partial_z, \qquad U = E_v(z) + \frac{\hbar^2}{2m_0}\partial_z\gamma_1(z)\partial_z, \qquad V = -2\frac{\hbar^2}{2m_0}\partial_z\gamma_2(z)\partial_z. \tag{4.30}$$

Moreover if we reorder the above Hamiltonian by the sign of the band spin, we obtain two blocks related by time-reversal symmetry. As the two blocks are totally decoupled, we can focus without loss of generality on the block with the states defined with a positive spin. We call this block "+". We also need to set the Fermi energy: $\varepsilon_F = 0$, such that $E_v^{InAs} = -0.41$ eV. Using the ansatz presented in Eq. (4.22), we can write the wave function of the block as

$$\Psi(k_x, k_y, z) = e^{i(k_x x + k_y y)} \begin{pmatrix} f_1(z) \\ f_3(z) \\ f_4(z) \end{pmatrix}. \tag{4.31}$$

We get the following set of equations to solve

$$\begin{pmatrix} T & 0 & -i\sqrt{\frac{2}{3}}P(z)\partial_z \\ 0 & U+V & 0 \\ -i\sqrt{\frac{2}{3}}\partial_z P(z) & 0 & U-V \end{pmatrix} \begin{pmatrix} f_1(z) \\ f_3(z) \\ f_4(z) \end{pmatrix} = E \begin{pmatrix} f_1(z) \\ f_3(z) \\ f_4(z) \end{pmatrix}. \tag{4.32}$$

Applying the boundary conditions, we also need that

$$\begin{pmatrix} -\frac{\hbar^2}{2m_0}\gamma_0'(z)\partial_z & 0 & 0 \\ 0 & \frac{\hbar^2}{2m_0}\left[\gamma_1'(z) - 2\gamma_2'(z)\right]\partial_z & 0 \\ -i\sqrt{\frac{2}{3}}P(z) & 0 & \frac{\hbar^2}{2m_0}\left[\gamma_1'(z) + 2\gamma_2'(z)\right]\partial_z \end{pmatrix} \begin{pmatrix} f_1(z) \\ f_3(z) \\ f_4(z) \end{pmatrix} \tag{4.33}$$

must be continuous at the boundary of each layer. We are now fully equipped to find the solutions for this asymmetric potential well.

From the Hamiltonian in Eq. (4.32), we notice that the heavy hole band is decoupled from the other bands. In our effective model, it will lead to a hole band that we will call $H1$. From the Hamiltonian, we obtain the following differential equation:

$$\left(E_v(z) + \frac{\hbar^2}{2m_0}\partial_z\left[\gamma_1'(z) - 2\gamma_2'(z)\right]\partial_z\right) f_3(z) = E f_3(z). \tag{4.34}$$

Inside each layer, all the material-dependent parameters are constant in each material, they are then not affected by the derivative. We make the following ansatz for this band

$$f_3(z) = \begin{cases} Ae^{\tilde{\alpha}z} & z \leq -d_1 \\ B\cosh(\tilde{\beta}z) + C\sinh(\tilde{\beta}z) & -d_1 \leq z \leq 0\,\text{nm} \\ D\cos(\tilde{\delta}z) + F\sin(\tilde{\delta}z) & 0\,\text{nm} \leq z \leq d_2 \\ Ge^{-\tilde{\alpha}z} & z \geq d_2 \end{cases}, \tag{4.35}$$

where $\tilde{\alpha} = \frac{\sqrt{2m_0}}{\hbar}\sqrt{\frac{E-E_v^{AlSb}}{\gamma_1'^{AlSb}-2\gamma_2'^{AlSb}}}$, $\tilde{\beta} = \frac{\sqrt{2m_0}}{\hbar}\sqrt{\frac{E-E_v^{InAs}}{\gamma_1'^{InAs}-2\gamma_2'^{InAs}}}$, and $\tilde{\delta} = \frac{\sqrt{2m_0}}{\hbar}\sqrt{\frac{E_v^{GaSb}-E}{\gamma_1'^{GaSb}-2\gamma_2'^{GaSb}}}$. This ansatz must respect the boundary conditions, such that

$$\begin{aligned} &Ae^{-\tilde{\alpha}d_1} = B\cosh(\tilde{\beta}d_1) - C\sinh(\tilde{\beta}d_1), \\ &B = D, \\ &D\cos(\tilde{\delta}d_2) + F\sin(\tilde{\delta}d_2) = Ge^{-\tilde{\alpha}d_2}, \end{aligned} \tag{4.36}$$

$$\begin{aligned} &\tilde{\alpha}(\gamma_1'^{AlSb} - 2\gamma_2'^{AlSb})Ae^{-\tilde{\alpha}d_1} = \tilde{\beta}(\gamma_1'^{InAs} - 2\gamma_2'^{InAs})(-B\sinh(\tilde{\beta}d_1) + C\cosh(\tilde{\beta}d_1)), \\ &\tilde{\beta}(\gamma_1'^{InAs} - 2\gamma_2'^{InAs})C = \tilde{\delta}(\gamma_1'^{GaSb} - 2\gamma_2'^{GaSb})F, \\ &\tilde{\delta}(\gamma_1'^{GaSb} - 2\gamma_2'^{GaSb})(-D\sin(\tilde{\delta}d_2) + F\cos(\tilde{\delta}d_2)) = -\tilde{\alpha}(\gamma_1'^{AlSb} - 2\gamma_2'^{AlSb})Ge^{-\tilde{\alpha}d_2}. \end{aligned} \tag{4.37}$$

Solving these linear equations enables us to find an implicit equation for the energy of the hole band. This equation is

$$\frac{\tilde{\beta}'}{\tilde{\delta}'}\frac{\tilde{\alpha}' + \tilde{\beta}'\tanh(\tilde{\beta}d_1)}{\tilde{\alpha}'\tanh(\tilde{\beta}d_1) + \tilde{\beta}'} = \frac{\tilde{\delta}'\tan(\tilde{\delta}d_2) - \tilde{\alpha}'}{\tilde{\alpha}'\tan(\tilde{\delta}d_2) + \tilde{\delta}'}, \tag{4.38}$$

where $\tilde{\alpha}' = \tilde{\alpha}(\gamma_1'^{AlSb} - 2\gamma_2'^{AlSb})$, $\tilde{\beta}' = \tilde{\beta}(\gamma_1'^{InAs} - 2\gamma_2'^{InAs})$, and $\tilde{\delta}' = \tilde{\delta}(\gamma_1'^{GaSb} - 2\gamma_2'^{GaSb})$. If we numerically solve this implicit equation with the data given in Tab. 4.1 and the widths $d_1 = 12.5$ nm and $d_2 = 5$ nm, we are able to find the energy of the hole band at

$$E_{H1} = 0.1154\,\text{eV}. \tag{4.39}$$

With the energy of the hole band, we are able to evaluate all the constants entering in the wave function. If we take into account its normalization, we are able to plot it in the z direction. The result is shown in Fig. 4.3. We observe that the wave function is well localized in the GaSb layer. It is exponentially suppressed when it penetrates in the neighboring layers. Note that this is consistent with what was already observed in Refs. [134, 136, 137].

We can repeat the same procedure for the equations for $f_1(z)$ and $f_4(z)$. This time, we note the coupling of the electron band and the light hole band. The effective band in the z direction will then mostly be an electron band or a light-hole band. We obtain the following set of differential equations in each layer

$$\begin{pmatrix} E_c(z) - \frac{\hbar^2}{2m_0}\gamma_0'(z)\partial_z^2 & -i\sqrt{\frac{2}{3}}P(z)\partial_z \\ -i\sqrt{\frac{2}{3}}P(z)\partial_z & E_v(z) + \frac{\hbar^2}{2m_0}\left[\gamma_1'(z) + \gamma_2'(z)\right]\partial_z^2 \end{pmatrix} \begin{pmatrix} f_1(z) \\ f_4(z) \end{pmatrix} = E \begin{pmatrix} f_1(z) \\ f_4(z) \end{pmatrix}. \tag{4.40}$$

To solve these differential equations, we will use the trick defined in Ref. [131] as explained below. If we use the data given in Tab. 4.1, we find that γ_0' can even be negative. However,

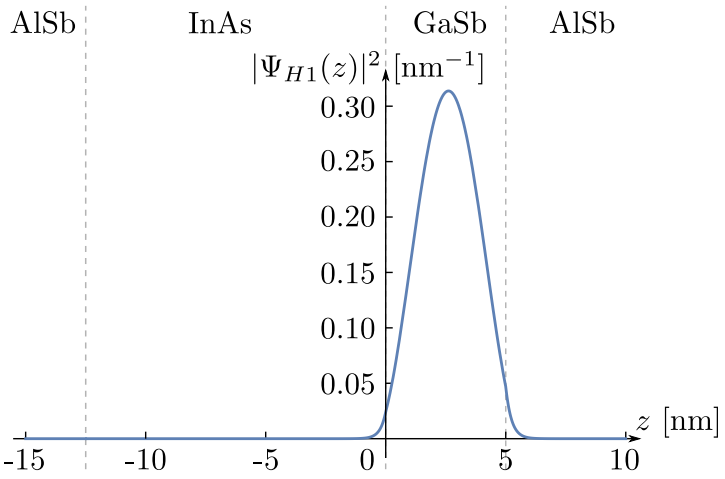

Figure 4.3: Wave function in the z direction for the $H1$ band. The dashed (grey) lines indicate the boundaries of the layers.

if we set $\gamma_0' = 1$, it enables us to avoid unphysical solutions, but does not change band structure near $\mathbf{k} = 0$ [65, 131]. The consequence is that the value of P needs to be renormalized by inverting the equation of γ_0' in Eq. (4.26). We have then

$$E_P = \left(\frac{m_0}{m_c} - \gamma_0'\right) \frac{E_g(E_g + \Delta)}{E_g + 2/3\Delta}, \tag{4.41}$$

which changes the values of the other Luttinger parameters in Eq. (4.26) accordingly. If we neglect for now the term with γ_0', we are then able to express $f_1(z)$ as function of $f_4(z)$, such that

$$f_1(z) = \frac{i}{E_c - E}\sqrt{\frac{2}{3}} P \partial_z f_4(z) = i\sqrt{\frac{2}{3}}\sqrt{\frac{\hbar^2}{2m_0}}\frac{\sqrt{E_P}}{E_c - E}\partial_z f_4(z). \tag{4.42}$$

The light hole band differential equation becomes

$$\left\{E_v(z) - E + \frac{\hbar^2}{2m_0}\left[\gamma_1'(z) + \gamma_2'(z) + \frac{2E_P(z)}{3(E_c(z) - E)}\right]\partial_z^2\right\} f_4(z) = 0. \tag{4.43}$$

Using this technique, $f_1(z)$ is no longer continuous at the interface, as pointed out in Refs. [128, 131]. We can propose an ansatz for the wave function and check the boundary conditions for $f_4(z)$. Once we know the numerical solution of $f_4(z)$, we can get $f_1(z)$, by using Eq. (4.42). The ansatz is then

$$f_4(z) = \begin{cases} A_2 e^{\alpha z} & z \leq -d_1 \\ B_2\cos(\beta z) + C_2\sin(\beta z) & -d_1 \leq z \leq 0\,\text{nm} \\ D_2\cos(\delta z) + F_2\sin(\delta z) & 0\,\text{nm} \leq z \leq d_2 \\ G_2 e^{-\alpha z} & z \geq d_2 \end{cases}, \tag{4.44}$$

where now the coefficents are

$$\begin{aligned}
\alpha &= \sqrt{\frac{2m_0}{\hbar^2}}\sqrt{\frac{3(E_c^{AlSb}-E)(E-E_v^{AlSb})}{3(E_c^{AlSb}-E)(\gamma_1'^{AlSb}+2\gamma_2'^{AlSb})+2E_P^{AlSb}}},\\
\beta &= \sqrt{\frac{2m_0}{\hbar^2}}\sqrt{\frac{3(E-E_c^{InAs})(E-E_v^{InAs})}{3(E_c^{InAs}-E)(\gamma_1'^{InAs}+2\gamma_2'^{InAs})+2E_P^{InAs}}},\\
\delta &= \sqrt{\frac{2m_0}{\hbar^2}}\sqrt{\frac{3(E_c^{GaSb}-E)(E_v^{GaSb}-E)}{3(E_c^{GaSb}-E)(\gamma_1'^{GaSb}+2\gamma_2'^{GaSb})+2E_P^{GaSb}}}.
\end{aligned} \tag{4.45}$$

The boundary conditions are then defined such that for $f_4(z)$, we have

$$\begin{aligned}
A_2e^{-\alpha d_1} &= B_2\cos(\beta d_1) - C_2\sin(\beta d_1),\\
B_2 &= D_2,\\
D_2\cos(\delta d_2) + F_2\sin(\delta d_2) &= G_2e^{-\alpha d_2},
\end{aligned} \tag{4.46}$$

$$\begin{aligned}
\alpha' A_2e^{-\alpha d_1} &= \beta'\left(B_2\sin(\beta d_1) + C_2\cos(\beta d_1)\right),\\
\beta' C_2 &= \delta' F_2,\\
\delta'\left(-D_2\sin(\delta d_2) + F_2\cos(\delta d_2)\right) &= -\alpha' G_2e^{-\alpha d_2},
\end{aligned} \tag{4.47}$$

where $\alpha' = \left[\gamma_1'^{AlSb} + 2\gamma_2'^{AlSb} + \frac{2E_P^{AlSb}}{3(E_c^{AlSb}-E)}\right]\alpha$, $\beta' = \left[\gamma_1'^{InAs} + 2\gamma_2'^{InAs} + \frac{2E_P^{InAs}}{3(E_c^{InAs}-E)}\right]\beta$ and $\delta' = \left[\gamma_1'^{GaSb} + 2\gamma_2'^{GaSb} + \frac{2E_P^{GaSb}}{3(E_c^{GaSb}-E)}\right]\delta$. We find again an implicit equation in order to get the energy

$$\frac{\beta'}{\delta'}\frac{\alpha' - \beta'\tan(\beta d_1)}{\beta' + \alpha'\tan(\beta d_1)} = \frac{\delta'\tan(\delta d_2) - \alpha'}{\alpha'\tan(\delta d_2) + \delta'}. \tag{4.48}$$

If we solve numerically this equation, we get the following energy

$$E_{E1} = 0.0647\,\text{eV}. \tag{4.49}$$

We evaluate all the coefficients entering in the wave function computation using the data presented in Tab. 4.1 and by using Eq. (4.42), we get the second component of the wave function. Once it is renormalized, the wave function in the z-direction is shown in Fig. 4.4. We find this time that even if the wave function is mostly localized in the InAs layer, there is still a non-negligible component in the GaSb layer due to the interband coupling. As most of the wave function is in the InAs layer, it will behave mostly as an electron band, so we call it $E1$. We plot the two different components of the wave function in Fig. 4.4. We notice that the light hole component (f_4) is indeed located mostly in the GaSb layer, whereas the electron component (f_1) is mostly located in the InAs layer. Moreover, the latter has the largest weight on the wave function. It reinforces the electron-like behavior

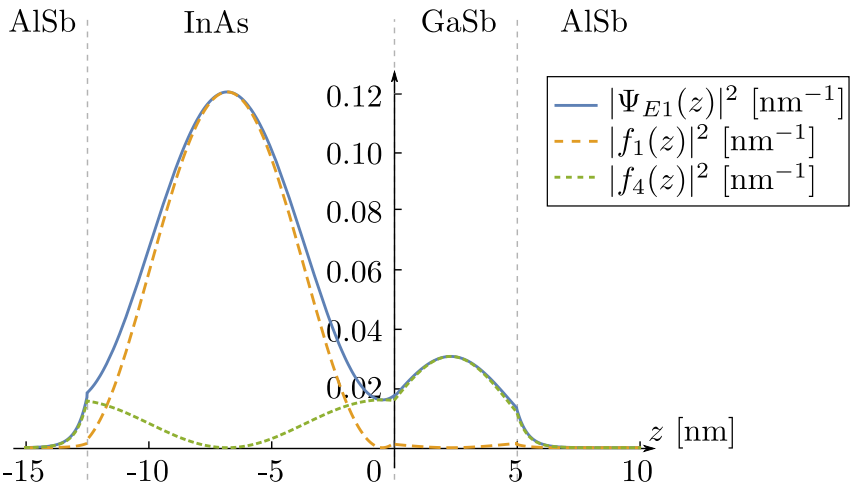

Figure 4.4: Wave function in the z direction for the $E1$ band. The dashed (grey) lines indicate the boundaries of the layers.

of the band. The wave function and its components are again consistent with the results published in Refs. [134, 136, 137]. For the "−" block, we get the same wave functions as presented above.

We now introduce perturbatively the remaining elements. The perturbation Hamiltonian is defined as

$$\mathcal{H}_1 = \begin{pmatrix} T_1 & 0 & -\frac{1}{\sqrt{2}}Pk_+ & 0 & \frac{1}{\sqrt{6}}Pk_- & 0 \\ 0 & T_1 & 0 & -\frac{1}{\sqrt{6}}Pk_+ & 0 & \frac{1}{\sqrt{2}}Pk_- \\ -\frac{1}{\sqrt{2}}Pk_- & 0 & U_1+V_1 & -S_- & R & 0 \\ 0 & -\frac{1}{\sqrt{6}}Pk_- & -S_-^\dagger & U_1-V_1 & C & R \\ \frac{1}{\sqrt{6}}Pk_+ & 0 & R^\dagger & C^\dagger & U_1-V_1 & S_+^\dagger \\ 0 & \frac{1}{\sqrt{2}}Pk_+ & 0 & R^\dagger & S_+ & U_1+V_1 \end{pmatrix}, \tag{4.50}$$

where the parameters are $T_1 = \frac{\hbar^2}{2m_0}\gamma_0' k_\parallel^2$, $U_1 = -\frac{\hbar^2}{2m_0}\gamma_1' k_\parallel^2$, and $V_1 = -\frac{\hbar^2}{2m_0}\gamma_2' k_\parallel^2$. As well as computing the energy of the $H1$ and $E1$ bands, we obtain other bound states at lower energy, namely a second hole band $H2$ and a band with predominantly light hole band characteristics $L1$. These additional bands are consistent with the results published in Ref. [134]. As they are located at lower energies and as we compute only the first order perturbation terms, we neglect them in our effective model. If we want to compute higher order terms, we also need to take into account the $H1$ and $L1$ energy levels, and we would apply a canonical transformation as in the previous section [16, 49]. The canonical transformation would enable us decouple the $E1$ and $H1$ bands from the $H2$ and $L1$ bands. To get the elements of the effective 4×4 Hamiltonian, we need to perform the

following integrals

$$\mathcal{H}_{ij}^{eff} = E_i\delta_{i,j} + \int_{-\infty}^{\infty} dz \sum_{\alpha\beta}^{6} \left\langle \Psi_i^{\alpha}(k_x,k_y,z)|\mathcal{H}_{1,\alpha\beta}|\Psi_j^{\beta}(k_x,k_y,z)\right\rangle \tag{4.51}$$

where $E_1 = E_3 = E_{E1}$ and $E_2 = E_4 = E_{H1}$. We will show one term of the matrix as an example to make the procedure explicit. The other terms are obtained in the same way. We compute $\mathcal{H}_{14}^{eff}$:

$$\begin{aligned}
\mathcal{H}_{14}^{eff} &= \int_{-\infty}^{\infty} dz \sum_{\alpha\beta}^{6} \left\langle \Psi_1^{\alpha}(k_x,k_y,z)|\mathcal{H}_{1,\alpha\beta}|\Psi_4^{\beta}(k_x,k_y,z)\right\rangle \\
&= \int_{-\infty}^{\infty} dz f_4^*(z) R f_6(z) \\
&= -\frac{\sqrt{3}\hbar^2}{4m_0}k_+^2 \int_{-\infty}^{\infty} dz f_4^*(z)\left[\gamma_3'(z) - \gamma_2'(z)\right] f_6(z) \\
&\quad + \frac{\sqrt{3}\hbar^2}{4m_0}k_-^2 \int_{-\infty}^{\infty} dz f_4^*(z)\left[\gamma_3'(z) + \gamma_2'(z)\right] f_6(z).
\end{aligned} \tag{4.52}$$

We are able to evaluate all the terms of the Hamiltonian, by computing all the remaining integrals. The effective Hamiltonian can then be written as

$$H_0^{eff} = \sum_{\mathbf{k}} \Phi^{\dagger}(\mathbf{k})\mathcal{H}_0^{eff}(\mathbf{k})\Phi(\mathbf{k}), \tag{4.53}$$

where $\Phi(\mathbf{k}) = (E1_+(\mathbf{k}), H1_+(\mathbf{k}), E1_-(\mathbf{k}), H1_-(\mathbf{k}))^T$. The Bloch matrix is

$$\begin{aligned}
&\mathcal{H}_0^{eff}(\mathbf{k}) \\
&= \begin{pmatrix}
\varepsilon(\mathbf{k}) + \mathcal{M}(\mathbf{k}) & Ak_+ & iTk_- & -i(R_1k_+^2 + R_2k_-^2) \\
Ak_- & \varepsilon(\mathbf{k}) - \mathcal{M}(\mathbf{k}) & i(R_1k_+^2 + R_2k_-^2) & 0 \\
-iTk_+ & -i(R_1k_-^2 + R_2k_+^2) & \varepsilon(\mathbf{k}) + \mathcal{M}(\mathbf{k}) & -Ak_- \\
i(R_1k_-^2 + R_2k_+^2) & 0 & -Ak_+ & \varepsilon(\mathbf{k}) - \mathcal{M}(\mathbf{k})
\end{pmatrix},
\end{aligned} \tag{4.54}$$

where $\varepsilon(\mathbf{k}) = C - Dk^2$ and $\mathcal{M}(\mathbf{k}) = M - Bk^2$. All the parameters are given in Tab. 4.2. However, using the literature values stated in Tab. 4.1, the value for R_1 becomes too large, which leads to a phase transition to a trivial insulator. As we are interested in the effect of SOC in the topological phase, we decide therefore to choose a smaller value for R_1, which enables us to remain in the nontrivial phase. In the end, we recover the BHZ Hamiltonian [8], this time with a Rashba term T and some anisotropic terms R_1 and R_2. Our results are consistent with previous results obtained in Refs. [65, 137–139]. All these

A [eV nm]	B [eV nm^2]	C [eV]	D [eV nm^2]	M [eV]
0.0081	-0.0434	0.0901	0.0428	-0.0254
	R_1(*) [eV nm^2]	R_2 [eV nm^2]	T [eV nm]	
	0.0044	-0.0034	0.004	

Table 4.2: Values of the parameters for the effective Hamiltonian presented in Eq. (4.54). They are evaluated when the layer of InAs is $d_1 = 12.5$ nm and the layer of GaSb is $d_2 = 5$ nm. (*) R_1 is not the numerical value extracted from the integral – see main text.

references noticed some anisotropies in the band structure, but that it kept a four-fold symmetry. We would therefore like to understand the effect of the anisotropy on the edge states. The first step is to rotate the lattice by an angle θ in the k_x, k_y plane, such that $\tilde{k}_x = \cos(\theta)k_x - \sin(\theta)k_y$ and $\tilde{k}_y = \sin(\theta)k_x + \cos(\theta)k_y$. If we set $\theta = \pi/4$, the effective Hamiltonian can now be written as

$$H^{eff}_{\pi/4} = \sum_{\tilde{\mathbf{k}}} \Phi^\dagger(\tilde{\mathbf{k}}) \mathcal{H}^{eff}_{\pi/4}(\tilde{\mathbf{k}}) \Phi(\tilde{\mathbf{k}}), \tag{4.55}$$

where $\Phi(\tilde{\mathbf{k}}) = (E1_+(\tilde{\mathbf{k}}), H1_+(\tilde{\mathbf{k}}), E1_-(\tilde{\mathbf{k}}), H1_-(\tilde{\mathbf{k}}))^T$. The Bloch matrix is now

$$\mathcal{H}^{eff}_{\pi/4}(\tilde{\mathbf{k}}) = \begin{pmatrix} \varepsilon(\tilde{\mathbf{k}}) + \mathcal{M}(\tilde{\mathbf{k}}) & Ae^{-i\pi/4}\tilde{k}_+ & iTe^{i\pi/4}\tilde{k}_- & -(R_1\tilde{k}_+^2 - R_2\tilde{k}_-^2) \\ Ae^{i\pi/4}\tilde{k}_- & \varepsilon(\tilde{\mathbf{k}}) - \mathcal{M}(\tilde{\mathbf{k}}) & (R_1\tilde{k}_+^2 - R_2\tilde{k}_-^2) & 0 \\ -iTe^{-i\pi/4}\tilde{k}_+ & (R_1\tilde{k}_-^2 - R_2\tilde{k}_+^2) & \varepsilon(\tilde{\mathbf{k}}) + \mathcal{M}(\tilde{\mathbf{k}}) & -Ae^{i\pi/4}\tilde{k}_- \\ -(R_1\tilde{k}_-^2 - R_2\tilde{k}_+^2) & 0 & -Ae^{-i\pi/4}\tilde{k}_+ & \varepsilon(\tilde{\mathbf{k}}) - \mathcal{M}(\tilde{\mathbf{k}}) \end{pmatrix}, \tag{4.56}$$

where $\varepsilon(\tilde{\mathbf{k}}) = C - D\tilde{k}^2$ and $\mathcal{M}(\tilde{\mathbf{k}}) = M - B\tilde{k}^2$. We can observe that the terms which are responsible for changing the bandstructure are the anisotropic ones.

4.3 Spin texture for InAs/GaSb heterostructures

We want to extract the spin texture from our effective model in Eq. (4.54) or in Eq. (4.56), so we need to regularize it over a square lattice. Some anisotropic terms, as well as a Rashba SOC, appear in our effective model and transform the band structure. The band structure is also influenced by the crystallographic direction of measurement, but keeps a four-fold rotation symmetry [65, 138, 139]. We would like then to see if this also affects the spin texture. We use two orientations: either if the nanoribbon is in the x or y direction or if it is rotated by $\pi/4$.

If we start with the system oriented in the x or y direction, we regularize our continuous model to a lattice model such that $k_{x,y} \approx \sin(ak_{x,y})/a$ and $k^2_{x,y} \approx (2 - 2\cos(ak_{x,y}))/a^2$,

where a is the lattice spacing ($a \simeq 0.61$ nm [134]). We obtain the effective Bloch matrix

$$\tilde{H}_0^{eff}(\mathbf{k}) = \begin{pmatrix} \tilde{\varepsilon}(\mathbf{k}) + \tilde{\mathcal{M}}(\mathbf{k}) & A(\mathbf{k}) & T(\mathbf{k}) & iR(\mathbf{k}) \\ A^*(\mathbf{k}) & \tilde{\varepsilon}(\mathbf{k}) - \tilde{\mathcal{M}}(\mathbf{k}) & -iR(\mathbf{k}) & 0 \\ T^*(\mathbf{k}) & iR^*(\mathbf{k}) & \tilde{\varepsilon}(\mathbf{k}) + \tilde{\mathcal{M}}(\mathbf{k}) & -A^*(\mathbf{k}) \\ -iR^*(\mathbf{k}) & 0 & -A(\mathbf{k}) & \tilde{\varepsilon}(\mathbf{k}) - \tilde{\mathcal{M}}(\mathbf{k}) \end{pmatrix}. \tag{4.57}$$

The different terms entering in the Hamiltonian are

$$\begin{aligned} \tilde{\varepsilon}(\mathbf{k}) =& C - \frac{2D}{a^2}[2 - \cos(ak_x) - \cos(ak_y)], \\ \tilde{\mathcal{M}}(\mathbf{k}) =& M - \frac{2B}{a^2}[2 - \cos(ak_x) - \cos(ak_y)], \\ A(\mathbf{k}) =& \frac{A}{a}(\sin(ak_x) + i\sin(ak_y)), \\ T(\mathbf{k}) =& \frac{T}{a}(i\sin(ak_x) + \sin(ak_y)), \\ R(\mathbf{k}) =& \frac{2R_1}{a^2}\left[\cos(ak_x) - \cos(ak_y) - i\sin(ak_x)\sin(ak_y)\right] \\ &+ \frac{2R_2}{a^2}\left[\cos(ak_x) - \cos(ak_y) + i\sin(ak_x)\sin(ak_y)\right]. \end{aligned} \tag{4.58}$$

We first compute the Hamiltonian on a nanoribbon, so we have to partially Fourier transform it in one direction, say the y direction. We obtain a Hamiltonian which is in k space for the x direction and in real space for the y direction. We repeat the same tricks as in Chaps. 1 and 2. First, we obtain the band structure as shown in Fig. 4.5. We observe the existence of edge states which link the conduction band to the valence band. These edge states are doubly degenerate: each edge has two counterpropagating edge states. The momentum scale of the bandstructure coincides with the values obtained using the full $k \cdot p$ model in Ref. [65]. On a technical note, the gap is relatively small using our model parameters. This is why we need a rather large ribbon for our numerical simulations ($L = 200a = 122$ nm – 200 unit cells).

With the wave functions, we can then extract the spin texture as shown in Fig. 4.6. The spin texture is non-symmetric, especially due to the anisotropic coefficients. Rashba SOC also contributes to it, but to a smaller extent. Nonetheless, the main features remain close to what we saw in Chap. 2. $\mathcal{K}(k_1, k_1) = 0$, because the wave functions are orthogonal by construction, and $\mathcal{K}(k_1, -k_1) = 0$, because the wave functions are orthogonal by Kramers' theorem. Moreover, the shape is still very close to what we observed in the other plots in Chap. 2. We can estimate the value of k_0 by fitting the two-dimensional data. We obtain $k_0 \approx 1.16$ nm^{-1}. This value is very small compared to the other values of k_0 we computed in Tab. 2.1.

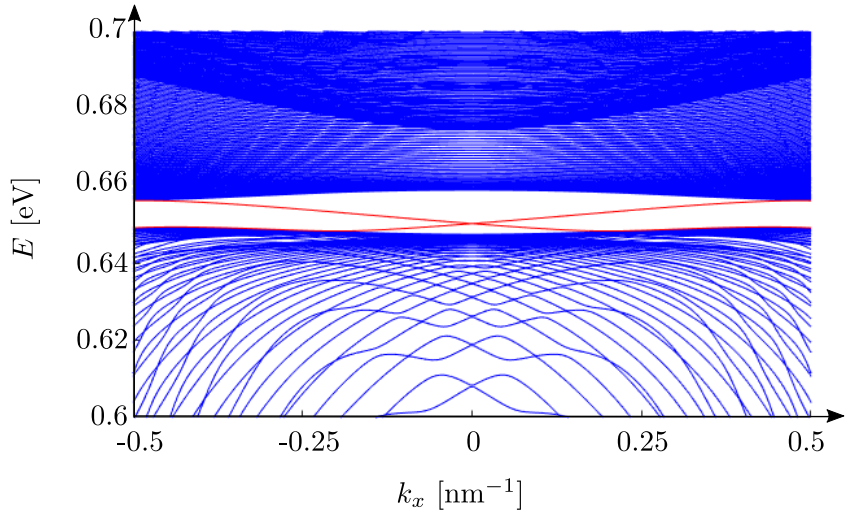

Figure 4.5: The energy spectrum of the effective Hamiltonian in Eq. (4.54) for a nanoribbon of $L = 200a = 122$ nm (200 unit cells). We set $a = 0.61$ nm, the spacing in the periodic direction $k_x = \pi/(400a)$ and the other parameters are defined in Tab. 4.2.

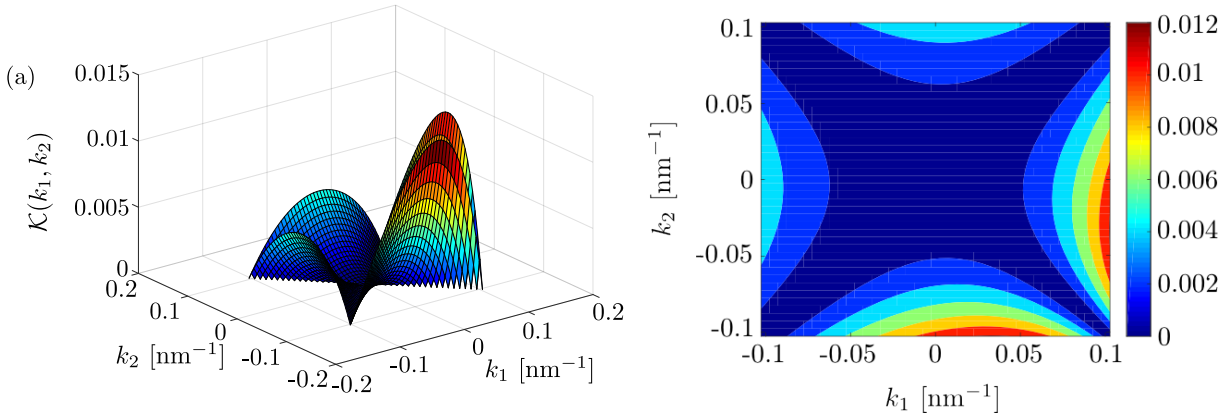

Figure 4.6: The spin texture of the effective Hamiltonian in Eq. (4.54) for a nanoribbon of $L = 122$ nm. We set $a = 0.61$ nm, the spacing in the periodic direction $k_x = \pi/(400a)$ and the other parameters are defined in Tab. 4.2. In panel (a), we have the three-dimensional plot and in panel (b), the corresponding contour plot.

If we now look to the ribbon rotated by $\pi/4$, we can now repeat the same procedure for the $\tilde{k}_{x,y}$ plane. We can regularize the model using $\tilde{k}_{x,y} \approx \sin(a\tilde{k}_{x,y})/a$ and $\tilde{k}^2_{x,y} \approx (2-2\cos(a\tilde{k}_{x,y}))/a^2$. The regularization implies that the effective Bloch matrix transforms as

$$\tilde{H}^{eff}_{\pi/4}(\tilde{\mathbf{k}}) = \begin{pmatrix} \tilde{\varepsilon}(\tilde{\mathbf{k}}) + \tilde{\mathcal{M}}(\tilde{\mathbf{k}}) & A(\tilde{\mathbf{k}}) & T(\tilde{\mathbf{k}}) & R(\tilde{\mathbf{k}}) \\ A^*(\tilde{\mathbf{k}}) & \tilde{\varepsilon}(\tilde{\mathbf{k}}) - \tilde{\mathcal{M}}(\tilde{\mathbf{k}}) & -R(\tilde{\mathbf{k}}) & 0 \\ T^*(\tilde{\mathbf{k}}) & -R^*(\tilde{\mathbf{k}}) & \tilde{\varepsilon}(\tilde{\mathbf{k}}) + \tilde{\mathcal{M}}(\tilde{\mathbf{k}}) & -A^*(\tilde{\mathbf{k}}) \\ R^*(\tilde{\mathbf{k}}) & 0 & -A(\tilde{\mathbf{k}}) & \tilde{\varepsilon}(\tilde{\mathbf{k}}) - \tilde{\mathcal{M}}(\tilde{\mathbf{k}}) \end{pmatrix}, \tag{4.59}$$

where the different terms of the Hamiltonian are

$$\begin{aligned} \tilde{\varepsilon}(\tilde{\mathbf{k}}) =& C - \frac{2D}{a^2}[2 - \cos(a\tilde{k}_x) - \cos(a\tilde{k}_y)], \\ \tilde{\mathcal{M}}(\tilde{\mathbf{k}}) =& M - \frac{2B}{a^2}[2 - \cos(a\tilde{k}_x) - \cos(a\tilde{k}_y)], \\ A(\tilde{\mathbf{k}}) =& e^{-i\pi/4}\frac{A}{a}(\sin(a\tilde{k}_x) + i\sin(a\tilde{k}_y)), \\ T(\tilde{\mathbf{k}}) =& e^{i\pi/4}\frac{T}{a}(i\sin(a\tilde{k}_x) + \sin(a\tilde{k}_y)), \\ R(\tilde{\mathbf{k}}) =& \frac{2R_1}{a^2}\left[\cos(a\tilde{k}_x) - \cos(a\tilde{k}_y) - i\sin(a\tilde{k}_x)\sin(a\tilde{k}_y)\right] \\ &+ \frac{2R_2}{a^2}\left[\cos(a\tilde{k}_y) - \cos(a\tilde{k}_x) - i\sin(ak_x)\sin(ak_y)\right]. \end{aligned} \tag{4.60}$$

We compute the Hamiltonian on a nanoribbon after partially Fourier transforming it. We choose to partially Fourier transform it along the $\tilde{y}$ direction. The band structure is then shown in Fig. 4.7. We observe in comparison to Fig 4.5 a different bandstructure near the gap and also a different energy dispersion for the edge states. This change is due to the anisotropy terms. For a consistency check, we also plot the bandstructure in the absence of anisotropy in both orientations, which give identical results.

Finally, we plot the spin texture in the same manner as before. The result is shown in Fig. 4.8. The main features of the spin texture are again present: vanishing diagonals and a hyperbolic shape. Nevertheless, we observe that the spin texture is different in comparison to what is shown in Fig. 4.6. The anisotropy of the spin texture is weaker and its numerical values are changed. Moreover, we can estimate the value of k_0 by fitting the two-dimensional plot. We obtain $k_0 \approx 0.99\ \mathrm{nm}^{-1}$. This value is close to what we observed above in the other orientation. Nonetheless it seems better to measure the spin texture in this rotated orientation, as k_0 is easier to evaluate due to the smaller anisotropies, and its numerical value is a little smaller. The latter means that the rotation of the spin quantization axis happens on a slightly shorter momentum scale.

In Ref. [78], Ortiz et al. proposed a formula to analytically compute the value of

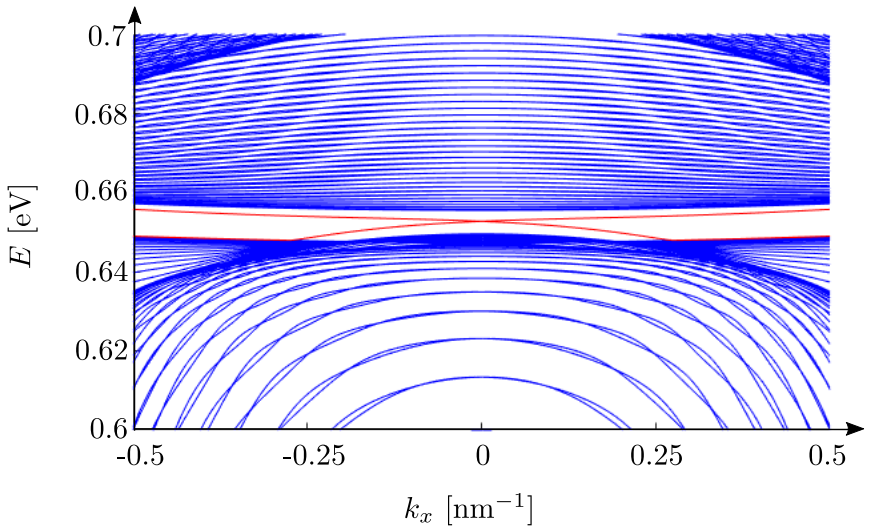

Figure 4.7: The energy spectrum of the effective Hamiltonian in Eq. (4.56) for a nanoribbon of $L = 200a = 122$ nm (200 unit cells). We set $a = 0.61$ nm, the spacing in the periodic direction $k_x = \pi/(400a)$ and the other parameters are defined in Tab. 4.2.

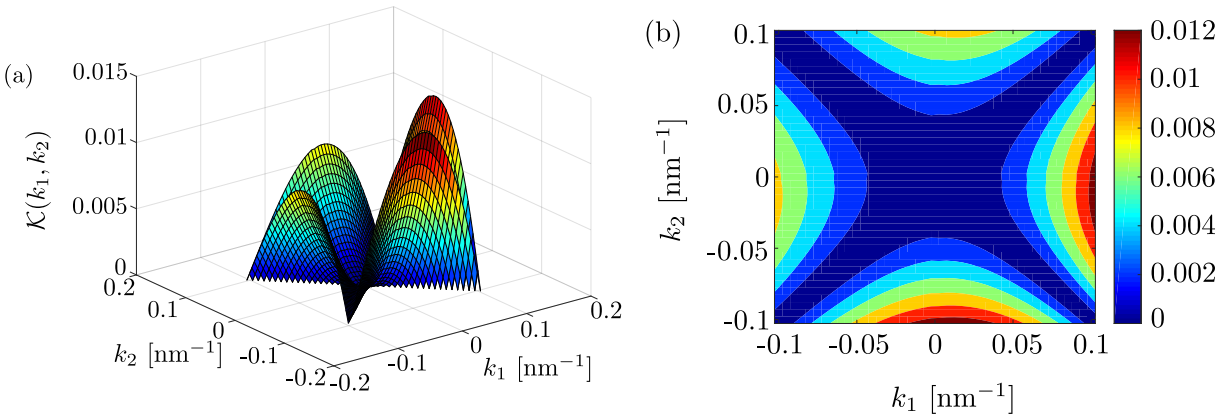

Figure 4.8: The spin texture of the effective Hamiltonian in Eq. (4.56) for a rotated nanoribbon of $L = 122$ nm. We set $a = 0.61$ nm, the spacing in the periodic direction $k_x = \pi/(400a)$ and the other parameters are defined in Tab. 4.2. In panel (a), we have the three-dimensional plot and in panel (b), the corresponding contour plot.

the spin texture in the BHZ Hamiltonian with Rashba SOC, but in the absence of any anisotropic terms. If we use their formula, we obtain that $k_0 \approx 1.15$ nm^{-1}, which is close to the value of k_0 in both orientations. Numerically, we also evaluated k_0 in the absence of anisotropies R_1 and R_2. It gives us a similar value: $k_0 \approx 1.1$ nm^{-1}. It is interesting to note that the value of k_0 is in between the two values obtained for the two crystallographic orientations and very close to their average. Moreover, this value sounds reasonable even though it is relatively small, because we also evaluated k_0 numerically and analytically with the parameters given in Ref. [78]. We obtained in both computations a k_0 of the same order of magnitude, but larger.

To summarize our results, InAs/GaSb heterostructures give a very interesting candidate to experimentally understand and measure the spin texture for two main reasons. Firstly, the bandstructure and the edge state dispersion are influenced by the crystallographic orientation of the nanoribbon. Therefore, we could imagine that this would also lead to interesting features in a full real space system. Secondly, k_0 is surprisingly small, which means that its effect on the spin texture is large. Therefore, a full rotation of the spin axis would then occur in a fraction of the Brillouin zone. The experimental scheme presented in the previous chapters would then provide possible means to probe it. For example, a local spectroscopic probe as presented at the end of Chap. 2 might be able to measure the change of spin texture.

5 | Summary and outlook

In this thesis we explored the nontrivial spin texture arising in two-dimensional insulators. The main ingredient in generating such an outcome was the breaking of the spin quantization axis symmetry. This can be achieved by introducing some structure and/or bulk inversion asymmetry terms in the models. Such phenomena are observed in experimental setups and thus validate the aim of understanding edge states in two-dimensional topological insulators with an undefined spin quantization axis. This scheme was introduced through the concept of generic helical edge states, which require only time-reversal symmetry. The approach we took enabled us to find that the spin axis rotates at low momenta, while preserving time-reversal symmetry. It also enables new processes like inelastic scattering to occur.

We explored several avenues to generalize and understand the implication of the absence of spin quantization axis symmetry. The first section in chapter 2 generalized the concept of spin texture and the observation of the spin quantization axis rotation in the absence of translational symmetry. We realized in the presence of rotational symmetry that the total angular momentum replaced the momentum in the evaluation of the spin texture. Moreover, when we compared the scale at which the spin axis rotates in both translation and rotation invariant systems, they appeared to be equivalent. Nonetheless, the underlying requirement of some kind of spatial symmetry was always present. To push the universality of our findings, we also investigated the spin texture in the absence of some spatial symmetry, e.g. in flakes. It resulted again that the spin axis was rotating when the counterpropagating wave functions were at different energy. This suggested to us that the evaluation of the spin texture could be a rather "local" measure, where only a few sites needed to be included. This led us to propose that the spin texture could be experimentally detected using a spectroscopic probe.

Edge states and the nontrivial topological state of topological insulators are often probed using transport experiments. This led us in chapter 3 to suggest a transport setup made of a Hall bar with an embedded antidot. This Hall bar was connected to four independent leads. We first examined the role of the spin texture in the absence of interaction between the electrons on the antidot. If the spin texture is different between

the Hall bar edges, the transmission rates were dependent on the difference between the two spin textures. However, in the homogeneous case, we discovered that the spin texture implicitly appeared in the nonzero spin-flipping tunnelings and thus modified the transmission rates between the leads. To complete the exploration of the transport setup, we also looked at the Coulomb blockade regime. We started with the help of Fermi's golden rule to compute the sequential tunneling. However as this regime assumes the relaxation to the ground states between two tunneling events, the chirality of the electrons tunneling could not be tracked. This led us to compute the next order tunneling term, namely cotunneling. Here, the current distribution depended upon the initial occupation of the antidot. If there was an even occupation, i.e. the electrons were doubly occupying the energy levels on the antidot up to the Fermi energy, we recovered an implicit dependence on the spin texture. However, if there was an odd occupation, the difference of spin texture between the outer edge and the antidot appeared explicitly. As the process did not conserve energy, this difference could be nonzero.

Finally, the last chapter studied in more detail InAs/GaSb heterostructures, which exhibit large Rashba spin-orbit coupling. From the $k \cdot p$ Hamiltonian, we extracted an effective model in two dimensions for one hole and one electron band, which is very close to the Bernevig-Hughes-Zhang model. We observed that in addition to the Rashba spin-orbit coupling term, there were two other anisotropic terms. These terms influence the Fermi surface, but also the band structure. The latter changed, if they were not measured in the same crystallographic orientation. This also implied some changes in the spin texture. It became orientation-dependent: the values of k_0 as well as the anisotropies in the measure of the rotation of the spin axis were affected by this. Moreover, k_0 was relatively small. This implies that the rotation is occurring rather fast in the band structure. As InAs/GaSb heterostructres are already an active area of experimental investigation, this system would be an interesting playground to probe the spin texture.

In this thesis, we found that spin-orbit coupling plays an important role in topological insulators, which leads to an interesting spin texture. However, there are still some open questions. If we stay focused on the last part of this thesis as InAs/GaSb heterostructures are good candidates to experimentally probe the spin texture, an important point would be to understand better the orientation dependent Fermi surface, which implies also a change in the properties of the edge states. Up to now, the spin texture was considered not to depend on the geometric shape of the edges. We could wonder what could be the effect on a quantum (anti)dot for example. Moreover, as it was shown in this thesis that the spin texture can be measured locally, this could be a first attempt to observe the orientation dependent spin textures. We could also wonder what would be the influence of an orientation dependent spin texture on the transport measurements.

Another important open question is related to the fact that the edge states are usually modeled as one dimensional systems, with an exponentially decaying wave function in the perpendicular direction to the edge. We pointed out in this thesis that the edge states had a spatial distribution in the growth direction of the heterostructure. There was also a spatial separation between the states, with the hole states mainly localized in the GaSb layer, whereas the electron states were mainly in the InAs layer. One could consider the consequences for the full three dimensional wave function, in particular in the case of interactions and impurities located only at the edge. We could wonder how the edge states would then spread into the heterostructure, and in which material they would mainly be localized, inheriting the properties of the layer they are located in.

A | Scattering matrices

This appendix describes the details of how to compute the scattering matrix presented in Eq. (3.13).

A.1 Scattering matrix at resonance

We will start when the system is at resonance, i.e. when the chemical potential μ corresponds to one of the eigenenergies of the antidot. We make the ansatz that the wave functions of the outer edges are represented as plane-waves as in Eq. (3.11), so that we can similarly define the antidot wave functions near each tunneling regions to be

$$\begin{aligned}\Psi_{d\pm 0} &= \frac{e^{-i\mu t}}{\sqrt{2\pi v_F}} \begin{cases} c_1(d_2)e^{\pm i j_F r/R} & r<0 \\ d_1(c_2)e^{\pm i j_F r/R} & r>0 \end{cases}, \\ \Psi_{d\pm \pi R} &= \frac{e^{-i\mu t}}{\sqrt{2\pi v_F}} \begin{cases} c_3(d_4)e^{\pm j_F r/R} & r<\pi R \\ d_3(c_4)e^{\pm j_F r/R} & r>\pi R \end{cases},\end{aligned} \tag{A.1}$$

where we describe the incoming wave functions (with amplitude c_i) and the outgoing wave functions (with amplitude d_i). With such wave functions, we can evaluate the Heisenberg equations of motion $i\partial_t \Psi_{s\alpha} = [\Psi_{s\alpha}, \mathcal{H}]$ and $i\partial_t \Psi_{\mathrm{d}\alpha\beta} = [\Psi_{\mathrm{d}\alpha\beta}, \mathcal{H}]$, where $s = U, L$, $\alpha = \pm$, $\beta = 0, \pi R$, and $\mathcal{H}$ is the full Hamiltonian written in Eq. (3.1). We get for the upper part the following scattering matrix which relates:

$$\begin{pmatrix} b_1 \\ b_2 \\ d_1 \\ d_2 \end{pmatrix} = S_U \begin{pmatrix} a_1 \\ a_2 \\ c_1 \\ c_2 \end{pmatrix}, \tag{A.2}$$

where

$$S_U = \begin{pmatrix} 0 & \frac{1-\Gamma}{1+\Gamma} & \frac{2i\sqrt{\Gamma}\sin(\theta_U)}{1+\Gamma} & -\frac{2i\sqrt{\Gamma}\cos(\theta_U)}{1+\Gamma} \\ \frac{1-\Gamma}{1+\Gamma} & 0 & -\frac{2i\sqrt{\Gamma}\cos(\theta_U)}{1+\Gamma} & -\frac{2i\sqrt{\Gamma}\sin(\theta_U)}{1+\Gamma} \\ -\frac{2i\sqrt{\Gamma}\sin(\theta_U)}{1+\Gamma} & -\frac{2i\sqrt{\Gamma}\cos(\theta_U)}{1+\Gamma} & 0 & \frac{1-\Gamma}{1+\Gamma} \\ -\frac{2i\sqrt{\Gamma}\cos(\theta_U)}{1+\Gamma} & \frac{2i\sqrt{\Gamma}\sin(\theta_U)}{1+\Gamma} & \frac{1-\Gamma}{1+\Gamma} & 0 \end{pmatrix}, \tag{A.3}$$

with $\Gamma = |\gamma_T|^2/(4v_F^2)$ and $\theta_U = \theta_{Uk_F} - \theta_{j_F} + \theta_T$. We can repeat the same procedure for the lower part. The scattering matrix relates

$$\begin{pmatrix} d_3 \\ d_4 \\ b_3 \\ b_4 \end{pmatrix} = S_L \begin{pmatrix} c_3 \\ c_4 \\ a_3 \\ a_4 \end{pmatrix}, \tag{A.4}$$

where

$$S_L = (-1)^{j_F+1} \begin{pmatrix} 0 & (-1)^{j_F+1}\frac{1-\Gamma}{1+\Gamma} & -\frac{2i\sqrt{\Gamma}\sin(\theta_L)}{1+\Gamma} & \frac{2i\sqrt{\Gamma}\cos(\theta_L)}{1+\Gamma} \\ (-1)^{j_F+1}\frac{1-\Gamma}{1+\Gamma} & 0 & \frac{2i\sqrt{\Gamma}\cos(\theta_L)}{1+\Gamma} & \frac{2i\sqrt{\Gamma}\sin(\theta_L)}{1+\Gamma} \\ \frac{2i\sqrt{\Gamma}\sin(\theta_L)}{1+\Gamma} & \frac{2i\sqrt{\Gamma}\cos(\theta_L)}{1+\Gamma} & 0 & (-1)^{j_F+1}\frac{1-\Gamma}{1+\Gamma} \\ \frac{2i\sqrt{\Gamma}\cos(\theta_L)}{1+\Gamma} & -\frac{2i\sqrt{\Gamma}\sin(\theta_L)}{1+\Gamma} & (-1)^{j_F+1}\frac{1-\Gamma}{1+\Gamma} & 0 \end{pmatrix}, \tag{A.5}$$

with $\theta_L = \theta_{j_F} - \theta_{Lk_F} + \theta_T$. If we assume that the structure of each tunneling matrix can be decomposed into four blocks such that

$$S_{U,L} = \begin{pmatrix} r_{U,L} & t'_{U,L} \\ t_{U,L} & r'_{U,L} \end{pmatrix}, \tag{A.6}$$

we are able to write the final scattering matrix, which contains only the amplitudes coming from the leads [105, 140]. The total scattering matrix relates these amplitudes as shown in Eq. (3.12). The effect of the phase, which appears when we want to equalize the two forms of the wave function in Eq. (A.1), is accounted for by the factor $(-1)^{j_F}$ in S_L. The final scattering matrix is then

$$\begin{aligned} S =& \left[\begin{pmatrix} r_1 & 0 \\ 0 & r'_2 \end{pmatrix} + \begin{pmatrix} t'_1 & 0 \\ 0 & t_2 \end{pmatrix} \left(\sigma_x \otimes \sigma_x - \begin{pmatrix} r'_1 & 0 \\ 0 & r_2 \end{pmatrix} \right)^{-1} \begin{pmatrix} t_1 & 0 \\ 0 & t'_2 \end{pmatrix} \right] \\ =& (-1)^{j_F+1} \begin{pmatrix} 0 & 0 & -\sin(\Theta) & \cos(\Theta) \\ 0 & 0 & \cos(\Theta) & \sin(\Theta) \\ \sin(\Theta) & \cos(\Theta) & 0 & 0 \\ \cos(\Theta) & -\sin(\Theta) & 0 & 0 \end{pmatrix}, \end{aligned} \tag{A.7}$$

where $\Theta = \theta_U + \theta_L = \theta_{Uk_F} - \theta_{Lk_F} + 2\theta_T$.

We can double-check our results using the transfer matrix formalism [140]. The transfer matrix connects the tunneling region of the outer edge to the one of the antidot edge. For example, we have

$$\begin{pmatrix} d_1 \\ d_2 \\ c_1 \\ c_2 \end{pmatrix} = M_U \begin{pmatrix} a_1 \\ a_2 \\ b_1 \\ b_2 \end{pmatrix} \tag{A.8}$$

It is connected to the scattering matrix by

$$M_{U,L} = \begin{pmatrix} t_{U,L} - r'_{U,L}(t'_{U,L})^{-1} r_{U,L} & r'_{U,L}(t'_{U,L})^{-1} \\ -(t'_{U,L})^{-1} r_{U,L} & (t'_{U,L})^{-1} \end{pmatrix}. \tag{A.9}$$

The total transfer matrix connects the upper contacts to the lower contacts in the following manner

$$\begin{pmatrix} b_3 \\ b_4 \\ a_3 \\ a_4 \end{pmatrix} = M \begin{pmatrix} a_1 \\ a_2 \\ b_1 \\ b_2 \end{pmatrix}, \tag{A.10}$$

where $M = M_L(\mathbb{1} \otimes \sigma_x)M_U$. By inverting the total transfer matrix to recover the total scattering matrix, we find that the transmission rates were identical.

A.2 Scattering matrix off resonance

We extend our description to when the tunneling is occurring off resonance. We will follow the method described in Chap. 8 of Ref. [141]. We consider the phase acquired by the electron along one half of the antidot to be $\phi = \frac{\pi R \mu}{v_F}$. We are then able to rewrite the equivalence between the incoming and the outcoming states if the electrons originate from the contact 1.

$$\begin{pmatrix} b_1 \\ b_2 \\ d_1 \\ d_2 \\ d_3 \\ d_4 \\ b_3 \\ b_4 \end{pmatrix} = \tilde{S} \begin{pmatrix} a_1 \\ 0 \\ d_4 e^{i\phi} \\ d_3 e^{i\phi} \\ d_2 e^{i\phi} \\ d_1 e^{i\phi} \\ 0 \\ 0 \end{pmatrix}, \tag{A.11}$$

where we use the definition that

$$\tilde{S} = \begin{pmatrix} r_U & t'_U & 0 & 0 \\ t_U & r'_U & 0 & 0 \\ 0 & 0 & r_U & t'_U \\ 0 & 0 & t_U & r'_U \end{pmatrix}. \tag{A.12}$$

We solve the coupled equations in Eq. (A.11) to obtain the first line of Eq. (3.13). We repeat the same process for the other contacts to describe the full scattering matrix. We can also use transfer matrix formalism, such that the total transfer matrix is

$$\tilde{M} = M_U(\mathbb{1} \otimes \sigma_x)e^{i\phi\sigma_z \otimes \mathbb{1}} M_U, \tag{A.13}$$

which enables us to double-check our results. Another double-check is done at the resonance limit ($\phi = \pi j_F$).

Bibliography

[1] F. D. M. Haldane, Journal of Physics C: Solid State Physics **14**, 2585 (1981).

[2] C. Kim, A. Y. Matsuura, Z.-X. Shen, N. Motoyama, H. Eisaki, S. Uchida, T. Tohyama, and S. Maekawa, Phys. Rev. Lett. **77**, 4054 (1996).

[3] B. Kim, H. Koh, E. Rotenberg, S.-J. Oh, H. Eisaki, N. Motoyama, S. Uchida, T. Tohyama, S. Maekawa, Z.-X. Shen, et al., Nature Physics **2**, 397 (2006).

[4] Y. Jompol, C. J. B. Ford, J. P. Griffiths, I. Farrer, G. A. C. Jones, D. Anderson, D. A. Ritchie, T. W. Silk, and A. J. Schofield, Science **325**, 597 (2009).

[5] K. S. Novoselov, A. K. Geim, S. V. Morozov, D. Jiang, Y. Zhang, S. V. Dubonos, I. V. Grigorieva, and A. A. Firsov, Science **306**, 666 (2004).

[6] C. L. Kane and E. J. Mele, Phys. Rev. Lett. **95**, 146802 (2005).

[7] C. L. Kane and E. J. Mele, Phys. Rev. Lett. **95**, 226801 (2005).

[8] B. A. Bernevig, T. L. Hughes, and S.-C. Zhang, Science **314**, 1757 (2006).

[9] L. Fu, C. L. Kane, and E. J. Mele, Phys. Rev. Lett. **98**, 106803 (2007).

[10] J. E. Moore and L. Balents, Phys. Rev. B **75**, 121306 (2007).

[11] R. Roy, Phys. Rev. B **79**, 195322 (2009).

[12] M. König, S. Wiedmann, C. Brüne, A. Roth, H. Buhmann, L. W. Molenkamp, X.-L. Qi, and S.-C. Zhang, Science **318**, 766 (2007).

[13] I. Knez, R.-R. Du, and G. Sullivan, Phys. Rev. Lett. **107**, 136603 (2011).

[14] C. Wu, B. A. Bernevig, and S.-C. Zhang, Phys. Rev. Lett. **96**, 106401 (2006).

[15] C. Liu, T. L. Hughes, X.-L. Qi, K. Wang, and S.-C. Zhang, Phys. Rev. Lett. **100**, 236601 (2008).

[16] D. G. Rothe, R. W. Reinthaler, C.-X. Liu, L. W. Molenkamp, S.-C. Zhang, and E. M. Hankiewicz, New Journal of Physics **12**, 065012 (2010).

[17] T. L. Schmidt, S. Rachel, F. von Oppen, and L. I. Glazman, Phys. Rev. Lett. **108**, 156402 (2012).

[18] M. Z. Hasan and C. L. Kane, Rev. Mod. Phys. **82**, 3045 (2010).

[19] X.-L. Qi and S.-C. Zhang, Rev. Mod. Phys. **83**, 1057 (2011).

[20] Y. Ando, Journal of the Physical Society of Japan **82**, 102001 (2013).

[21] M. Fruchart and D. Carpentier, Comptes Rendus Physique **14**, 779 (2013).

[22] G. Dolcetto, M. Sassetti, and T. L. Schmidt, Riv. Nuovo Cimento **39**, 113 (2016).

[23] A. Bansil, H. Lin, and T. Das, Rev. Mod. Phys. **88**, 021004 (2016).

[24] B. Bernevig and T. Hughes, *Topological Insulators and Topological Superconductors* (Princeton University Press, 2013).

[25] S. Shen, *Topological Insulators: Dirac Equation in Condensed Matters*, Springer Series in Solid-State Sciences (Springer Berlin Heidelberg, 2013).

[26] M. Franz and L. Molenkamp, eds., *Topological Insulators*, vol. 6 of *Contemporary Concepts of Condensed Matter Science* (Elsevier Science, 2013).

[27] L. D. Landau, Zh. Eksp. Teor. Fiz. **11**, 19 (1937).

[28] K. von Klitzing, G. Dorda, and M. Pepper, Phys. Rev. Lett. **45**, 494 (1980).

[29] B. I. Halperin, Phys. Rev. B **25**, 2185 (1982).

[30] R. B. Laughlin, Phys. Rev. B **23**, 5632 (1981).

[31] D. J. Thouless, M. Kohmoto, M. P. Nightingale, and M. den Nijs, Phys. Rev. Lett. **49**, 405 (1982).

[32] M. V. Berry, Proceedings of the Royal Society of London A: Mathematical, Physical and Engineering Sciences **392**, 45 (1984).

[33] J. Zak, Phys. Rev. Lett. **62**, 2747 (1989).

[34] B. Simon, Phys. Rev. Lett. **51**, 2167 (1983).

[35] M. Kohmoto, Annals of Physics **160**, 343 (1985).

[36] J. E. Avron, R. Seiler, and B. Simon, Physical Review Letters **51**, 51 (1983).

[37] R. Jackiw and C. Rebbi, Phys. Rev. D **13**, 3398 (1976).

[38] F. D. M. Haldane, Phys. Rev. Lett. **61**, 2015 (1988).

[39] G. W. Semenoff, Phys. Rev. Lett. **53**, 2449 (1984).

[40] H. A. Kramers, Proceedings Koninklijke Akademie van Wetenschappen **33**, 959 (1930).

[41] B. Bransden and C. Joachain, *Physics of Atoms and Molecules*, Pearson Education (Prentice Hall, 2003).

[42] J. J. Sakurai and J. J. Napolitano, *Modern Quantum Mechanics* (Addison Wesley, 2011), 2nd ed.

[43] D. Bercioux and P. Lucignano, Reports on Progress in Physics **78**, 106001 (2015).

[44] X.-L. Qi and S.-C. Zhang, Physics Today **63**, 33 (2010).

[45] A. Manchon, H. Koo, J. Nitta, S. Frolov, and R. Duine, Nature materials **14**, 871 (2015).

[46] E. I. Rashba, Sov. Phys. Solid State **2**, 1109 (1960).

[47] Y. A. Bychkov and E. I. Rashba, Soviet Journal of Experimental and Theoretical Physics Letters **39**, 66 (1984).

[48] G. Dresselhaus, Phys. Rev. **100**, 580 (1955).

[49] R. Winkler, *Spin-orbit Coupling Effects in Two-Dimensional Electron and Hole Systems*, Springer Tracts in Modern Physics (Springer Berlin Heidelberg, 2003).

[50] D. N. Sheng, Z. Y. Weng, L. Sheng, and F. D. M. Haldane, Phys. Rev. Lett. **97**, 036808 (2006).

[51] D. Huertas-Hernando, F. Guinea, and A. Brataas, Phys. Rev. B **74**, 155426 (2006).

[52] H. Min, J. E. Hill, N. A. Sinitsyn, B. R. Sahu, L. Kleinman, and A. H. MacDonald, Phys. Rev. B **74**, 165310 (2006).

[53] C.-C. Liu, W. Feng, and Y. Yao, Phys. Rev. Lett. **107**, 076802 (2011).

[54] C.-C. Liu, H. Jiang, and Y. Yao, Phys. Rev. B **84**, 195430 (2011).

[55] M. Ezawa, Phys. Rev. Lett. **109**, 055502 (2012).

[56] L. Voon and M. Willatzen, *The k.p Method: Electronic Properties of Semiconductors* (Springer Berlin Heidelberg, 2009).

[57] M. König, H. Buhmann, L. W. Molenkamp, T. Hughes, C.-X. Liu, X.-L. Qi, and S.-C. Zhang, Journal of the Physical Society of Japan **77**, 031007 (2008).

[58] A. Roth, C. Brüne, H. Buhmann, L. W. Molenkamp, J. Maciejko, X.-L. Qi, and S.-C. Zhang, Science **325**, 294 (2009).

[59] C. Brüne, A. Roth, E. G. Novik, M. König, H. Buhmann, E. M. Hankiewicz, W. Hanke, J. Sinova, and L. W. Molenkamp, Nature Physics **6**, 448 (2010).

[60] G. M. Gusev, Z. D. Kvon, E. B. Olshanetsky, A. D. Levin, Y. Krupko, J. C. Portal, N. N. Mikhailov, and S. A. Dvoretsky, Phys. Rev. B **89**, 125305 (2014).

[61] K. C. Nowack, E. M. Spanton, M. Baenninger, M. König, J. R. Kirtley, B. Kalisky, C. Ames, P. Leubner, C. Brüne, H. Buhmann, et al., Nature Materials **12**, 787 (2013).

[62] S. Hart, H. Ren, T. Wagner, P. Leubner, M. Mühlbauer, C. Brüne, H. Buhmann, L. W. Molenkamp, and A. Yacoby, Nature Physics **10**, 638 (2014).

[63] M. König, M. Baenninger, A. G. F. Garcia, N. Harjee, B. L. Pruitt, C. Ames, P. Leubner, C. Brüne, H. Buhmann, L. W. Molenkamp, et al., Phys. Rev. X **3**, 021003 (2013).

[64] C. Liu and S.-C. Zhang, in *Topological Insulators*, edited by M. Franz and L. Molenkamp (Elsevier Science, 2013), vol. 6 of *Contemporary Concepts of Condensed Matter Science*.

[65] F. Nichele, M. Kjaergaard, H. J. Suominen, R. Skolasinski, M. Wimmer, B.-M. Nguyen, A. A. Kiselev, W. Yi, M. Sokolich, M. J. Manfra, et al., Phys. Rev. Lett. **118**, 016801 (2017).

[66] K. Suzuki, Y. Harada, K. Onomitsu, and K. Muraki, Phys. Rev. B **87**, 235311 (2013).

[67] I. Knez, C. T. Rettner, S.-H. Yang, S. S. P. Parkin, L. Du, R.-R. Du, and G. Sullivan, Phys. Rev. Lett. **112**, 026602 (2014).

[68] L. Du, I. Knez, G. Sullivan, and R.-R. Du, Phys. Rev. Lett. **114**, 096802 (2015).

[69] F. Qu, A. J. A. Beukman, S. Nadj-Perge, M. Wimmer, B.-M. Nguyen, W. Yi, J. Thorp, M. Sokolich, A. A. Kiselev, M. J. Manfra, et al., Phys. Rev. Lett. **115**, 036803 (2015).

[70] T. Li, P. Wang, H. Fu, L. Du, K. A. Schreiber, X. Mu, X. Liu, G. Sullivan, G. A. Csáthy, X. Lin, et al., Phys. Rev. Lett. **115**, 136804 (2015).

[71] K. Suzuki, Y. Harada, K. Onomitsu, and K. Muraki, Phys. Rev. B **91**, 245309 (2015).

[72] S. Mueller, A. N. Pal, M. Karalic, T. Tschirky, C. Charpentier, W. Wegscheider, K. Ensslin, and T. Ihn, Phys. Rev. B **92**, 081303 (2015).

[73] F. Couëdo, H. Irie, K. Suzuki, K. Onomitsu, and K. Muraki, Phys. Rev. B **94**, 035301 (2016).

[74] E. M. Spanton, K. C. Nowack, L. Du, G. Sullivan, R.-R. Du, and K. A. Moler, Phys. Rev. Lett. **113**, 026804 (2014).

[75] B.-M. Nguyen, A. A. Kiselev, R. Noah, W. Yi, F. Qu, A. J. A. Beukman, F. K. de Vries, J. van Veen, S. Nadj-Perge, L. P. Kouwenhoven, et al., Phys. Rev. Lett. **117**, 077701 (2016).

[76] F. Nichele, H. J. Suominen, M. Kjaergaard, C. M. Marcus, E. Sajadi, J. A. Folk, F. Qu, A. J. A. Beukman, F. K. de Vries, J. van Veen, et al., New Journal of Physics **18**, 083005 (2016).

[77] A. Rod, T. L. Schmidt, and S. Rachel, Phys. Rev. B **91**, 245112 (2015).

[78] L. Ortiz, R. A. Molina, G. Platero, and A. M. Lunde, Phys. Rev. B **93**, 205431 (2016).

[79] N. Kainaris, I. V. Gornyi, S. T. Carr, and A. D. Mirlin, Phys. Rev. B **90**, 075118 (2014).

[80] A. Rod, G. Dolcetto, S. Rachel, and T. L. Schmidt, Phys. Rev. B **94**, 035428 (2016).

[81] C. P. Orth, G. Strübi, and T. L. Schmidt, Phys. Rev. B **88**, 165315 (2013).

[82] P. Michetti, P. H. Penteado, J. C. Egues, and P. Recher, Semicond. Sci. Technol. **27**, 124007 (2012).

[83] P. Michetti and P. Recher, Phys. Rev. B **83**, 125420 (2011).

[84] W.-Y. Shan, J. Lu, H.-Z. Lu, and S.-Q. Shen, Phys. Rev. B **84**, 035307 (2011).

[85] P. Rakyta, M. Vigh, A. Csordás, and J. Cserti, Phys. Rev. B **91**, 125412 (2015).

[86] A. Kundu, A. Zazunov, A. L. Yeyati, T. Martin, and R. Egger, Phys. Rev. B **83**, 125429 (2011).

[87] M. Abramowitz and I. A. Stegun, *Handbook of mathematical functions: with formulas, graphs, and mathematical tables* (Courier Corporation, 1964).

[88] B. Zhou, H.-Z. Lu, R.-L. Chu, S.-Q. Shen, and Q. Niu, Phys. Rev. Lett. **101**, 246807 (2008).

[89] J. W. Wilder, L. C. Venema, A. G. Rinzler, R. E. Smalley, and C. Dekker, Nature **391**, 59 (1998).

[90] V. J. Goldman and B. Su, Science **267**, 1010 (1995).

[91] M. R. Geller and D. Loss, Phys. Rev. B **56**, 9692 (1997).

[92] V. N. Golovach and D. Loss, Phys. Rev. B **69**, 245327 (2004).

[93] Y. Komijani, P. Simon, and I. Affleck, Phys. Rev. B **92**, 075301 (2015).

[94] G. Dolcetto, F. Cavaliere, D. Ferraro, and M. Sassetti, Phys. Rev. B **87**, 085425 (2013).

[95] S.-Y. Hwang, R. López, M. Lee, and D. Sánchez, Phys. Rev. B **90**, 115301 (2014).

[96] R. López, S.-Y. Hwang, and D. Sánchez, J. Phys. Conf. Ser. **568**, 052016 (2014).

[97] G. Dolcetto and T. L. Schmidt, Phys. Rev. B **94**, 075444 (2016).

[98] T. Posske, C.-X. Liu, J. C. Budich, and B. Trauzettel, Phys. Rev. Lett. **110**, 016602 (2013).

[99] T. Posske and B. Trauzettel, Phys. Rev. B **89**, 075108 (2014).

[100] B. Rizzo, A. Camjayi, and L. Arrachea, Phys. Rev. B **94**, 125425 (2016).

[101] R.-L. Chu, J. Lu, and S.-Q. Shen, EPL (Europhysics Letters) **100**, 17013 (2012).

[102] V. Krueckl and K. Richter, Phys. Rev. Lett. **107**, 086803 (2011).

[103] F. Dolcini, Phys. Rev. B **83**, 165304 (2011).

[104] F. Dolcini, Phys. Rev. B **92**, 155421 (2015).

[105] S. Datta, *Electronic transport in mesoscopic systems* (Cambridge University Press, 1997).

[106] R. Landauer, IBM Journal of Research and Development **1**, 223 (1957).

[107] R. Landauer, Philosophical Magazine **21**, 863 (1970).

[108] M. Büttiker, Y. Imry, R. Landauer, and S. Pinhas, Phys. Rev. B **31**, 6207 (1985).

[109] M. Büttiker, Phys. Rev. B **32**, 1846 (1985).

[110] M. Büttiker, Phys. Rev. Lett. **57**, 1761 (1986).

[111] M. Büttiker, IBM Journal of Research and Development **32**, 63 (1988).

[112] C. W. Groth, M. Wimmer, A. R. Akhmerov, and X. Waintal, New Journal of Physics **16**, 063065 (2014).

[113] L. Fu and C. L. Kane, Phys. Rev. B **76**, 045302 (2007).

[114] P. Sternativo and F. Dolcini, Phys. Rev. B **89**, 035415 (2014).

[115] R.-L. Chu, J. Li, J. K. Jain, and S.-Q. Shen, Phys. Rev. B **80**, 081102 (2009).

[116] H. Bruus and K. Flensberg, *Many-body quantum theory in condensed matter physics* (Oxford University Press Oxford, 2002).

[117] C. W. J. Beenakker, Phys. Rev. B **44**, 1646 (1991).

[118] J. Lehmann and D. Loss, Phys. Rev. B **73**, 045328 (2006).

[119] P.-O. Löwdin, The Journal of Chemical Physics **19**, 1396 (1951).

[120] J. M. Luttinger and W. Kohn, Phys. Rev. **97**, 869 (1955).

[121] E. Kane, Journal of Physics and Chemistry of Solids **1**, 82 (1956).

[122] P. Yu and M. Cardona, *Fundamentals of Semiconductors: Physics and Materials Properties*, no. vol. 3 in Advanced texts in physics (Springer Berlin Heidelberg, 2010), 4th ed.

[123] E. O. Kane, Journal of Physics and Chemistry of Solids **1**, 249 (1957).

[124] J. M. Luttinger, Phys. Rev. **102**, 1030 (1956).

[125] C. R. Pidgeon and R. N. Brown, Phys. Rev. **146**, 575 (1966).

[126] C. R. Pidgeon and S. H. Groves, Phys. Rev. **186**, 824 (1969).

[127] M. H. Weiler, R. L. Aggarwal, and B. Lax, Phys. Rev. B **17**, 3269 (1978).

[128] M. G. Burt, Journal of Physics: Condensed Matter **4**, 6651 (1992).

[129] M. G. Burt, Journal of Physics: Condensed Matter **11**, 53 (1999).

[130] B. A. Foreman, Phys. Rev. B **48**, 4964 (1993).

[131] B. A. Foreman, Phys. Rev. B **56**, R12748 (1997).

[132] E. G. Novik, A. Pfeuffer-Jeschke, T. Jungwirth, V. Latussek, C. R. Becker, G. Landwehr, H. Buhmann, and L. W. Molenkamp, Phys. Rev. B **72**, 035321 (2005).

[133] A. T. Meney, B. Gonul, and E. P. O'Reilly, Phys. Rev. B **50**, 10893 (1994).

[134] E. Halvorsen, Y. Galperin, and K. A. Chao, Phys. Rev. B **61**, 16743 (2000).

[135] P. Lawaetz, Phys. Rev. B **4**, 3460 (1971).

[136] A. Zakharova, S. T. Yen, and K. A. Chao, Phys. Rev. B **66**, 085312 (2002).

[137] L.-H. Hu, C.-X. Liu, D.-H. Xu, F.-C. Zhang, and Y. Zhou, Phys. Rev. B **94**, 045317 (2016).

[138] J. Li, W. Yang, and K. Chang, Phys. Rev. B **80**, 035303 (2009).

[139] Q.-Z. Wang, X. Liu, H.-J. Zhang, N. Samarth, S.-C. Zhang, and C.-X. Liu, Phys. Rev. Lett. **113**, 147201 (2014).

[140] P. A. Mello and N. Kumar, *Quantum Transport in Mesoscopic Systems: Complexity and Statistical Fluctuations, a Maximum-entropy Viewpoint*, no. 4 in Mesoscopic physics and nanotechnology (Oxford University Press, 2004).

[141] T. Heinzel, *Mesoscopic Electronics in Solid State Nanostructures* (Wiley-VCH Verlag GmbH, 2008).

Acknowledgment

It is now the time for me to thank all the persons implied in the completion of this thesis. First, I would like to thank my two supervisors, Stephan Rachel and Thomas Schmidt. I am grateful that they chose me back in early summer 2013 to be their Ph.D. student. I really appreciated to be supervised by both of them as they always supported me, and believed in my abilities. As I am now looking at the past three and a half years, I can see how much I do not regret my choice to start this thesis and discover (a part of) Europe, in Dresden and in Luxembourg. I grew a lot during my Ph.D. both scientifically and personally, and a big part of it is thanks to both of them. I am also grateful to Matthias Vojta for agreeing to be my official supervisor in Dresden and for including me as a member of his group. Before early summer 2013, Thierry Giamarchi supervised me for my master thesis and without his support and his guidance, I guess that I would not have started a Ph.D. I would like to thank as well Giacomo Dolcetto for collaborating with me during my Luxembourgish time.

As this thesis was done in two different places and teams, I would to acknowledge the people that crossed my scientific path. If I start chronologically, I would like to thank the members of Matthias Vojta's and Carsten Timm's groups for the scientific discussions, but also for the activities outside work. In particular, I would like to thank Alex Kashuba, Alex Lau, Chris Koschenz, Darshan Joshi, Eugen Wolf, Fabian Zschocke, Jacob Schmiedt, Johannes Mierau, my office mate Mark Steudtner, Maxim Breitkreiz, Paolo Michetti, Tim Ludwig and Tobias Meng. I hope that I did not forget anyone from the 3pm coffee break. I am grateful for meeting people beyond these two groups and in particular my nice fellows in the local Orga-team for the 2014 DPT.

In Luxembourg, I would like to thank the members of Thomas Schmidt's and Ludger Wirtz's groups for the same reasons as above. In particular, I would like to thank Alejandro Molina, Alessio Calzona, my office mate Chris Pedder, Efterpi Kalesaki, Engin Torun, Fulvio Paleari, my office mate Giacomo Dolcetto, Henrique Miranda, my office mates Patrick Haughian and Solofo Groenendjick, Sven Reichardt, Thomas Galvani and Viktoriia Kornich. I hope again that I did not forget anyone from the 4pm coffee break. Moreover, this thesis would not have been the same without the thorough proofreading of

Chris Pedder! I am also grateful for meeting everyone from the floor below and to those who made my Friday evenings so special at Rock Solid.

As this thesis was done in "cotutelle", I am grateful to all the persons from both university administrations that made everything work so far. I am as well very thankful for the administrative help from Mesdames Latus, Schoffer and Bertrand.

When I left Geneva for Dresden, I left my encouraging friends and family and it implied quite a change in my life. Now I can say that it was great to live in Dresden and in Luxembourg. I improved a lot my German skills, I learned a lot and I met great people in both places. When I left Dresden for Luxembourg, I experienced a bit of nostalgia regarding Dresden and I guess, I will feel the same when my time in Luxembourg will be over.

Last but not least, I would like to thank my family and in particular my parents Cathia and Michel, my sister Jessica and my boyfriend François for their constant support, their endless love and much more!

Eklärung – Statement

Hiermit versichere ich, dass ich die vorliegende Arbeit ohne unzulässige Hilfe Dritter und ohne Benutzung anderer als der angegebenen Hilfsmittel angefertigt habe; die aus fremden Quellen direkt oder indirekt übernommenen Gedanken sind als solche kenntlich gemacht. Die Arbeit wurde bisher weder im Inland noch im Ausland in gleicher oder ähnlicher Form einer anderen Prüfungsbehörde vorgelegt.

Diese Dissertation wurde am Institut für Theoretische Physik der Technischen Universität Dresden unter der Betreuung von Dr. Stephan Rachel und Prof. Dr. Matthias Vojta und an der Forschungseinheit für Physik und Materialwissenschaft der Universität Luxemburg unter der Betreuung von Prof. Dr. Thomas Schmidt angefertigt. Ich erkenne die Promotionsordnung der Fakultät Mathematik und Naturwissenschaften der Technischen Universität Dresden vom 23.02.2011 an.

I herewith declare that I have produced this paper without the prohibited assistance of third parties and without making use of aids other than those specified; notions taken over directly or indirectly from other sources have been identified as such. This paper has not previously been presented in identical or similar form to any other German or foreign examination board.

This dissertation was produced at the Institute for Theoretical Physics, Technische Universität Dresden under the supervision of Dr. Stephan Rachel and Prof. Dr. Matthias Vojta and at the Physics and Materials Science Research Unit, University of Luxembourg under the supervision of Prof. Dr. Thomas Schmidt. I recognize the Doctorate Regulations of the Faculty of Science dated on 23$^{\text{rd}}$ of February 2011.

Alexia Rod
Luxembourg, 09.01.2017